NASA/CR–20240008985

Sonic Boom Analyses in Support of Improved X-59 Community Noise Testing

Kent L. Gee, Mark C. Anderson, Kaylee Nyborg, J. Taggart Durrant,
Jesse D. Blaine and Avery K. Sorrell
Brigham Young University, Provo, Utah

Prepared for:
National Aeronautics and Space Administration
Langley Research Center, Hampton, VA

Contract 80LARC17C004, Activity 202008
Alexandra Loubeau, Technical Monitor

November 2024

NASA STI Program Report Series

Since its founding, NASA has been dedicated to the advancement of aeronautics and space science. The NASA scientific and technical information (STI) program plays a key part in helping NASA maintain this important role.

The NASA STI program operates under the auspices of the Agency Chief Information Officer. It collects, organizes, provides for archiving, and disseminates NASA's STI. The NASA STI program provides access to the NTRS Registered and its public interface, the NASA Technical Reports Server, thus providing one of the largest collections of aeronautical and space science STI in the world. Results are published in both non-NASA channels and by NASA in the NASA STI Report Series, which includes the following report types:

- TECHNICAL PUBLICATION. Reports of completed research or a major significant phase of research that present the results of NASA Programs and include extensive data or theoretical analysis. Includes compilations of significant scientific and technical data and information deemed to be of continuing reference value. NASA counterpart of peer-reviewed formal professional papers but has less stringent limitations on manuscript length and extent of graphic presentations.

- TECHNICAL MEMORANDUM. Scientific and technical findings that are preliminary or of specialized interest, e.g., quick release reports, working papers, and bibliographies that contain minimal annotation. Does not contain extensive analysis.

- CONTRACTOR REPORT. Scientific and technical findings by NASA-sponsored contractors and grantees.

- CONFERENCE PUBLICATION. Collected papers from scientific and technical conferences, symposia, seminars, or other meetings sponsored or co-sponsored by NASA.

- SPECIAL PUBLICATION. Scientific, technical, or historical information from NASA programs, projects, and missions, often concerned with subjects having substantial public interest.

- TECHNICAL TRANSLATION. English-language translations of foreign scientific and technical material pertinent to NASA's mission.

Specialized services also include organizing and publishing research results, distributing specialized research announcements and feeds, providing information desk and personal search support, and enabling data exchange services.

For more information about the NASA STI program, see the following:

- Access the NASA STI program home page at http://www.sti.nasa.gov

- Help desk contact information:

https://www.sti.nasa.gov/sti-contact-form/ and select the "General" help request type.

NASA/CR–20240008985

Sonic Boom Analyses in Support of Improved X-59 Community Noise Testing

Kent L. Gee, Mark C. Anderson, Kaylee Nyborg, J. Taggart Durrant,
Jesse D. Blaine and Avery K. Sorrell
Brigham Young University, Provo, Utah

National Aeronautics and
Space Administration

Langley Research Center
Hampton, Virginia 23681-2199

November 2024

Available from:

NASA STI Program / Mail Stop 148
NASA Langley Research Center
Hampton, VA 23681-2199
Fax: 757-864-6500

This page intentionally left blank.

Table of contents

Table of Figures

Table of tables

Nomenclature and acronyms

ARC	Angular Recording Configuration
ASEL	A-weighted sound exposure level
BSEL	B-weighted sound exposure level
CarpetDIEM	Carpet Determination in Entirety Measurements
CFSv2	Climate Forecast System Version 2
CSEL	C-weighted sound exposure level
DAQ	Data Acquisition
DSEL	D-weighted sound exposure level
ESEL	E-weighted sound exposure level
FFT	Fast Fourier Transform
GRS	Ground recording system
ISBAP	Indoor Sonic Boom Annoyance Predictor
JASA	Journal of the Acoustical Society of America
Lasso	Least absolute shrinkage and selection operator
LR	Lasso Regression
OTO	One-third octave
PL	Perceived Level, calculated according to Shepherd and Sullivan (1991)
QSF18	Quiet Supersonic Flights 2018
RMSE	Root mean-square error
ROM	Reduced-order model
SCAMP	Superboom Caustic Analysis and Measurement Program
SNR	Signal-to-noise ratio
WSPR	Waveforms and Sonic Boom Perception and Response
XVal	Cross-validation
ZSEL	Z-weighted sound exposure level
ΔPM	PCBoom-predicted PL minus measured PL

Executive Summary

This contractor report describes sonic boom and other related analyses performed in support of informing measurement planning and analysis of quiet supersonic aircraft community testing. The report is divided into three main sections: (1) investigations on the impacts of contaminating noise on sonic boom community noise metrics; (2) investigations into sonic boom variability, including turbulence effects on metrics of interest and development of a data-driven boom variability analysis framework; (3) other studies that support developing improved methodologies for community testing and analysis.

The first set of studies involves determining and mitigating the impact of contaminating noise on sonic boom metric calculations. Because it was previously found that high-frequency ambient and instrumentation noise at sonic boom measurement campaigns had impacted calculated metrics – resulting in a positive bias for quieter booms or recordings with greater background noise – an investigation into spectral bandwidth limitations has been conducted. Using simulated X-59 shaped booms with additive noise from the community-based Quiet Supersonic Flights 2018 (QSF18) measurement campaign, different filtering approaches have been investigated. Straightforward time and frequency-domain approaches have been developed that successfully remove the noise contamination from metric calculations. The approach has then been used to determine the required effective bandwidth needed to successfully calculate a given metric, such as B-weighted sound exposure level (BSEL) or Perceived Level (PL), within 1 dB. For a simulated X-59 shaped boom, the required bandwidth is only a few hundred hertz for most of the metrics investigated.

The above filtering method for contaminating noise removal has been used in two other related investigations. First, the impact of contaminating noise on the QSF18 dose-response curves has been studied. Although prior work to obtain human subject doses and connect them to the closest QSF18 measurements was a complex process, this investigation suggests that for quieter booms (those with the greatest potential for contamination), a given percentage of people highly annoyed could have been caused by PLs that were at least 5 dB less than those originally reported. In the second contaminating noise-related study, recorded ambient/electronic noise from a different measurement campaign – the Carpet Determination in Entirety Measurements (CarpetDIEM) flight series – was added to X-59 simulations. This was done to simulate the kind of noise contamination expected for upcoming Quesst Mission Phase 2 X-59 testing. Analysis shows the expected contaminating noise for Phase 2 X-59 measurements is far less than at QSF18, but also that residual noise contamination can be effectively removed using the aforementioned methodology.

The second set of studies in this report deals with quantifying boom variability due to different effects. One of these effects is atmospheric turbulence. A seven-microphone array that spanned 122 m (400 ft) nominally undertrack and perpendicular to the flight path for the 2019 CarpetDIEM I campaign has been used to study boom variability due to turbulence. Analysis of the booms suggests Gaussian distributions about the mean level for each boom can be assumed. However, the 90% confidence interval for the mean varies several decibels across booms and metrics. PL, ASEL, and ESEL were the most affected by turbulence, whereas BSEL, DSEL, and the indoor sonic boom annoyance predictor (ISBAP) were the least affected.

Another variability-related analysis has examined more broadly the potential causes of sonic boom variability for different aircraft and ambient conditions. A Least absolute shrinkage and selection operator (Lasso) Regression-based methodology was developed to examine variability in QSF18 and CarpetDIEM measurements. Lasso Regression (LR) is a useful, straightforward

framework for analyzing sonic boom test flight data to gain important insights and could be adopted during X-59 test flights to guide NASA and partners in understanding the measured and predicted community noise metrics. In the analysis here, LR identifies key factors driving measured metric variability. For example, metrics are sensitive to aircraft trajectory at both CarpetDIEM and QSF18. This is unsurprising for QSF18, which used the low-boom dive maneuver, but it was unexpected for CarpetDIEM, where the measurement plan understood by the field team called for steady-flight cruise booms. After LR identified aircraft trajectory inputs as contributors to measured metric variability, a deeper trajectory analysis showed that some booms at CarpetDIEM were not truly cruise booms. Additionally, LR confirms that contaminating noise is an important factor in measured metric variability, especially at QSF18, and that after filtering the noise the contaminating noise is no longer correlated with the boom metrics.

The LR results also help establish an expected fidelity of predicted levels for X-59 flight tests using data-driven and numerical modeling. LR-based regression indicates that CarpetDIEM metrics could be predicted with a reduced-order model with a root-mean-square error of 4.5 dB. After filtering the contaminating noise from QSF18 data, the error in that campaign is 7.4 dB. Thus, the ability to empirically model X-59 test flights is expected to be around 4-8 dB with the types of input data available during the two campaigns. Regarding numerical modeling, preliminary results here suggest opportunities for further PCBoom validation. Using LR on the difference between measured and PCBoom-predicted metrics suggests that meteorological and aircraft trajectory factors along with several other correlated factors are driving differences between measurements and PCBoom predictions.

The last set of studies deals with broader analysis and measurement issues related to community testing. Two investigations are related to fundamentals of boom processing. The first quantifies the impact of time-domain window shape on different loudness and sound exposure-based sonic boom metrics. As long as the window does not attenuate the primary shocks, the window shape is largely irrelevant. Second, a study of improving low-frequency spectral smoothness of one-third octave band spectra calculated from narrowband autospectra shows that the spectrum is sufficiently smooth provided that there is at least one narrowband spectral bin within each one-third octave band of interest. This finding provides guidance on the signal length – whether recorded or extended using zero padding – required for a given analysis.

One final R&D task, also in support of developing X-59 and broader community test methods, has been to explore greater compactness in a weather-robust, inverted microphone configuration with a ground plate and large-diameter windscreen. Prior designs developed and/or tested for a previous program were modified to investigate using a ground plate and windscreen with smaller diameters. Initial laboratory testing indicates greater plate scattering effects than prior designs, due to a smaller diameter (placing plate-edge diffraction closer to the microphone) and possibly thicker plate lip. Additionally, outdoor tests measuring wind pseudonoise reduction suggest that outer diameter is more important than windscreen thickness in driving wind noise reduction. The results guide ongoing development of ground-recording systems for X-59 community testing.

Introduction

Over the next few years, NASA will begin community noise testing with the X-59, the first supersonic aircraft developed to demonstrate sonic boom minimization through full aircraft shaping. The sonic booms (or “thumps”) the aircraft will produce represent a potentially major step toward eventual overland, commercial supersonic flight. These tests will take place in several different communities throughout the contiguous United States, and high-fidelity acoustic measurements will need to be made within urban environments. Although accurate sonic boom measurements are already challenging in any setting, measurements made in urban environments face additional challenges. These and other challenges related to acoustical measurements of the upcoming X-59 tests are the focus of the present research.

The first set of studies discussed in this report is contaminating noise corruption. During the Waveforms and Sonic Boom Perception and Response (WSPR) test, contaminating noise made a notable contribution to the Perceived Level (PL) metric value, particularly when the boom was quieter (Page *et al.*, 2014). Anticipating that the X-59 booms will be susceptible to the same type of contaminating noise corruption, Klos (2022) modified existing ISO 11204 standards to subtract the contaminating noise from the sonic boom spectra. Although the technique is generalizable to other types of recordings beyond sonic boom measurements, a method that is custom-created for sonic boom analysis will also be useful.

The second set of studies discussed in this report is sonic boom measurement variability. One factor that has long been known to distort sonic boom signatures is atmospheric turbulence (Hubbard *et al.*, 1964), and recently an entire measurement campaign was dedicated to studying turbulence effects on sonic booms (Bradley *et al.*, 2020). However, many factors ultimately affect measured sonic boom signatures. Changes in meteorology, aircraft trajectory, and environmental factors can all impact the boom loudness at the ground. Thus, a machine learning framework that is trained on data from recent flight tests can be useful for determining effects on boom metrics from individual factors as well as combinations of factors.

The third set of studies discussed herein is the possible standardization of signal processing methods and hardware for X-59 community noise testing. There is not yet a definitive recommendation for methods such as windowing or zero padding, and potential recommendations will be explored within this report. Additionally, the planned Phase 2 and 3 Ground Recording System (GRS) units presently lack a suitable microphone configuration that will be both weather-robust and reduce measurement artifacts from the microphone setup geometry. Previous designs have either been subject to ground reflections (Downs *et al.*, 2022) and/or have been insufficiently weather-robust (Page *et al.*, 2020). BYU has leveraged experience in weather-robust outdoor setups to provide recommendations for X-59 sonic boom measurement hardware.

This report is structured around the three aforementioned studies and is divided into three primary sections, discussing each study in turn. Section 1 discusses contaminating noise mitigation methods and then explores the effects of contaminating noise on metric calculations when not removed. Section 2 is focused on sonic boom variability. The effects of turbulence across a small linear array are discussed, and then a framework for determining additional important factors is laid out. This framework has led to important insights into measurement variability. Section 3 discusses proposed signal processing standards and testing related to outdoor measurement hardware. Section 4 provides a summary of the recommendations and provides contact information for finding future publications and results related to this research.

In addition to the main body of this report, there are also three appendices. These appendices are designed to archive important figures and results that did not fit in the main report body but will still be useful for future reference. Appendix A contains figures related to contaminating noise mitigation that are useful in understanding the variability in contaminating noise removal. Appendix B contains figures that demonstrate the effects of clipping for each sonic boom metric on both N-waves and shaped booms. Appendix C contains information on regression inputs discussed in Section 2.2 Lastly, Appendix D contains further analyses pertaining to measurement hardware design and testing that may be useful in guiding further experiments and analyses.

Section 1 – Contaminating Noise

1.1 Contaminating Noise Mitigation

(This section is largely identical to a portion of Anderson *et al.* (2024a)).

One of the important problems continuing to face outdoor sonic boom measurements is the local ambient and instrumentation noise (Page *et al*., 2014; Klos, 2020; Anderson *et al*., 2021; Klos, 2022, Anderson *et al.* 2024b). Noise can artificially inflate metric values, resulting in an overall bias error in sonic boom metric distributions. To compute accurate sonic boom metrics, this problem must be dealt with effectively.

The following method is proposed for removal of ambient and instrumentation noise (hereafter considered together under the term "contaminating noise") from sonic boom recordings:

1. Record 650-ms of contaminating noise before the boom, as well as a 650-ms recording containing the boom.
2. Calculate the contaminating noise and the boom spectra, then subtract them to calculate the signal-to-noise ratio (SNR) spectrum.
3. Determine the first OTO band center frequency at which the SNR becomes less than 3 dB. This becomes the filter cutoff or corner frequency.
4. Apply either a sixth-order Butterworth-magnitude filter (time domain) or a brick-wall filter (frequency domain) with the determined cutoff frequency from the previous step. For the brick-wall filter, the spectral data at the cutoff frequency are kept, and data at frequencies greater than the cutoff frequency are removed. Note that the Butterworth filter can be applied as two third-order magnitude filters (one forward and one backward) to produce a usable waveform with zero phase distortion. This can be done in MATLAB® r2022a via the *filtfilt* command.
5. Calculate metrics using the filtered data.

To demonstrate the success of this filtering approach, a detailed example is included in this report. For this example, we use a simulated NASA C609 low boom (Rallabhandi and Loubeau, 2022) and real-world contaminating noise recorded during QSF18. The simulated waveform is shown Figure 1.1(a) and is referred to as the "Clean Boom". The metrics calculated using this waveform are considered true because there is no contaminating noise. In Figure 1.1(b), 1300 ms of continuous contaminating noise has been superposed on the clean boom, with 650 ms occurring before the boom recording. The new 1300-ms recording is then split into the "Preboom Contaminating Noise" and the "Mock Recording".

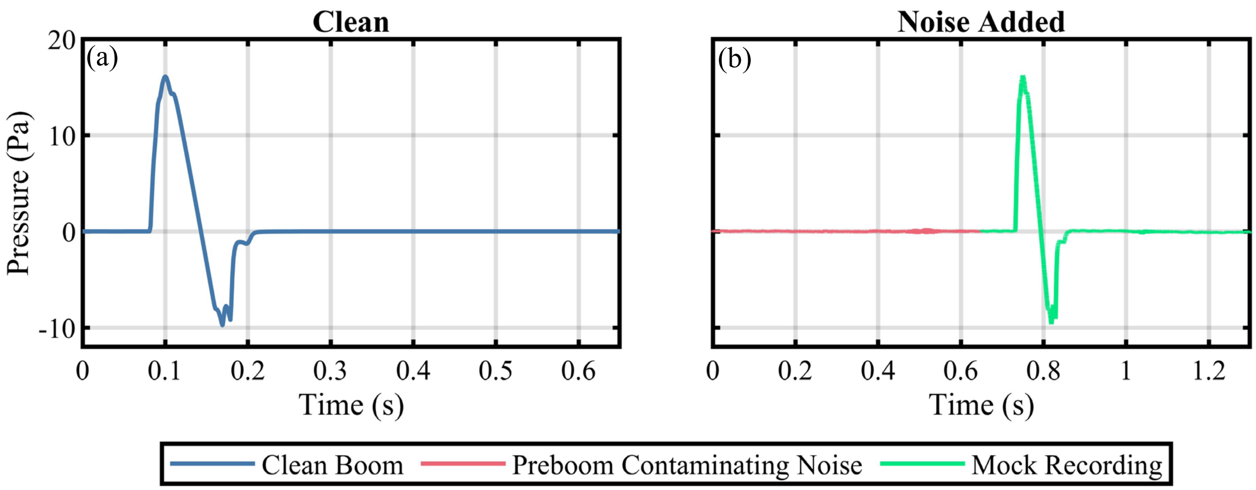

Figure 1.1. (a) A simulated low boom, known as the clean boom. (b) A total of 1300 ms of contaminating noise has been superposed on the clean boom, with 650 ms being placed before the start of the boom portion of the recording. The new waveform is 1300 ms in duration and can be split into a preboom contaminating noise phase and a mock recording phase.

The spectra for these waveforms are shown in Figure 1.2(a). Notice that the boom spectrum is dominant at low frequencies, and the contaminating noise spectrum is dominant at frequencies greater than a few hundred Hertz. Although there is sometimes contaminating noise due to wind, such effects tend to be at frequencies low enough to have a relatively minor effect on sonic boom metrics. Notice also that the contaminating noise is not stationary, causing the preboom ambient and mock recording spectra not to match perfectly at high frequencies. This effect can also be seen in Figure 1.2(b), which shows the SNR spectrum of the mock recording relative to the preboom contaminating noise. This nonstationarity is the reason that a purely spectral-subtraction-based method for contaminating noise removal was avoided when developing this method. Experience shows that although the contaminating noise is nonstationary, the method presented in this document tends to perform well.

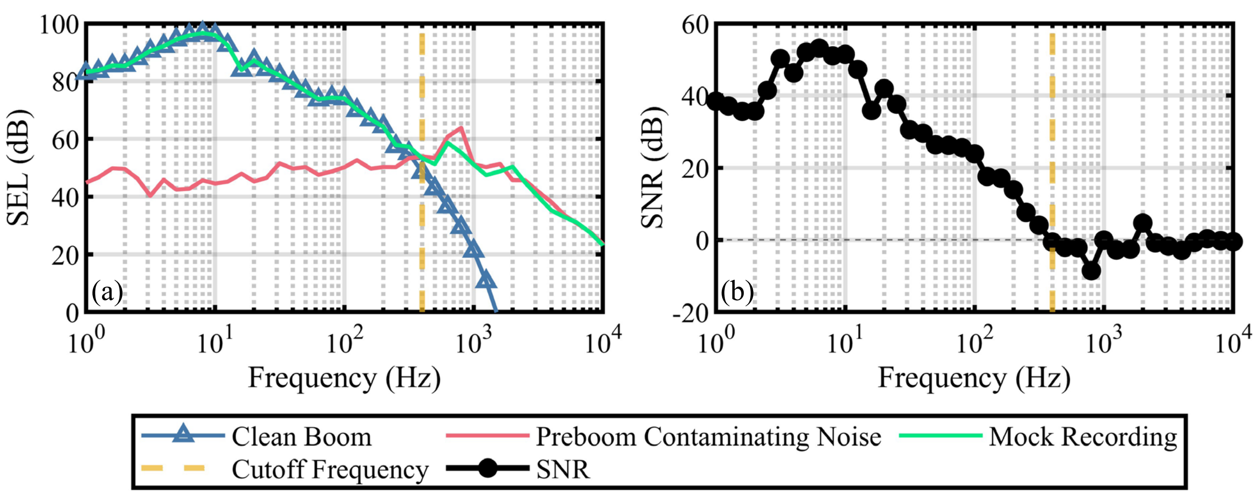

Figure 1.2. Determining the cutoff frequency. (a) The three spectra are plotted together. (b) The SNR between the Mock Recording and the Preboom Contaminating Noise is plotted.

What do the spectra look like after the filtering has been applied? Figure 1.3 contains the filtered mock recording results. Parts (a) and (b) show the flat-weighted spectral results for both the Butterworth and brick wall methods respectively. Parts (c) and (d) show the loudness spectra obtained as part of the PL metric calculation. For this example, the clean boom had a PL of 76.1 dB and the mock recording had a PL of 80.1 dB. The Butterworth filter brought the PL down to 76.0 dB and the Brick wall filter brought the PL down to 75.9 dB. Notice that both types of filters work well and returned the PL to within 0.2 dB of the clean case. Note also that because the brick wall filter performed similarly to the Butterworth filter, we can conclude that attempts to match the high-frequency spectral slope of the clean boom more closely are unlikely to yield large improvements. It is also important to note that this method, like other methods such as the methods proposed by Klos (2022), relies on the assumption that the contaminating noise is stationary. Additional limitations of the methods proposed in this report are that tonal noise can cause the filter cutoff frequency to be set to an unnecessarily low frequency and that results are limited to low-pass filtering.

This approach can be compared to another state-of-the-art technique. Klos (2022) proposed an adaptation of ISO 11204 (ISO11204:2010, 2010) that allows for more aggressive corrections than typically afforded by that standard. The most successful of the proposed adaptations are denoted "Custom E" and "Custom F". To make a direct comparison, a set of 300 simulated C609 low booms were randomly paired with contaminating noise recordings from QSF18. The differences between the filtered mock recording PL values and the clean boom PL values were calculated and are shown as histograms in Figure 1.4. Part (a) shows only the results using the ISO 11204 adaptations. Part (b) superimposes the results from the methods proposed in this report. All four methods successfully remove the contaminating noise for the PL metric. These methods should all continue to be studied once real low-boom measurements are available. It is possible that multiple methods ought to be used in tandem because they are likely robust to different types of errors.

Further details on the methods proposed within this section have been recently published in the Journal of the Acoustical Society of America (Anderson *et al*., 2024b).

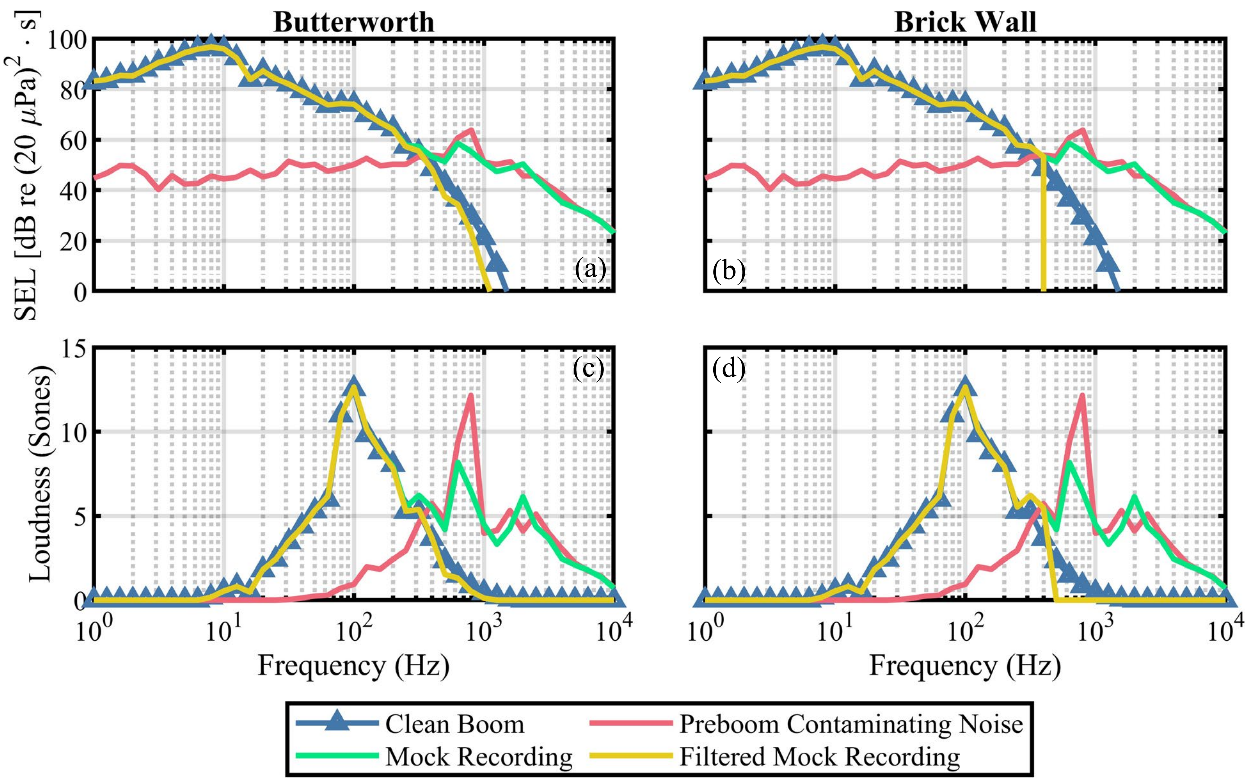

Figure 1.3. Applying the filters to the data: (a) the flat-weighted spectra using the Butterworth filter, (b) the flat-weighted spectra using the brick wall filter, (c) the loudness spectra using the Butterworth filter, and (d) the loudness spectra using the brick wall filter.

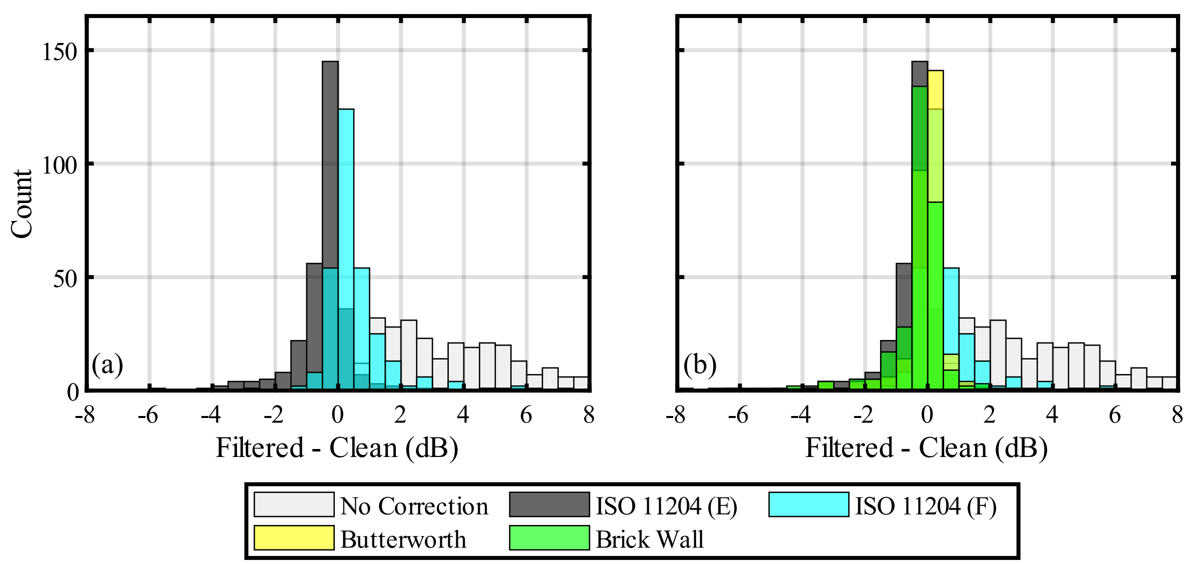

Figure 1.4. Comparison with the method proposed in Klos (2022): (a) the distribution of filtered metrics relative to the clean boom and (b) the same distributions, but with the filtering methods proposed in this report included. Note that the "No Correction" case extends beyond the plot limits up to a maximum value of +20.6 dB.

1.2 QSF-18 Dose-Response

One of the key goals of the X-59 program is to develop a dose-response curve for human annoyance as a function of sonic boom level. Previous dose-response curves have been created using the QSF18 dataset (Page *et al.*, 2020; Lee *et al.*, 2020), but this measurement included contaminating noise corruption because the measurements were made in urban environments. Contaminating noise increases the metric value above the true sonic boom loudness level, creating a bias in the dose-response curve. This brief study examines the effects of contaminating noise corruption on QSF18 measurements specifically and quantifies the potential impacts of contaminating noise corruption on the dose-response curve. The results help inform future X-59 dose-response curve analyses.

Removing contaminating noise from the data used to produce the dose-response curve shifts the entire curve to the left, and the shift is more dramatic for low PL values. This shift is derived from the results in Figure 1.5(a), where both the Butterworth filter and the ISO 11204 Custom F methods were used to remove contaminating noise from the data. Note that only booms with a PL SNR greater than 5 dB were included, as was done in Lee *et al.* (2020). Exponential curve fits are shown, which can be used to estimate the mean effects of contaminating noise for a given measured PL value during this specific field test. Both curves are then used to shift the dose-response curve obtained from Lee *et al.* (2020). These results are shown in Figure 1.5(b). As an example, the same annoyance level that was originally calculated to occur at 70 dB now occurs at 65 dB. It is noted that these results are limited to contaminating noise removal from measurements alone. The process used to calculate the dose at QSF18 (Page *et al.*, 2020) depended on much more than measurements alone. Therefore, the importance of contaminating noise removal is noted, but the full effects remain unknown until further testing can be done and the dose-response calculation methodology is finalized.

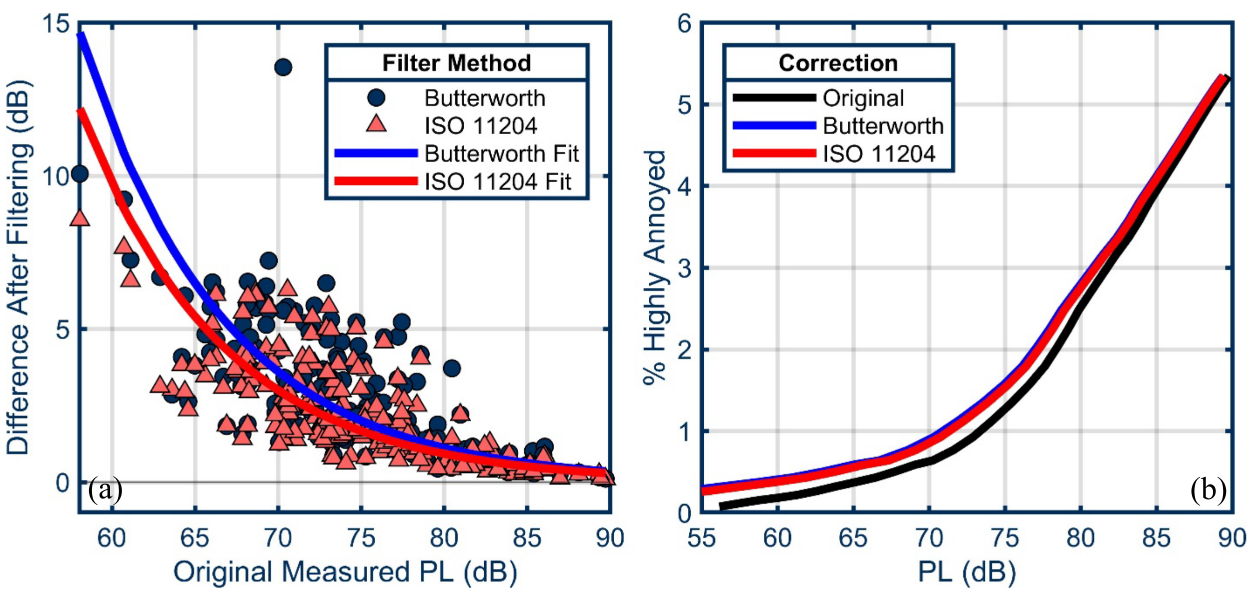

Figure 1.5. Adjusting the percent highly annoyed curve from Lee *et al.* (2020). (a) The change in the PL after removing contaminating noise shown as a function of the original, noisy PL. (b) The curve fits derived from (a) are applied to the dose-response curve.

It is also insightful to consider the different sources of QSF18 contaminating noise. For this analysis, only the BYU-fielded stations were used because they contain a wide variety of hardware configurations (Anderson *et al.*, 2022a). Creating a similar plot to Figure 1.5(a), but for the BYU stations and the Butterworth filter, Figure 1.6 shows the amount of contaminating noise removed as a function of the original measured PL. Although different representations may be useful, this current representation is sufficient for the current investigation. As was shown in Figure 1.5(a), the contaminating noise is more consequential for quieter booms than louder booms.

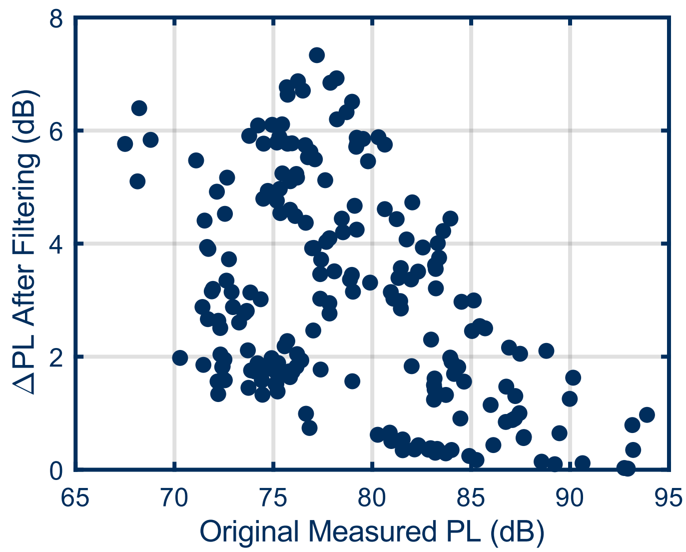

Figure 1.6. Change in PL after removing contaminating noise, shown as a function of the original unfiltered PL. This particular analysis used only BYU-fielded stations to enable a wider variety of hardware for comparisons.

Color-coding the dots shown in Figure 1.6 can help reveal potential trends in the contaminating noise effects. For example, Figure 1.7(a) colors the data according to measurement location. Notice that the cemetery location tended to have less contaminating noise than the park location, both of which make intuitive sense based on the expected contaminating noise levels in a cemetery and a park respectively. However, measurement location is not the only factor involved in determining contaminating noise levels. Figure 1.7(b) colors the data according to the DAQ card that was used in the measurement hardware. Here, the clear disparity between the NI 9250 and 9232 cards is due to the NI 9232[1] card having the highest electrical noise of the three cards and the NI 9250[2] being known to have the lowest while the NI 9234[3] card noise floor is in the middle.

These results are preliminary and indicate potential future research to be accomplished, as well as likely paths forward for reducing contaminating noise corruption in the X-59 tests. For example, putting the microphone in a park is likely to yield higher contaminating noise levels than in a quieter part of town like a cemetery. Additionally, the NI 9232 card should generally be avoided for quieter sonic booms because its larger input range results in higher electrical noise levels that interfere with the metric calculations.

[1] https://www.ni.com/en-us/shop/model/ni-9232.html

[2] https://www.ni.com/en-us/shop/model/ni-9250.html

[3] https://www.ni.com/en-us/shop/model/ni-9234.html

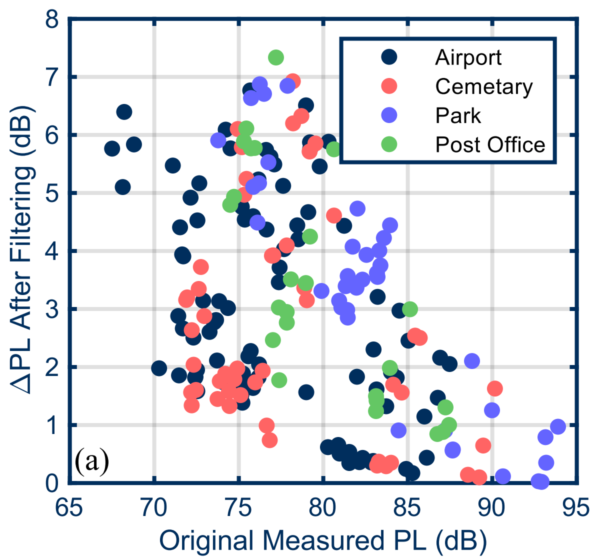

Figure 1.7. The change in PL after removing contaminating noise, shown as a function of the original unfiltered PL. (a) The data from Figure 1.6 have been colored according to measurement location. (b) The same data, colored according to DAQ card.

1.3 Applying CarpetDIEM-I Contaminating Noise to Simulated Low Booms

1.3.1 Using Measured Data

Quesst Phase 2 X-59 testing will occur in the desert environment near Edwards Air Force Base, CA. Although much quieter than an urban environment, measurements in this environment still contain contaminating noise. Therefore, previous recordings in this environment can inform future decisions regarding the effects of contaminating noise on Phase 2 testing.

To study the potential effects of contaminating noise on low-boom recordings, ambient recordings measured during CarpetDIEM I were superposed on 300 simulated X-59 C609 booms (Rallabhandi and Loubeau, 2022) to determine the effects of contaminating noise on the sonic boom metrics. The data were separated by microphone type to determine whether different microphone sensitivities resulted in a noticeable effect. Note that the microphones were distributed over NI 9232, 9234, and 9250 cards, the effects of which have been discussed in Section 1.2 above. This is expected to result in some degree of conflation between different measurement hardware, but this analysis should still indicate useful trends. Figure 1.8 shows the probability plots for the four metrics that were the most impacted by contaminating noise: PL, ASEL, ISBAP, and ESEL. The x-axes denote the differences produced in the metric values. Notice that the ambient recordings made using the PCB 378A07 resulted in the largest differences because of this microphone's lower sensitivity (~5 mV/Pa) compared to the GRAS 47AC (~8 mV/Pa) and the GRAS 46AE (~50 mV/Pa). Figure 1.9 shows the same type of plots for the four studied metrics that were the least impacted: BSEL, CSEL, DSEL, and ZSEL. Note that the CSEL and ZSEL are not in the final list of candidate metrics, but are included here for completeness only. Although there appears to be slightly more impact on the metric values when using the PCB 378A07 microphone for these metrics, all differences are generally within 1 or 2 dB. All of these results can be traced back to the fact that the highly-affected metrics all contain greater high-frequency weighting than the less-affected metrics, indicating that the highly-affected metrics are being disturbed by the high-frequency electronic noise floor within the contaminating noise. Table 1.1 contains statistical descriptions of all metric distributions.

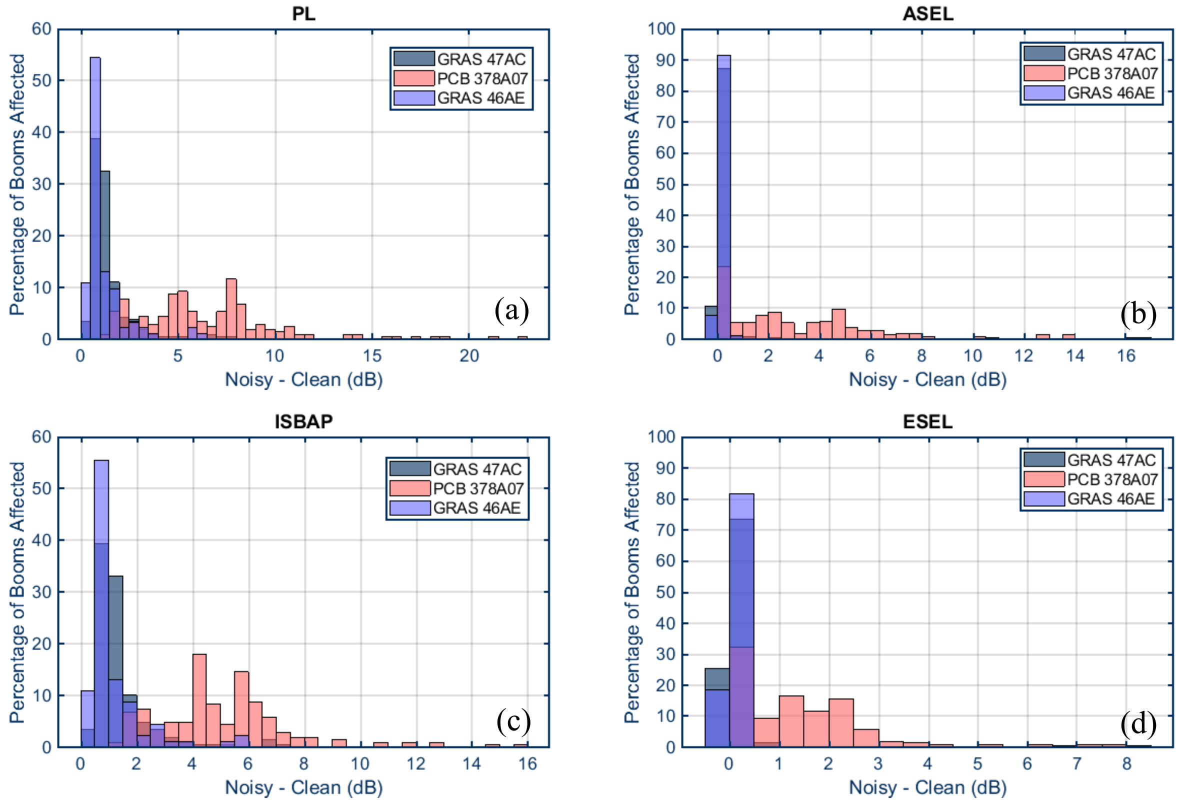

Figure 1.8. Effects of contaminating noise on C609 simulated low booms for different weighted metrics. The data are separated by microphone type. The "Percentage of Booms Affected" axis indicates the percent (out of 100) of data points that fall in each bin.

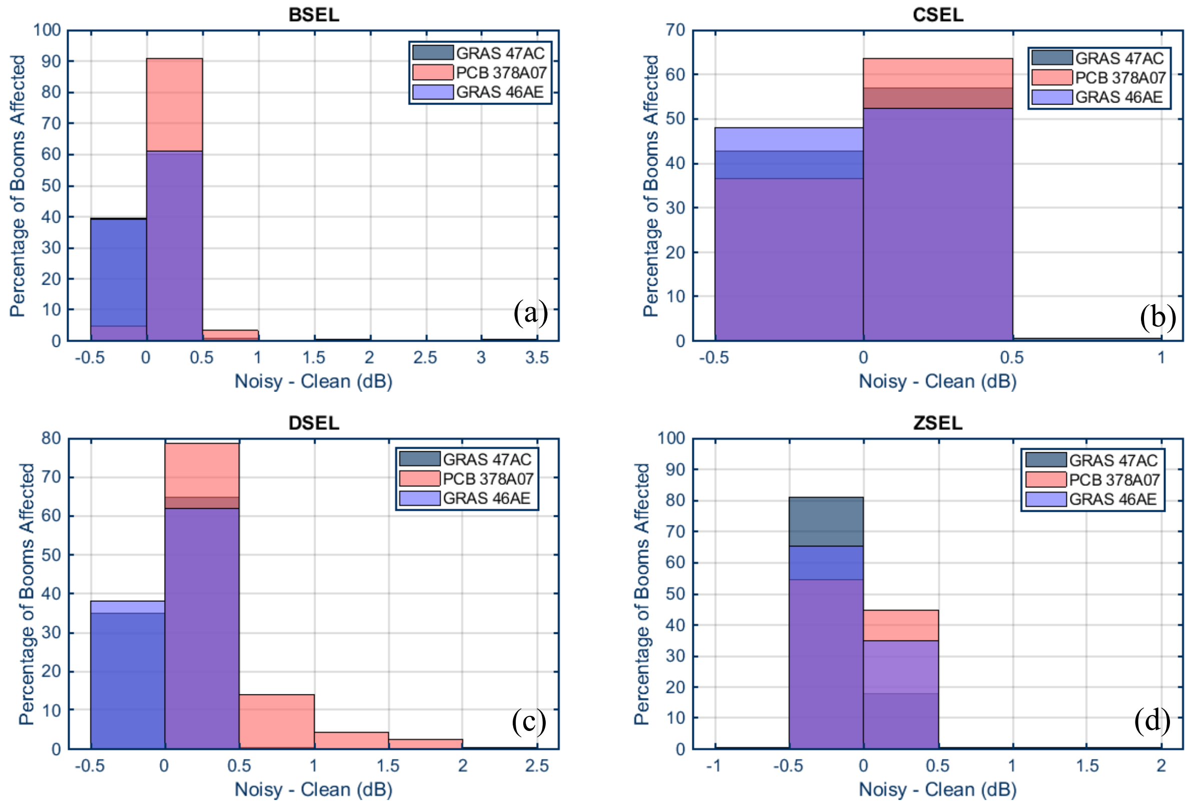

Figure 1.9. Effects of contaminating noise on C609 booms for different weighted metrics. The data are separated by microphone type. The "Percentage of Booms Affected" axis indicates the percent (out of 100) of data points that fall in each bin.

Table 1.1. Mean and standard deviation values calculated from the histograms in Figure 1.8 and Figure 1.9.

Metrics	GRAS 46AE		PCB 378A07		GRAS 47AC	
	Mean (dB)	Std. Deviation (dB)	Mean (dB)	Std. Deviation (dB)	Mean (dB)	Std. Deviation (dB)
PL	1.1	1	6.7	4	1.3	1.1
ISBAP	1.1	0.9	5.2	2.5	1.3	1.04
ASEL	0.04	0.1	3.6	3.6	0.06	0.3
BSEL	0.004	0.03	0.1	0.2	0.02	0.2
CSEL	0.0006	0.01	0.006	0.02	0.01	0.1
DSEL	0.001	0.009	0.4	0.5	0.01	0.1
ESEL	0.01	0.03	1.6	1.8	0.03	0.2
ZSEL	-0.004	0.04	0.1	-0.0005	0.003	0.2

1.3.2 Brown Noise / Simulated Wind Noise

Although useful data were collected at CarpetDIEM for evaluating the contaminating noise due to measurement hardware, the wind conditions during CarpetDIEM were calm. To explore the effects of wind pseudonoise on low-boom recordings, brown noise was added to the simulated C609 booms. The brown noise levels were set to approximately match the results shown in Jones *et al.* (2020) for a wind speed around 10 m/s (~20 mph). Figure 1.10 shows an example spectrum where this brown noise was superposed on the clean boom to create a noisy boom. Notice that the brown noise only affects the spectrum notably at low frequencies, indicating that metrics that weight low frequencies higher will be more affected by this added noise.

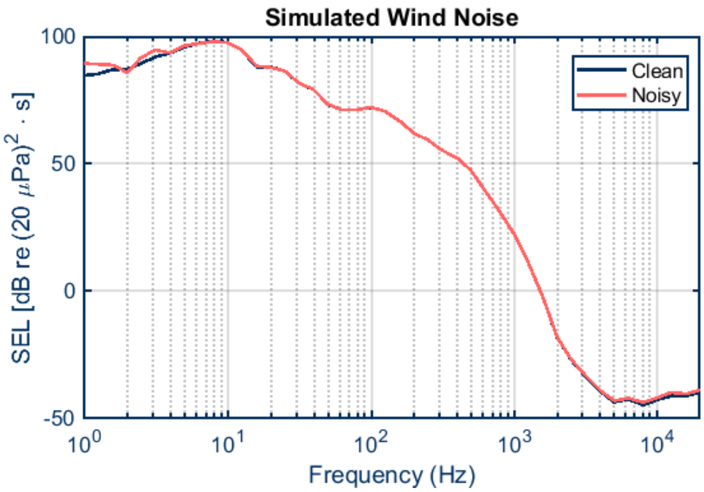

Figure 1.10. Spectra depicting a C609 boom before and after simulated wind noise application.

Repeating this same process for all 300 simulated C609 booms enables a statistical representation of the approximate effects of wind noise on sonic boom metrics. This is shown in Figure 1.11 and Figure 1.12. Notice that all metrics are affected by less than 0.5 dB with the exception of ZSEL, which is expected given its equal weighting across frequencies. Therefore, for sonic boom human perception metrics (PL, ISBAP, ASEL, BSEL, DSEL, ESEL), the effects of moderate wind pseudonoise are considered negligible.

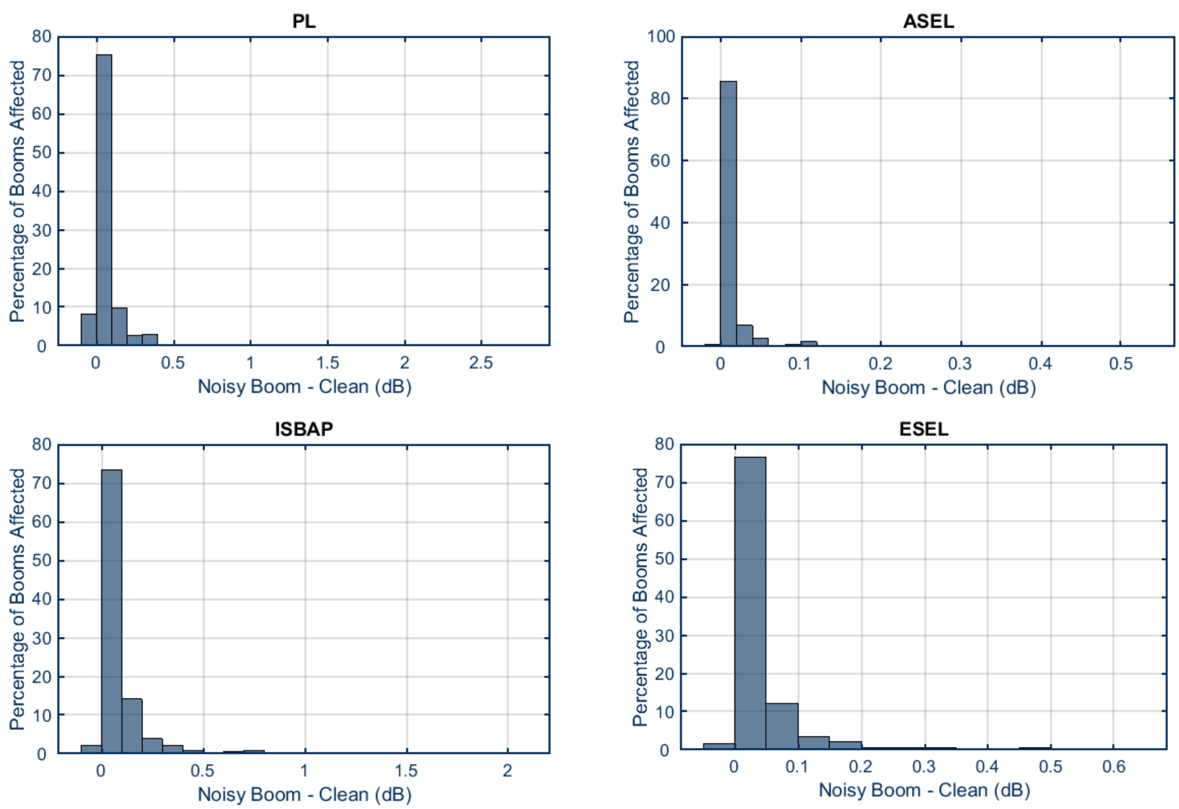

Figure 1.11. Effects of wind noise on different weighted metrics. The x-axes show the difference between the noisy boom and the clean C609 boom. The "Percentage of Booms Affected" axis indicates the percent (out of 100) of data points that fall in each bin.

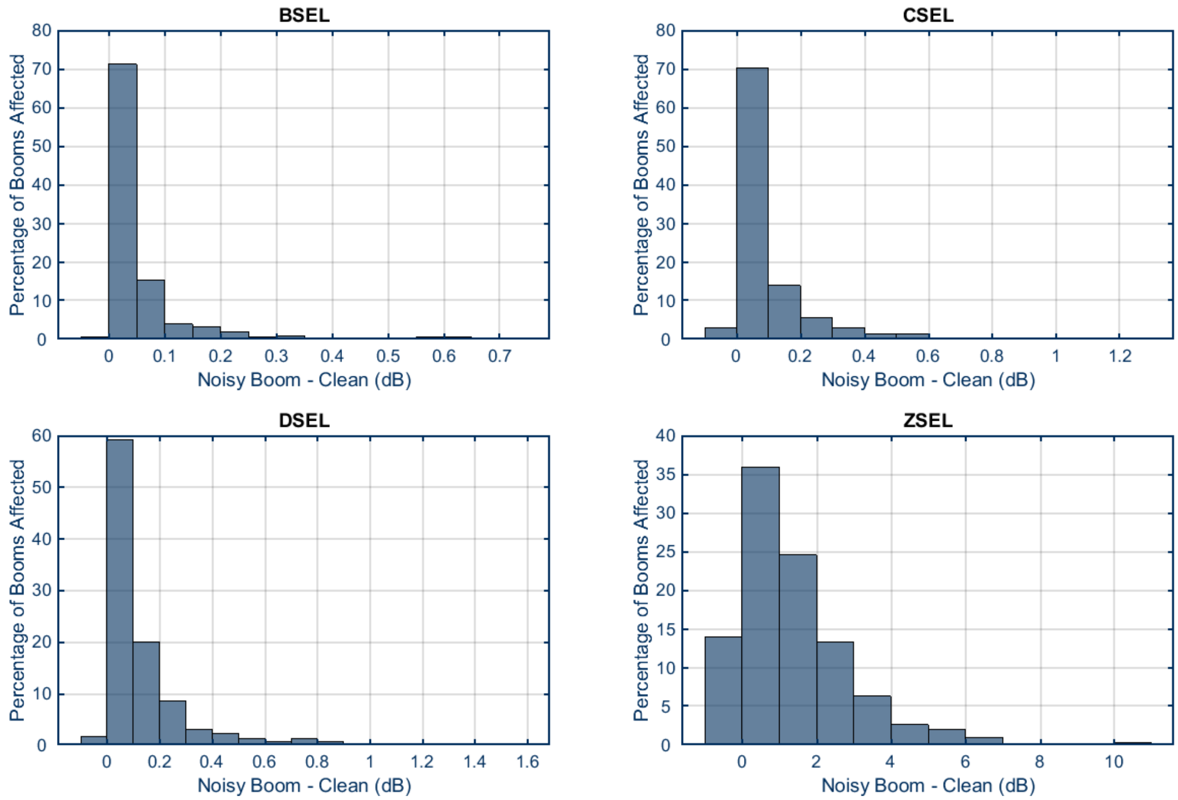

Figure 1.12. Effects of wind noise on different weighted metrics. The x-axes show the difference between the noisy boom and the clean C609 boom. The "Percentage of Booms Affected" axis indicates the percent (out of 100) of data points that fall in each bin.

Section 2 – Analysis of Boom Variability

2.1 Turbulence-Induced Variability

(This section contains portions that are largely identical to material found in Anderson *et al.* (2024a))

Meteorological effects on sonic boom measurements have been studied for decades (Maglieri *et al*., 2014). Of particular interest is the lowest portion of the atmosphere, known as the atmospheric boundary layer, where turbulence can be much greater than at higher altitudes. Turbulence may cause sonic boom waveforms measured over short distances to vary dramatically. To investigate turbulence effects on sonic booms further, BYU fielded a seven-microphone 400-ft (120-m) linear turbulence array directly under the flight track at CarpetDIEM (Durrant *et al*., 2022). The array was oriented perpendicular to the flight track.

Figure 2.1 shows the sonic boom from a single flyover measured at all seven microphones along the array. Notice the large visual differences between the waveforms across the array. Because the microphones are close together relative to the aircraft altitude, the differences across the array cannot be due to large-scale atmospheric differences, but rather to smaller-scale atmospheric turbulence.

These differences translate into sonic boom metric variability, as indicated in Figure 2.2(a) for the PL metric. This includes booms from three supersonic overflights (A, B, and C). Each overflight is unique and shows different amounts of variability across the array. When considering the mean metric value for a boom, the confidence interval on that mean value varies with the amount of scatter. For example, Boom A has a narrower confidence interval width than Boom B. The benefit of analyzing the variability in the confidence interval widths is to demonstrate that the scatter in the data can vary dramatically between booms. Figure 2.2(b) illustrates this for each metric. The metrics across the array for twelve booms at this station were calculated and the confidence interval (CI) half-widths for each metric for each boom were also calculated. The results can be interpreted as follows: the PL 90% confidence interval half-width (i.e., mean ± CI/2) was sometimes as narrow as 0.6 dB, but sometimes as wide as 2.7 dB. The choice to use 90% confidence intervals is done in this analysis to enable comparison with Doebler (2017), where favorable agreement is found between this work and Doebler (2017). All other confidence intervals in this report use the 95% confidence interval. While these results are all for N-waves, these methods may be useful when studying measurements of low booms. It is therefore recommended that during X-59 testing, similar results be obtained by using multiple microphones at a single location to experimentally determine the variability due to atmospheric turbulence.

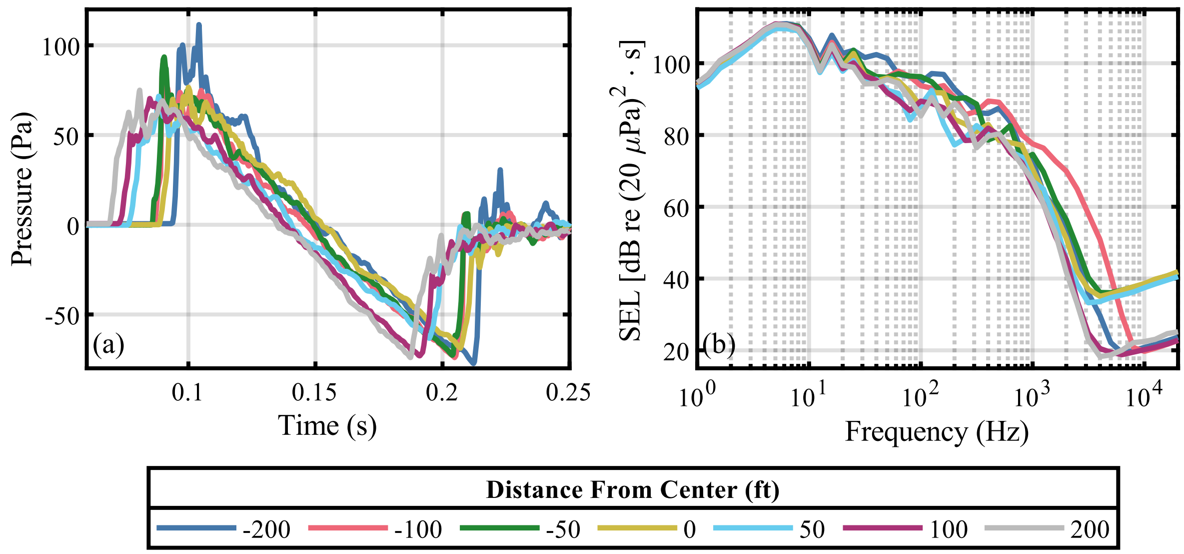

Figure 2.1. (a) Example waveforms measured across the turbulence array for a single boom event. (b) Corresponding spectra for the booms shown in part (a).

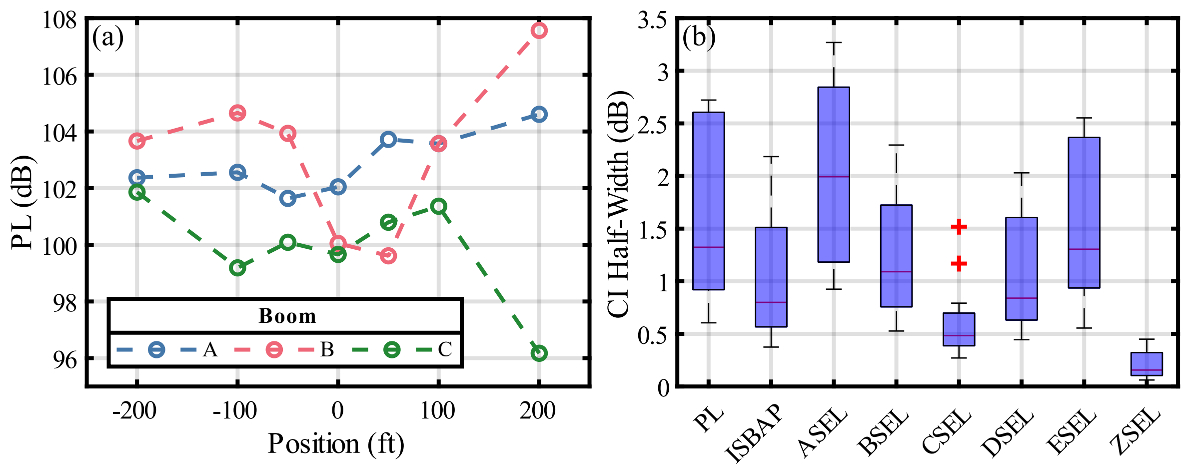

Figure 2.2. The effects of atmospheric turbulence on sonic boom metrics. (a) The PL metric for three example overflights varies widely across the array and each boom is unique. (b) Each overflight (N=12) has a unique confidence interval half-width for each metric mean value. Twelve overflights each with 7 boom measurements were used to calculate 90% confidence interval half-widths for each boom for each metric, and the results are shown as a box and whisker plot with the medians shown by a horizontal line. Red plus signs indicate outliers, and the red bars indicate the median values.

2.1.1 Effects of Clipping on Sonic Boom Measurements

During the CarpetDIEM measurement campaign, 11 of the 23 booms measured at the turbulence array were clipped on at least one channel because higher-sensitivity microphones were used (Gee *et al.*, 2020). In the preceding discussion, any boom where a channel clipped was entirely thrown out so that each boom maintained the same number of channels. This brings up the question to what extent clipping impacts the sonic boom metrics. Two example booms are shown in Figure 2.3. These booms are representative of the amount of peak-pressure clipping generally seen across the array. The remainder of this section is devoted to completing a more-general investigation, using clipping amounts well beyond what was actually observed at

CarpetDIEM I. This analysis is demonstrated in Figure 2.4. Parts (a) and (b) show a CarpetDIEM and C609 boom, respectively, with varying amounts of artificial peak-amplitude clipping, defined as a percentage of the peak pressure amplitude that has been removed. Part (c) shows the impact on each metric value as a function of the clipping percentage for the measured CarpetDIEM boom and part (d) for the simulated C609 boom. Interestingly, the CarpetDIEM boom can remain within 1 dB of the unclipped metric values with up to 20% peak-amplitude clipping. This indicates that the booms with minor clipping (judged to be < 20%) can still be included in further analyses alongside the unclipped booms. The C609 boom behavior when clipped is also interesting. Because the clipping introduces artificial high-frequency content, several metrics actually increase in level with the introduction of waveform clipping. Overall, even minor clipping can produce large effects on low-boom levels, meaning that measurement hardware should be chosen to avoid this possibility. This must be balanced with the need to reduce contaminating noise from the measurement hardware, as discussed in Section 1.

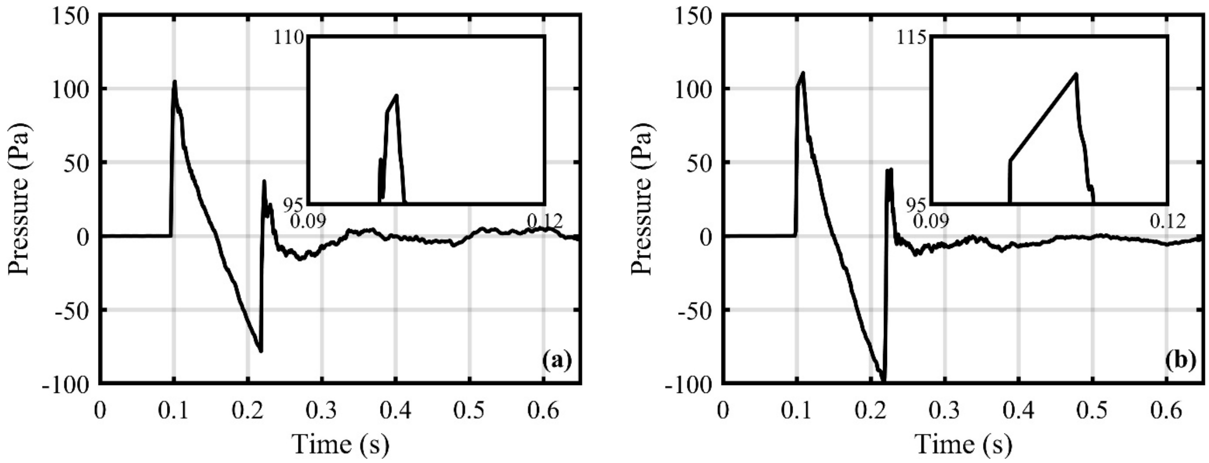

Figure 2.3. Example waveforms of what was deemed (a) minor clipping and (b) major clipping. Boom (a) was deemed acceptable for metric calculations, but boom (b) is on the edge of what might be useful for metric calculations.

An additional useful analysis is to determine the spread of the metric changes over a variety of boom waveforms. For this analysis, 231 booms measured at CarpetDIEM along the entire measurement array of several miles (Durrant *et al.*, 2022) and 300 simulated C609 booms were modified with artificial clipping at different levels as shown in Figure 2.4. These results are shown in Figure 2.5 for the PL only. Notice in part (a) that the CarpetDIEM PL values are almost always decreased by clipping and that the changes remain, on average, within about 1 dB up to 20% clipping. This indicates that CarpetDIEM N-wave data with minor clipping can be treated just like unclipped data when calculating metric values as long as 1 dB bias error is considered acceptable. Similar results indicating that minor clipping can often be neglected can be seen in Gee *et al.* (2013). Notice also in Figure 2.5(b) that the C609 PL tends to increase a few decibels on average, even for clipping values greater than 40%. These plots have been created for all metrics and can be found in Appendix B.

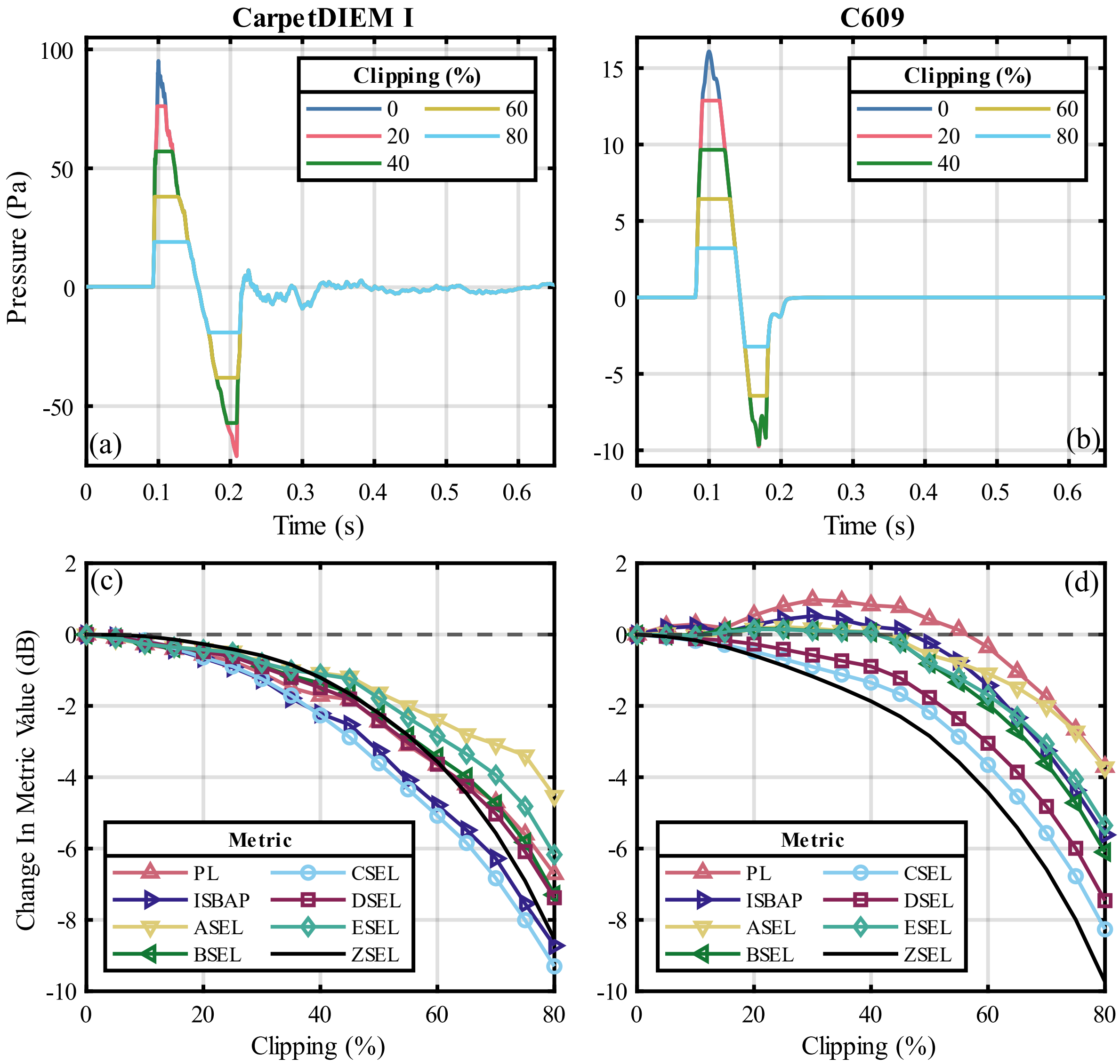

Figure 2.4. (a) Effect of clipping (percentage of peak pressure amplitude) on a CarpetDIEM waveform. (b) An example C609 boom simulation clipped at different values. (c) The change in metric values as the CarpetDIEM boom is clipped by various amounts, (d) The change in metric values as the C609 boom is clipped by various amounts.

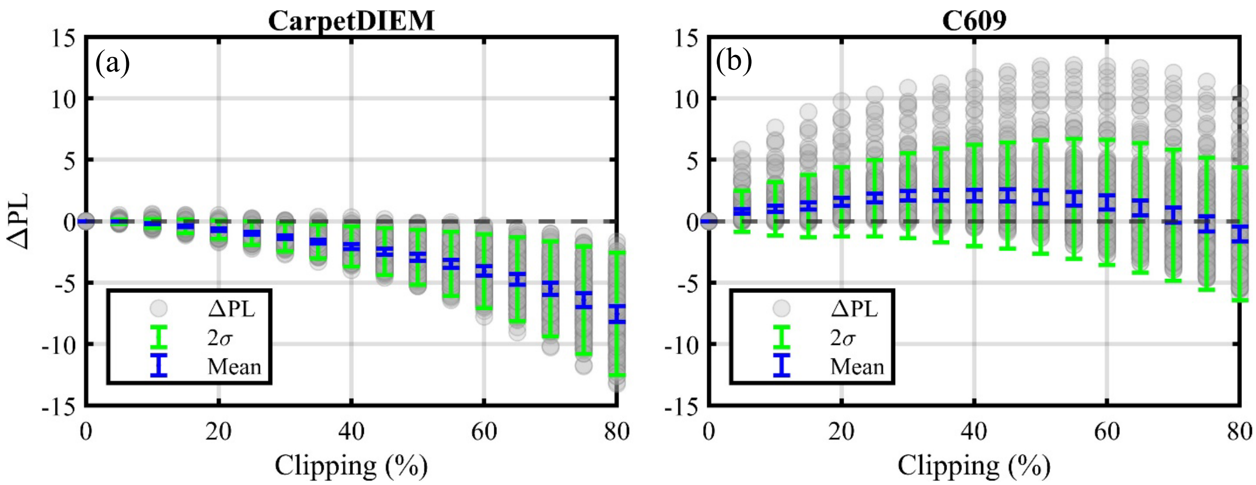

Figure 2.5. Clipping effects for (a) 231 CarpetDIEM booms and (b) 300 C609 booms, shown as a function of the clipping percentage. ΔPL represents the difference between the clipped-boom PL and the unclipped-boom PL. Negative values indicate that the PL was decreased by the clipping. Individual metric differences at specific clipping percentages are represented as dots. Twice the standard deviation of the distribution of data points at each clipping percentage is indicated by the green bars. The blue bars represent the 95% confidence interval for the mean value of the distribution at each clipping percentage.

2.2 Lasso Regression Analysis of Measured and Modeled Sonic Boom Metric Variability

2.2.1 Introduction

With the X-59 scheduled to take its first test flights in the coming years, NASA has been actively preparing by conducting several flight test campaigns with other supersonic aircraft. These flight test campaigns serve as risk-reduction exercises that prepare NASA and its partners to make safe, accurate measurements of X-59 sonic booms and associated community response. Through these campaigns, NASA has also been developing and testing its sonic boom prediction capabilities, mainly through the use of its sonic boom prediction software suite, known as PCBoom (Page *et al.,* 2023, Lonzaga *et al.*, 2022).

Much work has gone into developing codes like PCBoom that predict boom metrics by modeling waveform propagation through the atmosphere to the ground (Lonzaga *et al.,* 2020). However, recent flight tests contained larger-than-expected variability both in the measured sonic boom metrics at the ground and the accuracy of the PCBoom predictions when compared with ground measurements (Durrant *et al.,* 2021a). Thus, this section has two main goals: 1) identify the factors behind the variability in the measured metrics at the ground and 2) identify the factors behind the discrepancies between measured and predicted metrics. Variability in the measured metrics is referred to simply as "measured metric variability" whereas the difference between the measured and PCBoom-predicted metrics is referred to as ΔPM, signifying the difference between Predicted and Measured metrics. It is important to note that the PCBoom predictions used in this analysis did not include the effects of turbulence. Additionally, PCBoom is only as good as its inputs, so large ΔPM values do not necessarily correspond to an error by PCBoom, but could be due to errors in inputs such as near-field pressure data, aircraft trajectories, atmospheric data, etc.

To accomplish these goals, this section uses a different approach than traditional sonic boom prediction codes. The framework proposed here does not attempt to model the generation and propagation of a boom through the atmosphere to the ground. Rather, it uses empirical data, such as atmospheric and flight trajectory data, as inputs to a Least absolute shrinkage and selection operator (Lasso) Regression (LR) model (Tibshirani, 1996) that returns a reduced-order model (ROM). This ROM is fit using input factors that are the primary contributors to either measured metric variability or ΔPM. This method is different than the focus of previous work in sonic boom modeling and preparation for X-59 testing, but it is also built using data from previous NASA flight test campaigns.

Specifically, the LR framework developed in this report uses data from two recent flight test campaigns that differ significantly in their test environment and measurement setup. One flight test campaign used in this report, dubbed Quiet Supersonic Flights 2018 (QSF18), took place in November 2018 in Galveston, Texas (Page *et al.,* 2020). This test aimed to measure the community response to 'low booms', or booms that are about as quiet as X-59 booms are predicted to be (Doebler and Rathsam*,* 2019). To produce these low booms, NASA pilots flew an F/A-18 in a low-boom dive maneuver over the ocean between 20-50 km off the shore of Galveston. These booms were measured at 11 different microphone stations located around the Galveston area, and the associated community response was gathered and correlated with the booms. The data from this campaign have proven to be extremely useful, as it is one of the only sources of low-boom recordings in a heavily-populated area.

Another flight test campaign, dubbed Carpet Determination In Entirety Measurements (CarpetDIEM I), took place in 2019 in a much different environment than QSF18 (Durrant *et al.,* 2021b). At CarpetDIEM I, NASA pilots flew an F/A-18 at cruise conditions over a lateral array of microphones in the desert near Edwards Air Force Base in California. These booms were much louder than the booms recorded at QSF18 and contained much less contaminating noise. Additionally, this test provided logistical lessons for NASA and its partners as they prepare to measure the acoustics of the first X-59 flights at this same location in the coming years.

While both of these test flight campaigns have already provided valuable lessons and preparation for the upcoming X-59 community tests (Downs *et al.,* 2021; Anderson *et al.,* 2021; Anderson *et al.,* 2022b; Durrant *et al.,* 2021b), questions remain about the large amounts of variability in the measured sonic boom loudness metrics. Both QSF18 and CarpetDIEM contain amounts of metric variability beyond the expected loudness differences due to changes in boom propagation distance. Variability on the order of 10 dB or more was seen at QSF18 for flights where booms were generated the same distance from a microphone station. At CarpetDIEM each flight was nominally the same, but variations in loudness metrics at the same microphone station were also measured to be at least 8 dB in some cases. Additionally, ΔPM values using the PCBoom 6.7 PCBurg module at these flights were as high as 20 dB with a root mean-square error (RMSE) between 5-10 dB.

The upcoming community tests of the X-59 will rely on accuracy both in predicted and measured metrics, and thus the factors that cause boom metrics to be louder or quieter in each test location need to be thoroughly investigated and understood. This section aims to understand the factors that drove the metric variability at the QSF18 and CarpetDIEM tests individually, as well as to understand which factors affect boom metrics generally and thus could apply to future flight test campaigns in different environments. Additionally, this section seeks to determine which of these factors may be driving ΔPM, although this application of LR is still preliminary and under development.

To accomplish these goals, this section develops a framework using LR to analyze the QSF18 and CarpetDIEM datasets. LR is a technique that is useful for eliminating irrelevant factors from a large group of input factors. LR allows the user to input all potentially relevant data and discover which factors are the best predictors of output variability (in the measured sonic boom loudness metrics or ΔPM). This creates a ROM that is more easily understood and interpreted than a model with dozens of input factors. The ROM factors can then be investigated further to determine the physical reasons for their impact on measured metric variability and/or ΔPM.

This section's scope is limited to identifying potential factors contributing to measured metric variability and ΔPM, as well as suggesting possible physical reasons for their impact. This section does not seek to develop a new prediction tool or advocate for the creation of a ROM for each new X-59 flight test. Rather, the results should help NASA, its partners, and the sonic boom community at large better understand measured metric variability and ΔPM, both of which are critical to accomplishing the objectives of the Quesst mission. However, it may be worth considering the use of the LR approach as an aid to preflight planning of the X-59 tests in the event that measured doses are significantly different from planned doses as the community test progresses.

The rest of this section is organized as follows. Subsection 2.2.2 introduces the LR method used to obtain a ROM that predicts sonic boom metrics from ambient, aircraft trajectory, and meteorological data. Subsections 2.2.3 and 2.2.4 use this method to create a ROM for the CarpetDIEM and QSF18 flight tests and then analyze the selected inputs to determine possible physical reasons for their selection. Because the QSF18 dataset contains a large amount of contaminating noise, a filtering method is used to remove the contaminating noise, and the results are re-analyzed. Both datasets create a ROM with an RMSE of around 4.5 dB unless contaminating noise filtering is applied, in which case the RMSE for QSF18 is increased to 7.4 dB. Next, Subsections 2.2.5 and 2.2.6 use this same LR framework but use ΔPM as the output instead of the measured metrics. Preliminary results identify potential factors driving ΔPM, but future work is needed to verify and expand upon these results.

2.2.2 Lasso regression framework

While several regression methods were tested for use in this analysis (including elastic net regression, ridge regression, and random forest among others), LR was chosen due to its clarity of results and ease of use. For this analysis, the built-in MATLAB® function for Lasso Regression (MathWorks®, 2023) is implemented with just a few lines of code. The equation for LR is given as Eq. (1), where the first summation is least-squares minimization in multiple dimensions. In Eq. (1), y is the output, x is the input factor (such as meteorological, aircraft trajectory, or ambient data), and β is the coefficient that is multiplied by the input to obtain the prediction with the lowest squared error when every input is summed up. After this summation, there is an added penalty that drives more unimportant inputs to zero as the penalty factor, λ, is increased over each iteration. Thus, LR removes factors that minimize its loss of predictive capability.

$$Minimize\left(\sum_{n=1}^{N}\left(y_n - \sum_{j=1}^{J} x_{nj}\beta_j\right)^2 + \lambda_i \sum_{j=1}^{J} |\beta_j|\right) \tag{1}$$

When LR is performed in MATLAB®, λ is increased over 100 iterations until no inputs remain by iteration 100. The user can take the remaining inputs at any iteration, essentially choosing how many inputs they desire in their ROM. However, to find the iteration that gives the best predictions, model validation at each iteration is required.

K-fold cross-validation is one method to determine the λ value that produces the best model and has become common practice for users of LR (Obuchi and Kabashima, 2016; Chetverikov *et al.,* 2020). At each iteration, the data are randomly separated into k subsets, with one subset used for validation and the rest used for training. This is repeated k times so that each subset is used once for validation. As cross-validation is done on every iteration in MATLAB®, the user can track the validation RMSE and look for a minimum value. The remaining inputs at this iteration can then be identified. If a sparser model is desired, the user can also find the inputs remaining at a later iteration where more inputs have been zeroed-out.

Figure 2.6 shows an example of 10-fold cross-validation. Going from left to right, the penalty factor, λ, is increased until a minimum RMSE is found at the red dotted line. This is the point where many unimportant inputs have been zeroed-out, creating a robust predictive model (by avoiding overfitting). Past this point, even more inputs are zeroed-out, but this increases the cross-validation RMSE (due to underfitting). Error bars above and below each point show the standard error for each iteration's cross-validation. 'XVal' in the legend means K-fold cross-validation.

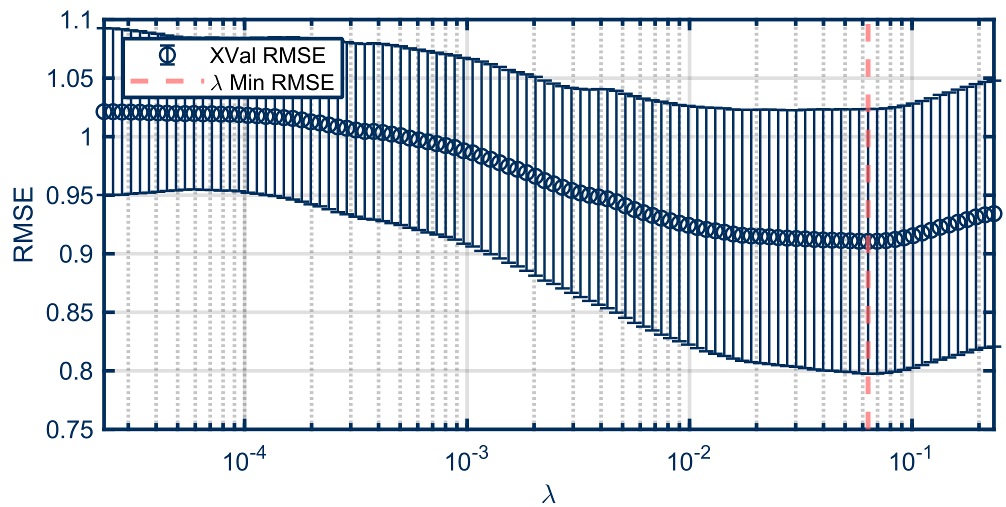

Figure 2.6. Example: 10-fold cross-validation (XVal) is performed at each iteration of LR as the penalty parameter, λ, increases. Increasing λ forces more unimportant input coefficients to zero until a minimum prediction RMSE is found at the red dotted line. Past this point, more inputs are removed and the RMSE increases.

LR with 10-fold cross-validation is used on both the CarpetDIEM and QSF18 datasets. This allows for an analysis of the flight tests individually as well as a comparison between the two flight tests to discover if any factors are significant in both flight tests, which had different environments. In both tests, the Perceived Level (PL) metric is used as the output for measured metric variability, and ΔPM is used to investigate predicted metric variability. While PL is just one of several candidate en route supersonic aircraft noise certification metrics, the results across all metrics are similar. It is also important to note that more input factors are passed into LR for CarpetDIEM than for QSF18, as will be discussed in the next two sections.

2.2.3 CarpetDIEM-measured Sonic Boom Metric Variability

A total of 68 inputs are used in the LR for CarpetDIEM. These inputs include meteorological, aircraft trajectory, contaminating noise, and PCBoom predictions. Meteorological data (e.g., wind speed, temperature, pressure, etc.) come from ground weather stations near the microphone locations as well as from pre-flight weather balloons launched to gather atmospheric data for PCBoom. Additionally, modeled turbulence parameters are used, taken from the Climate Forecast System Version 2 (CFSv2) (Saha *et al.,* 2014). As-flown aircraft trajectory data such as Mach number, heading, flight path angle, and their derivatives are also passed in as input factors. Two sets of contaminating noise metrics are calculated, one set for the 650 ms immediately preceding the boom and another set averaged over the 60 seconds before the boom. Finally, PCBoom predictions for each metric are also used as potential predictors for LR. The inputs are normalized to a mean of 0 and a standard deviation of 1, allowing a comparison of coefficient magnitudes. For a full list of inputs, outputs, their descriptions, and correlations for the inputs, see Appendix C.

The results from 10-fold cross-validated LR at CarpetDIEM are given below in Figure 2.7. Here, a minimum PL RMSE of 4.5 dB is achieved at a λ value of 0.21. This accuracy is slightly better than the PCBoom prediction accuracy (ΔPM) at CarpetDIEM, which had an RMSE of 5.1 dB. Error bars for the cross-validation (XVal) encompass values almost 2 dB above and below the mean at this iteration.

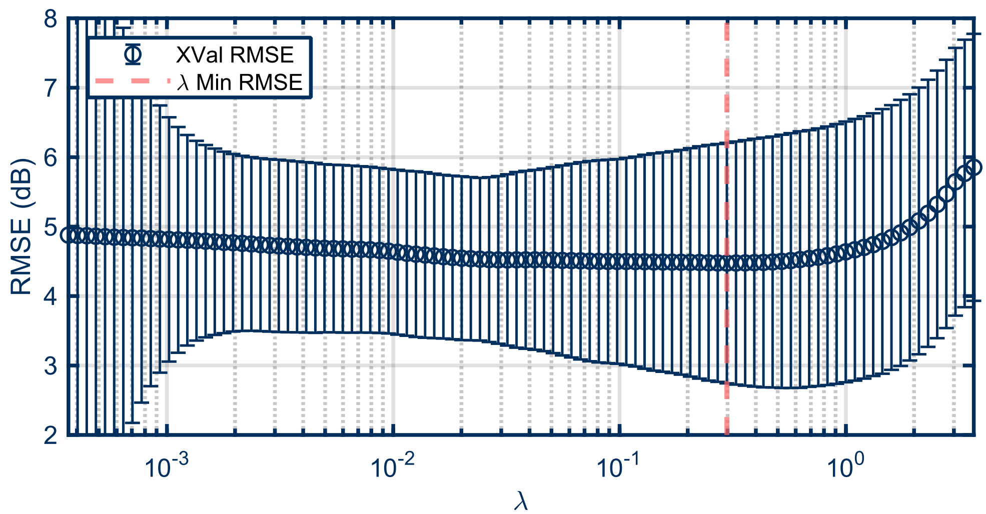

Figure 2.7. Cross-validation results for CarpetDIEM show a minimum PL RMSE of 4.5 dB is achieved at a λ value of 0.21.

Now that the λ value corresponding to the minimum RMSE has been found, the remaining inputs at this iteration can be identified. These inputs are given below in Table 2.1, along with their regression coefficient from the linear regression ROM. Normalization of the inputs to mean zero and standard deviation of unity allows direct comparison of the coefficient magnitudes. A negative coefficient means a negative correlation between a quantity and PL. Here, Wind Direction (as measured by ground weather stations), Temperature (also measured by ground weather stations), Mach Derivative (which captures the change in Mach number at the time of ray emission), and Straight-line Distance (the distance between aircraft and ground recording station at the time of ray emission) have negative coefficients and thus correspond to a decrease in the PL. Conversely, Friction Velocity (a measure of turbulence in the atmosphere, obtained from the CFSv2), Flight Path Angle 2nd Derivative (a measure of the aircraft's up-down tilt 2nd time derivative at the time of ray emission), PCBoom DSEL (PCBoom-predicted D-weighted Sound Exposure Level at each station), Ambient ASEL (measured over 650 ms before the boom), and Ambient DSEL (averaged over the 60 seconds before the boom) have positive coefficients and thus correspond to an increase in the PL.

Table 2.1. CarpetDIEM remaining inputs after LR with their associated coefficient.

Input Name	Coefficient
Straight-line Distance	-1.9
PCBoom DSEL	1.6
Ambient DSEL (60 s)	0.50
Mach Derivative	-0.4
Flight Path Angle 2nd Derivative	0.2
Ambient ASEL (0.65 s)	0.048
Wind Direction	-0.047
Temperature	-0.044
Friction Velocity	-0.041
RMSE	**4.5 dB**

Several of these factors, such as Straight-line Distance, are intuitive, but others, such as the aircraft trajectory inputs, are unexpected. The CarpetDIEM flights were all nominally cruise booms with similar trajectories, so changes in aircraft trajectory were expected to have minimal effect on the boom PL at the ground. Another interesting result from Table 2.1 is that PCBoom DSEL is chosen instead of PCBoom PL when the output is PL. However, these two inputs are highly correlated, so LR could likely have chosen either PCBoom DSEL or PCBoom PL and obtained a similar result. Eliminating correlated inputs is one of LR's strengths, as long as the user remembers that LR will not return all strong predictors if they are correlated to another strong predictor.

To visualize the LR process and weighting for each input, Figure 2.8 contains a colormap tracking each input's coefficients through all 100 iterations. Dark blue colors indicate when a variable is zeroed-out, whereas red colors indicate when a variable is given a large coefficient. Several inputs, such as Friction Velocity, are zeroed-out, but are later brought back into the model, showing how different combinations of inputs are chosen each time λ increases. While many other inputs were considered in LR, this figure only shows those inputs whose coefficient is non-zero at the iteration corresponding to the minimum RMSE, which is indicated by the vertical dashed line. As the λ value continues to increase in iterations past this line, more inputs are eliminated until just PCBoom DSEL and Straight-line Distance remain at iteration 84. By iteration 98, only Straight-line Distance remains.

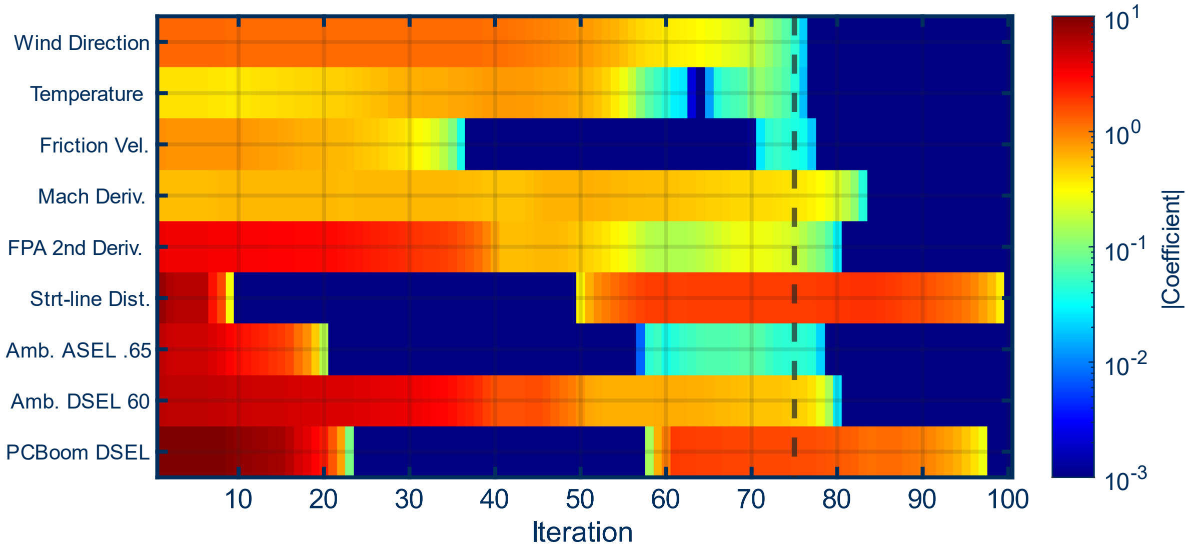

Figure 2.8. Colormap of the inputs' coefficients chosen by LR through 100 iterations in MATLAB® for the CarpetDIEM campaign. The iteration corresponding to the minimum RMSE is indicated by a vertical dashed line.

The fact that several flight trajectory inputs are present in the ROM warranted further investigation. CarpetDIEM flights were nominally cruise booms, but Figure 2.9 shows this was not the case for some booms. The aircraft trajectory is plotted and colored by Mach number with blue dashed lines connecting PCBoom-predicted ray emission points to the ground recording station where the boom was measured. For flight 5, pass 2, the aircraft was both decelerating and turning as rays were still being emitted to the undertrack microphone stations. The results from LR in Figure 2.8 and Table 2.1 suggest that this change in aircraft trajectory had significant impact on the measured sonic boom metrics. Similar inputs will also be seen to influence the ΔPM values at CarpetDIEM in Subsection 2.2.5 below. It will be important for the X-59 to remain on-condition longer for the Phase 2 flights.

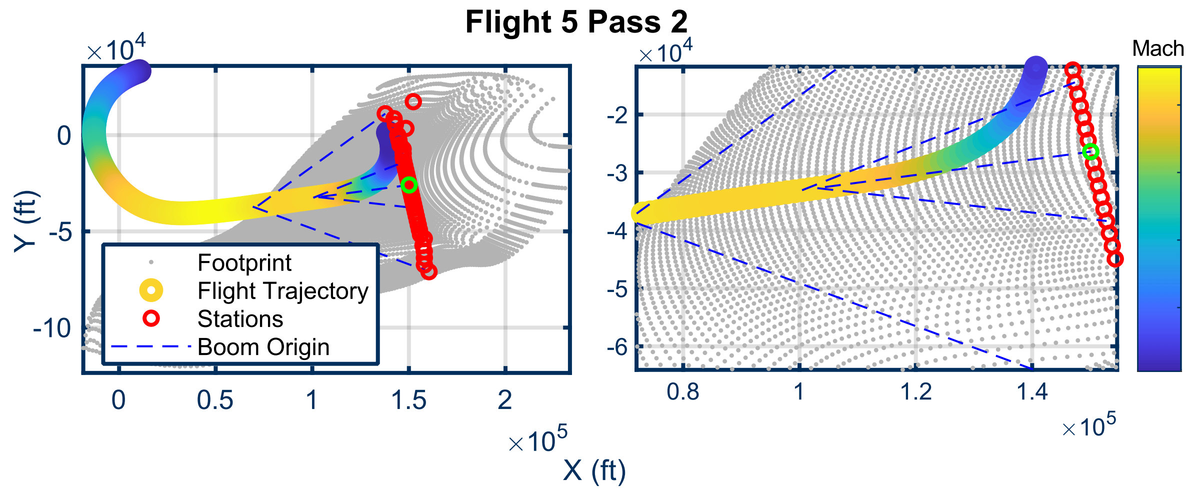

Figure 2.9. Aircraft trajectory is plotted going from left to right and colored by Mach number. Blue dashed lines connect the PCBoom-predicted ray emission points to the microphone recording station that measured the boom on the ground. A zoomed-in view shows an unsteady trajectory while rays are still being emitted.

In summary, at CarpetDIEM, two aircraft trajectory inputs (Mach Derivative and Flight Path Angle Second Derivative) were chosen by LR, which was unexpected until further investigation showed the trajectories to be unsteady at the time of ray emission. Several meteorological factors were chosen by LR, but all contained low-magnitude coefficients. Finally, Straight-line Distance was chosen as the last remaining input over any PCBoom prediction and was shown to produce a better fit than PCBoom DSEL. This result helps motivate Subsections 2.2.5 and 2.2.6 in this report, which investigate ΔPM variability.

2.2.4 QSF18-measured Sonic Boom Metric Variability

The QSF18 flight test campaign differed from the CarpetDIEM campaign in two ways relevant to this analysis: a low-boom dive maneuver was used to achieve quieter booms, and the measurement was made in a high-noise environment. Because the low-boom dive maneuver only flies supersonic for a short period at a specific location, aircraft trajectory inputs are averaged over the dive rather than taken at an instant in time, as was the case at CarpetDIEM. Additionally, at the time of this analysis, only PCBoom PL predictions were conveniently available, whereas for CarpetDIEM multiple PCBoom metrics for several different runs of PCBoom were used as inputs to LR. Because of these differences, the QSF18 dataset uses just 35 inputs, much fewer than the 68 used for CarpetDIEM, largely due to fewer aircraft trajectory and PCBoom inputs. However, similar to CarpetDIEM, meteorological inputs from ground weather stations, weather balloons, and the CFSv2 are used. Additionally, contaminating noise is passed in as a potential factor, and its influence is seen to be much bigger at QSF18 than at CarpetDIEM. The inputs, outputs, their descriptions, and the input correlations for QSF18 can also be found in Appendix C.

Running LR with 10-fold cross-validation at QSF18, as shown in Figure 2.10, results in a 3.9 dB minimum RMSE at a λ value of 0.008. However, this minimum RMSE is achieved at an early iteration where few of the 35 inputs have been zeroed out. Thus, for this case, a later iteration with a λ value of 0.50 is used to identify the most important factors. This iteration is chosen because it has just four inputs remaining, yet it still maintains an RMSE within 0.2 dB of the minimum. At this iteration, designated by a blue dashed line in Figure 2.10, fewer inputs remain than at the minimum RMSE iteration, but prediction accuracy is 4.1 dB.

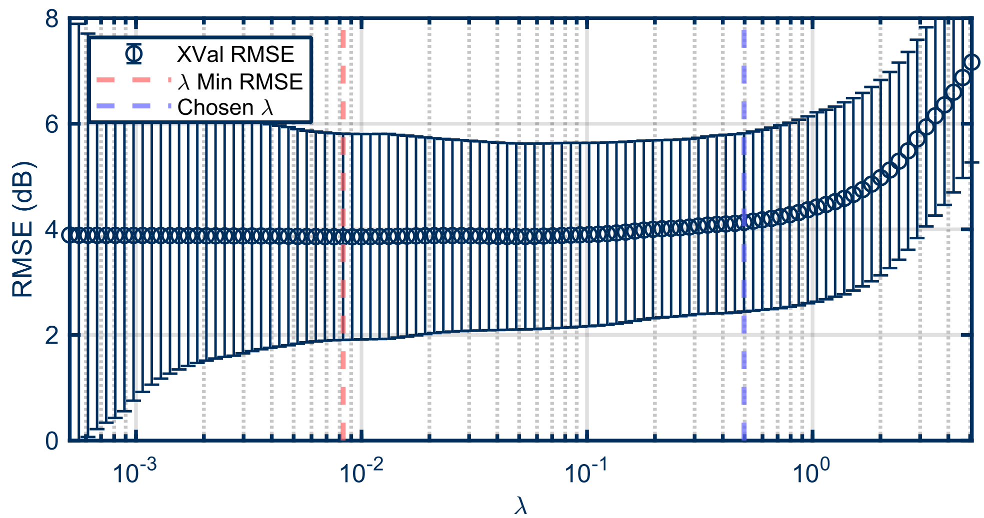

Figure 2.10 Cross-validation results for QSF18 show a minimum PL RMSE of 3.9 dB is achieved at a *λ* value of 0.008, but because so many inputs remain at this iteration, a later iteration is chosen with a *λ* value of 0.50.

Table 2.2 gives the remaining inputs and their coefficients at λ = 0.50. Here, Horizontal Distance (a measure of the distance between the aircraft's coordinates and the microphone station coordinates that does not consider altitude) is the only input left with a negative correlation to PL. Conversely, Heading (the aircraft's heading angle), Dive Depth (a measure of the altitude lost during the aircraft's supersonic dive), and Ambient PL (calculated over 650 ms before the boom and containing both ambient and instrumentation noise) are positively correlated with PL. The Heading coefficient can be misleading; this result does not suggest a larger heading angle always creates louder sonic booms, it merely suggests that at this particular flight test the supersonic dives with a larger Heading angle tended to create louder booms, perhaps because they were pointed more towards the microphone stations. The Heading angle ranges from 298-341 degrees in the dataset. The top correlates for Heading, given in Table C.3, are the locations of the aircraft at the time of ray emission in the x- and h-directions.

Table 2.2. QSF18 remaining inputs after LR with their associated coefficient.

Input Name	Coefficient
Horizontal Distance	-4.5
Ambient PL	2.3
Heading	0.54
Dive Depth	0.18
RMSE	**4.1 dB**

These four factors' coefficients are tracked through all 100 iterations in Figure 2.11. Here, λ = 0.50 at iteration 75, which is the iteration used for Table 2.2. Each input has a non-negligible coefficient, but Horizontal Distance and Ambient PL are shown to have coefficients several times larger than either Heading or Dive Depth. This means that LR is largely depending on just two inputs, Ambient PL and Horizontal Distance, to achieve its prediction accuracy of 4.1 dB RMSE.

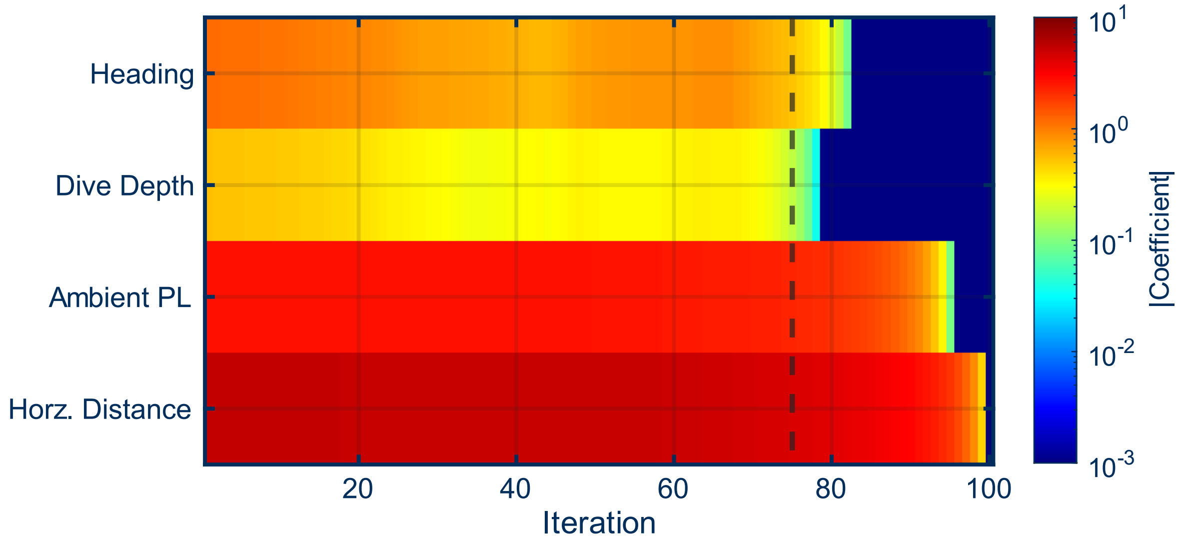

Figure 2.11. Colormap of the inputs' coefficients chosen by LR through 100 iterations in MATLAB® for the QSF18 campaign. The iteration corresponding to the minimum RMSE is indicated by a vertical dashed line.

Contaminating noise was high at QSF18, and thus provides a high noise floor which may lower prediction error. Because Ambient PL is calculated over the 650 ms immediately preceding the boom, only a couple of boom PL values were quieter than the Ambient PL. This can be visualized in Figure 2.12, where a line corresponding to PL = Ambient PL is plotted with a dashed line. This lower limit imposed by contaminating noise makes it easier for Lasso to predict metrics with a lower RMSE. Additionally, a fit line shows a strong correlation between Ambient PL and the measured boom PL.

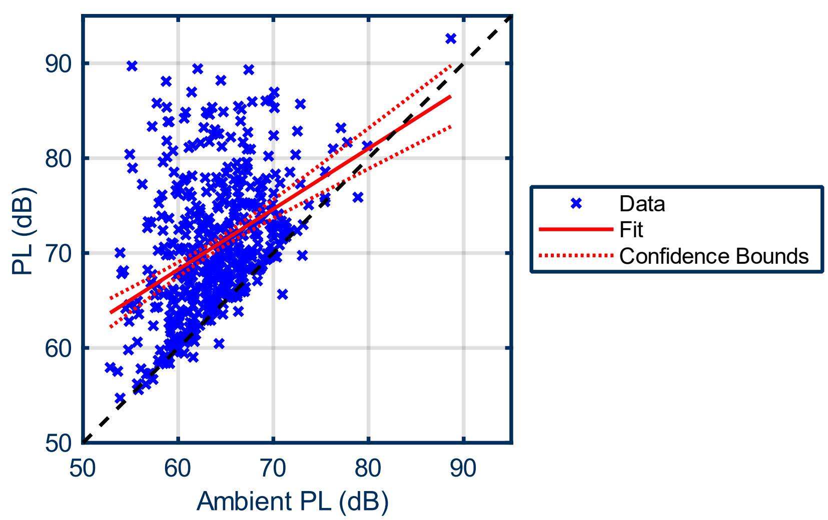

Figure 2.12. A linear fit for Ambient PL and measured boom PL is established, showing a strong correlation between the two with very few booms having louder contaminating noise than measured boom PL.

Although LR is able to predict metrics with a low RMSE by using contaminating noise, more insight is gained by removing the contaminating noise from measurements using the Butterworth filter method from Section 1. This allows LR to identify additional input factors that influence boom metrics that were obscured by the high levels of contaminating noise. After applying the contaminating noise filter, LR is rerun on the dataset through the same process, this time arriving at the results presented in Table 2.3. Several new inputs, such as Aircraft Tail # (an indicator of which of two aircraft at QSF18 was used for each boom), Wind Direction (measured at the nearest ground weather station), Atmospheric Boundary Layer Height (acquired from CFSv2), Average Mach (the aircraft's Mach number averaged over the dive portion of its trajectory), and Angle (the difference between the aircraft's heading and the angle pointing towards the microphone station) are chosen by LR now that contaminating noise has been filtered out. The inputs with a negative coefficient have a negative correlation with PL. The selected iteration for Table 2.2 and Table 2.3 is the same, so more inputs are present after filtering not because a different iteration was chosen, but because the contaminating noise filter was applied.

Table 2.3. QSF18 (with contaminating noise filtering) remaining inputs after LR with their associated coefficient.

Input Name	Coefficient
Horizontal Distance	-9.6
Heading	1.5
Wind Direction	-0.81
Dive Depth	0.45
Atmospheric Boundary Layer Height	0.35
Aircraft Tail #	-0.27
Angle	-0.24
Average Mach	0.11
RMSE	**7.4 dB**

After filtering, the model relies heavily on the Horizontal Distance input to predict the PL (its coefficient is more than 6x greater than the next largest coefficient). This process is seen in the colormap in Figure 2.13, where it has the largest coefficient through all iterations and is the last to be zeroed out. Its coefficient is consistently larger than any other input throughout all 100 iterations. Atmospheric Boundary Layer Height is correlated with turbulence, which can distort boom waveforms. The Wind Direction could influence boom PL by blowing the rays towards or away from the stations, depending on the wind speed present for each boom. However, these meteorological inputs are not kept through all iterations and are assigned small coefficients in the end. Thus, even when contaminating noise is filtered out, Lasso only identifies small effects from meteorological inputs at QSF18.

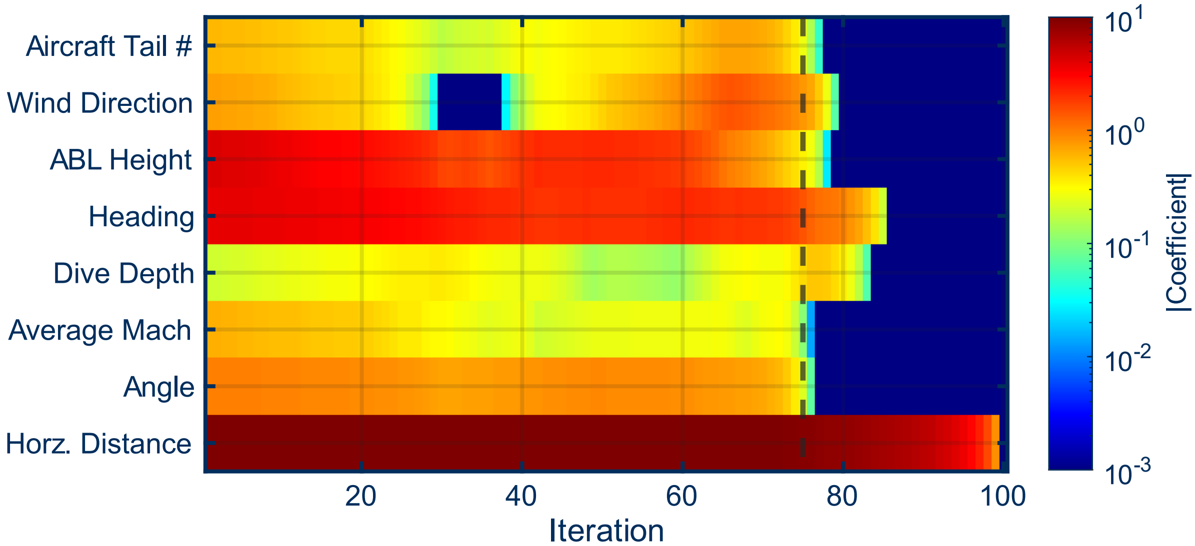

Figure 2.13. Colormap of the inputs' coefficients chosen by LR through 100 iterations in MATLAB® In Subsection 2.2.5 for the QSF18 campaign after filtering out contaminating noise.

In summary, the same LR framework has been carried out at QSF18 as was done at CarpetDIEM. Results show that LR is able to predict metrics with a 4.1 dB RMSE by using mostly contaminating noise and distance input factors. The Butterworth filter method from Section 1 has been used to remove the contaminating noise and discover more subtle influences from other factors. Several more meteorological and aircraft trajectory factors have been identified, but the model's prediction accuracy decreases after the ambient filter is applied and relies mostly on a distance factor to predict metrics.

2.2.5 CarpetDIEM Modeled Sonic Boom Metric Variability

The same methods used to analyze measured metric variability can now be used to analyze the difference between predicted and measured metrics, or ΔPM. For this section and the next, the same LR framework is used, except that the output (y in Equation (1)) is now ΔPM instead of measured PL. K-fold cross-validation is still used to identify the best model through 100 iterations in MATLAB®.

Before giving the results for LR when used to identify input factors driving ΔPM, a brief overview of PCBoom predictions is given below in Figure 2.14 and Figure 2.15. Figure 2.14 shows a distribution of ΔPM values from the CarpetDIEM measurement campaign when PCBoom was run using as-flown flight trajectory data. CarpetDIEM's ΔPM values have an RMSE of 5.1 dB and a mean error of 1.1 dB. This is an improvement from the ΔPM values at QSF18, which have an RMSE of 8.7 dB (3.6 dB higher than CarpetDIEM) and a mean error of 6 dB (4.9 dB higher than CarpetDIEM).

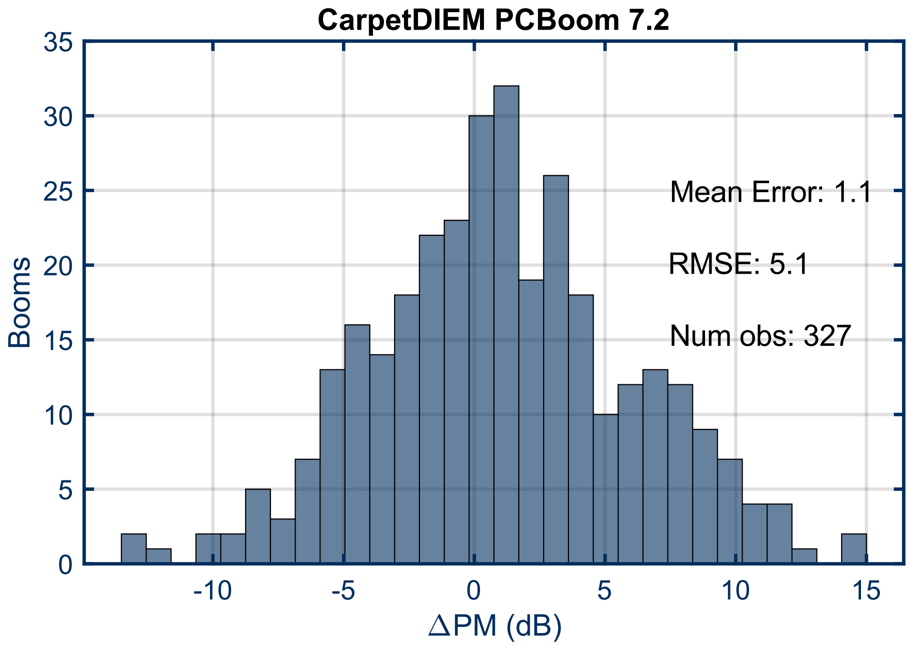

Figure 2.14. A histogram of ΔPM values shows a distribution with an RMSE of 5.1 dB and a mean error of 1.1 dB.

Several PCBoom near-field inputs were tested as part of this analysis, although none included turbulence effects. Figure 2.15 plots four booms from CarpetDIEM with their measured waveform, predicted waveform from the default F-function input, and predicted waveform from a CFD near-field input from the SonicBAT campaign. Because the F-function input leads to modeled metrics that match the measured metrics the best, it is used in this analysis. The waveforms in Figure 2.15 show how the predicted waveforms differ from the measured waveforms in appearance (due in large part to turbulence) and in PL. Some of the predicted booms overpredict the loudness, some underpredict, and some are within 1 dB. Large values of ΔPM tend to come from recordings made near the edge of the array, such as at Boom 21 at Station 20 in the figure.

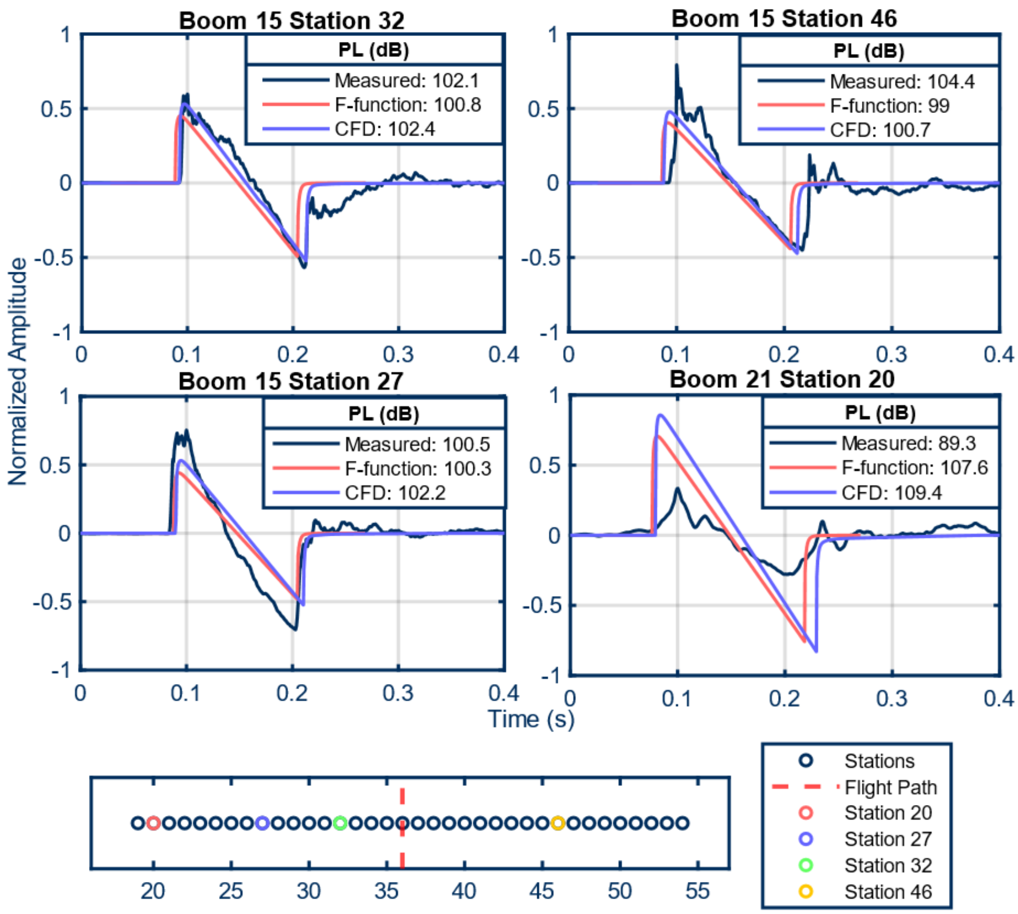

Figure 2.15. Four booms are shown with their measured waveform, predicted waveform with the default F-function, and predicted waveform with a CFD near-field input. A schematic of the station layout with nominal flight path is given below the waveforms.

Although this analysis is preliminary, insights are still obtained by examining the results of LR for ΔPM. Table 2.4 gives the remaining input factors from LR at CarpetDIEM and their associated coefficients. This table shows a variety of factors influence ΔPM, including aircraft trajectory factors, meteorological factors, and contaminating noise. Interestingly, Heading Derivative is given the largest positive coefficient, indicating that larger heading derivatives correspond to larger positive ΔPM values. Meteorological factors include an input from a high-altitude balloon measurement, a low-altitude balloon measurement, a ground weather station, and one from the CFSv2 modeled data. Additionally, contaminating noise is given a negative coefficient, indicating that louder contaminating noise corresponds to lower (more negative) ΔPM values. This makes sense given that contaminating noise can increase the loudness of the boom, making the ΔPM (predicted minus measured) values more negative. Overall, this model predicts ΔPM values with an RMSE of 4.5 dB.

Table 2.4. CarpetDIEM ΔPM remaining inputs after LR with their associated coefficient.

Input Name	Coefficient
Heading Derivative	2.1
Straight-line Distance	1.8
High Altitude Pressure	-1.5
Flight Path Angle 2nd Derivative	-1.3
Relative Humidity	-1.0
Avg. Ambient DSEL	-0.6
Low Altitude Dew Point	-0.5
Mach 2nd Derivative	-0.4
Abs. Value Emission Angle	-0.4
Mach Derivative	0.2
Friction Velocity	-0.2
RMSE	**4.5 dB**

2.2.6 QSF18 Modeled Sonic Boom Metric Variability

Next, LR is run on the QSF18 dataset, again using ΔPM as the output factor to capture input factors driving modeled sonic boom metric variability. Table 2.5 gives the remaining inputs from LR along with their associated coefficient. Similar to CarpetDIEM (Table 2.4), LR identifies aircraft trajectory, meteorological inputs, and contaminating noise as contributing to ΔPM variability. Dive Slope is given the largest coefficient of the aircraft trajectory inputs, showing that the low-boom dive maneuver's execution had an effect on the ΔPM values. Also, several meteorological factors from the balloon taken at high altitudes are identified. The North/South Wind Direction at high altitudes is given the largest coefficient of any input factor. Lastly, Ambient PL is given a negative coefficient, similar to Table 2.4, showing that contaminating noise causes more negative ΔPM values.

Table 2.5. QSF18 ΔPM remaining inputs after LR with their associated coefficient.

Input Name	Coefficient
High Altitude Wind Direction (N/S)	2.0
Dive Slope	1.5
Ambient PL	-1.5
High Altitude Temperature	-1.2
Aircraft Heading	1.0
Aircraft Tail #	0.5
Wind Speed	0.1
Humidity	0.08
High Altitude Wind Direction (E/W)	-0.01
RMSE	**5.8 dB**

2.2.7 Conclusions

In this section, LR has identified key factors driving measured metric variability. It is found that metrics are surprisingly sensitive to aircraft trajectory at both CarpetDIEM and QSF18. For QSF18, which utilized the low-boom dive maneuver, aircraft trajectory is expected to contribute. However, at CarpetDIEM, which aimed for nominally cruise booms, LR also identifies aircraft trajectory inputs as contributors to measured metric variability. Further analysis of the aircraft trajectory, based on the LR findings, has shown that some booms measured during CarpetDIEM were not generated during steady, level flight.

Additionally, contaminating noise was identified through LR as an important factor in measured metric variability, especially at QSF18. Because the contaminating noise at QSF18 was seen to strongly affect the metrics, a filter was used to remove the contaminating noise. After this filter, LR identified other inputs that contribute to the variability at QSF18, although the RMSE post-filter went up by several decibels. This analysis shows that contaminating noise is a problem in low-boom, high noise environments, but that ambient filters remove correlation of contaminating noise with boom metrics.

These results also help establish an expected prediction RMSE range of 4-8 dB depending on the flight test logistics and environment. Using all available weather, trajectory, and ambient information, LR for CarpetDIEM was able to predict metrics with an RMSE of 4.5 dB. At QSF18, the RMSE was 4.1 dB before filtering, and 7.4 dB after filtering. Thus, the predictions for the X-59 test flights are expected to fall within a similar range.

In addition to measured metrics, this section's preliminary results for predicting ΔPM suggest areas for PCBoom improvement. A wide variety of input factors at both CarpetDIEM and at QSF18 suggest that aircraft trajectory, meteorology, and contaminating noise all play a role in ΔPM variability. One preliminary takeaway is that the meteorological data at all altitudes is important. This warrants expansion of the LR inputs to potentially include more meteorological data at more altitudes, rather than just a low and high altitude. Aircraft trajectory, even for simple flight paths, was also seen to influence ΔPM values. This could suggest improvement of PCBoom ray-tracing implementation. These results, however, are preliminary and further investigation will be a part of future work. Creating and improving the inputs, rerunning PCBoom with turbulence filters, and cross-checking with other model selection methods will improve and clarify these results.

It is also important to note that many of the inputs used in this analysis are highly correlated. For example, Ambient PL and Ambient DSEL are correlated, and thus LR could likely use either one with minimal change in prediction accuracy.

Overall, this section's results provide guidance for X-59 testing by identifying sources of metric variability and discrepancies between measured and predicted metrics. These results do not suggest using LR as a prediction tool to plan test flights, but they do show that LR is a useful framework for analyzing boom data to gain important insights. This same framework, which is relatively simple and easy to implement, can be used at future X-59 test flights with greater amounts of data to guide NASA and partners in understanding the measured and predicted metrics. A practical application in the event that planned noise doses are not matching measured noise doses during X-59 community tests is to fit a LR model to make empirical corrections to PCBoom predictions as part of the preflight planning process.

Section 3 – Other Investigations

3.1 Signal Processing Methods

(Much of this section is identical to portions of Anderson *et al.* (2024a))

3.1.1 Time-domain Windowing

One of the many factors to consider when analyzing sonic boom recordings is time-domain windowing prior to performing a fast Fourier transform (FFT)-based spectral analysis. Windowing ensures that the waveform endpoints are set to zero, thereby reducing spectral leakage due to discontinuities at the waveform end points. One useful window choice is a Tukey (or tapered cosine) window because it leaves most of the waveform unaffected. The ramp portions of this window are defined by cosine functions, and the length of the ramp portions is defined by the "cosine fraction." This is illustrated in Figure 3.1. As an example, a cosine fraction of 0.4 indicates that each ramp individually covers 20% of the waveform, for a total of 40% of the waveform being tapered. Thus, the percentage of the waveform tapered by each individual ramp is determined by dividing the cosine fraction by two and multiplying by one hundred. In the limit that the cosine fraction becomes zero, the Tukey window becomes a rectangular window. In the limit that the cosine fraction becomes unity, the Tukey window becomes a Hann window. A cosine fraction of 0.1 is recommended for sonic boom analyses where waveforms start 100 ms before the peak of the primary shock and the total recording length is 650 ms, as shown in Figure 3.2(a) and (c). This recording length convention is the same as used in Page *et al*. (2014), though the lead time of 100 ms recommended here is shorter than in Page *et al*. (2014). This captures more of the post-boom noise if that is of interest to a particular analysis.

The choice of cosine fraction is relatively unimportant as long as the window is not too rectangular, and the ramps do not attenuate the main shocks. The effects of different cosine fractions on sonic boom metrics can be studied directly, as is shown in Figure 3.2. In this example, sonic boom metrics are calculated with varying cosine fractions. Figure 3.2(a) shows an example 650-ms boom recording from the NASA Carpet Determination in Entirety Measurements I (CarpetDIEM I) test campaign (Durrant *et al*., 2022) along with a reference Tukey window using a cosine fraction of 0.1. Figure 3.2(b) shows the results of applying different cosine fractions and displays the results for each metric relative to a cosine fraction of 0.1, i.e., metric computed with a given cosine fraction minus metric computed with a 0.1 cosine fraction. This was done to visualize differences more easily for each metric simultaneously. The same analysis is shown for another boom, from the NASA Quiet Supersonic Flights 2018 (QSF18) test campaign (Page *et al*., 2020; Anderson *et al*., 2022a), in Figure 3.2(c) and (d). The two examples are included to demonstrate that the results are similar for booms that have different relative amounts of post-boom noise. For both waveforms, the metric values all have a region of relative flatness between a cosine fraction of about 0.05 to 0.3. Divergences from this flat region at small cosine fractions are likely due to the window being too rectangular and causing waveform edge discontinuity, especially for the boom in Figure 3.2(c), which has notable post-boom noise and has a lower metric value, making it more sensitive to the discontinuity. This is because a nearly rectangular window will introduce broadband noise into the spectrum, increasing the metric value. Notice how for both booms, the metrics all diverge simultaneously at and above a cosine fraction of 0.3. For this particular cosine fraction, the individual ramp lengths are $0.3/2 \times 650$ ms = 97.5 ms, which means that the initial ramp will start reducing the primary shock amplitude. For waveforms with 100 ms of lead time before the peak of the primary shock and a total duration of 650 ms, a cosine fraction of 0.1 seems to be a suitable choice.

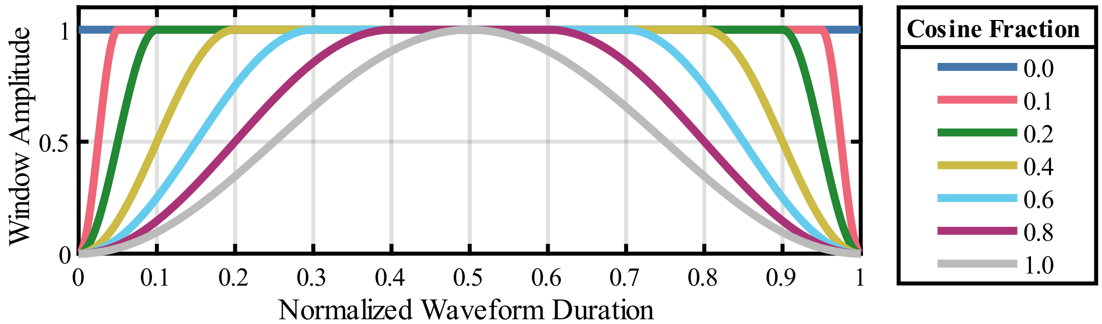

Figure 3.1. Several example Tukey windows, each with a different cosine fraction. A rectangular window is produced when the cosine fraction is zero, and a Hann window is produced by setting the cosine fraction to unity.

An asymmetric window may also be desirable, where the second ramp is longer than the first (Klos, 2022). This would enable an even more gradual taper to zero for the post-boom noise. This window type is analyzed in Figure 3.3. Part (a) shows the same boom as analyzed in Figure 3.2(c) and (d), but with an example asymmetric window superposed on top of the waveform. Part (b) shows the same type of analysis as Figure 3.2, but where the first ramp is kept at a cosine fraction of 0.1 (covering 5% of the recording) and only the second ramp cosine fraction is varied between 0–0.5 (0–25% of the recording). Evidently, increasing the second ramp length has marginal effects on the metric values, so long as its cosine fraction is greater than about 0.05 (2.5% of the recording). Therefore, an asymmetric window is also a good choice when analyzing sonic booms, though for this example it is not necessarily better than a symmetric window.

There likely exist other acceptable windows that could be successfully applied to sonic boom waveforms. Overall, the choice of window appears to be relatively unimportant so long as the primary boom is not affected by the windowing. In other words, the post-boom noise is a small contribution to the metric values, and a cosine fraction of 0.5 (25% of the recording) for the latter half of the waveform only has a 0.25 dB impact. This also implies that the window gain is negligible compared to the primary boom signal, which is not affected by the window. Further research could be performed to determine whether the claims in this section hold true for recordings with lower signal-to-noise ratios.

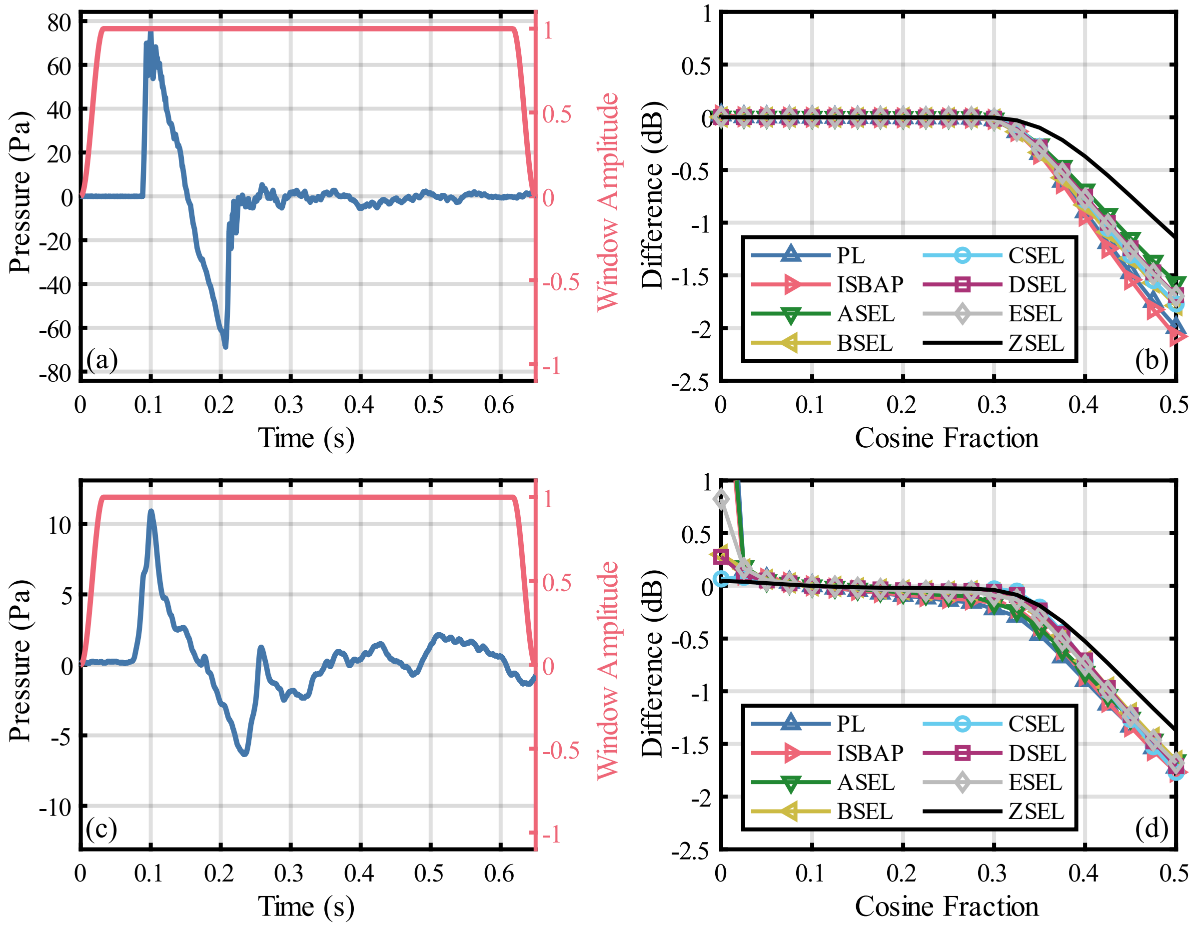

Figure 3.2. The effects of different cosine fractions on sonic boom perception metric values. (a) An example waveform from CarpetDIEM I along with a reference Tukey window with a cosine fraction of 0.1. (b) All sonic boom metrics shown relative to their calculated values with a cosine fraction of 0.1. (c) Similar to (a) but using a boom from QSF18 with notable post-boom noise. (d) Similar to (b) but using the QSF18 boom.

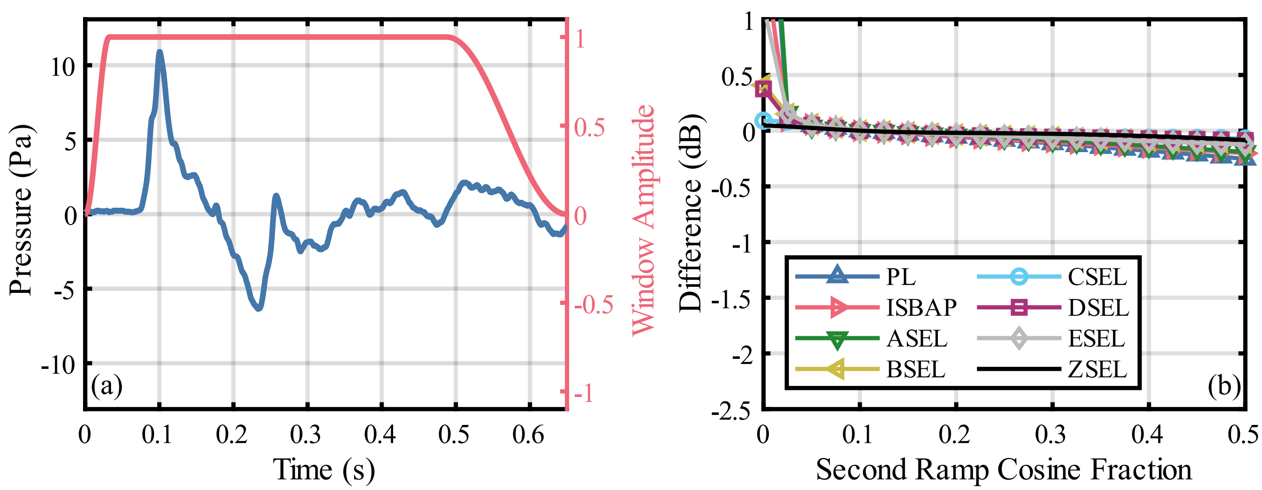

Figure 3.3. Analyzing an asymmetric window on the same boom as analyzed in Figure 3.2(c) and (d). (a) The boom is shown with an example window. The first ramp has a cosine fraction of 0.1 and the second ramp has a cosine fraction of 0.5, meaning it covers 25% of the recording. (b) The second ramp taper ratio is varied and

the effects on the metrics are shown relative to the case where the taper ratio for the second ramp is equal to 0.1.

3.1.2 Zero Padding

When performing an FFT analysis over a short time interval, the frequency resolution is sparser than for a longer time interval. When converting the spectrum into one-third octave (OTO) bands, this sparse frequency resolution results in not every OTO band having an FFT bin, creating a nonphysical distribution of energy in adjacent OTO bands at low frequencies. An example is the spectrum shown in Figure 3.4(a). Notice the jagged peaks and troughs in the spectrum below 10 Hz. A solution to this issue is to use a longer recording to increase the frequency resolution so that each OTO band contains at least one FFT bin. This can be accomplished through zero padding. After windowing the signal, zeros are artificially appended (and/or prepended) onto the waveform, creating a longer recording. Because the sonic boom is a one-time impulse event, and many sonic boom metrics are exposure metrics, adding zeros to the signal does not affect those final metric values.

To determine the total duration of the padding required to remove the jagged peaks in the low-frequency spectrum, spectra of waveforms with increasing pad lengths were computed, and the results are shown in Figure 3.4(b). This analysis demonstrates that a pad of four seconds, resulting in a padded waveform of total duration 4.650 seconds, is a good choice to smooth the spectrum down to 1 Hz. Larger padding will always produce even smoother results but is more computationally time-consuming for FFT calculations. Therefore, we recommend applying up to four seconds of zero-padding to the windowed waveform before performing an FFT, if smooth FFT results are desired. An example is shown in Figure 3.5, where the four seconds of padding is split with two seconds before and two seconds after the windowed waveform. This could also be applied as four seconds either before or after the recording.

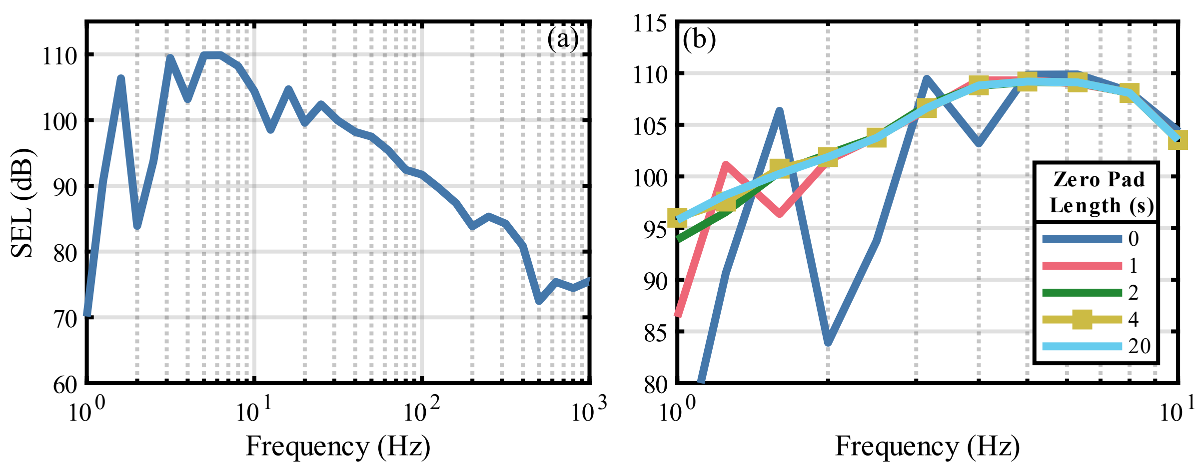

Figure 3.4. Effects of zero-padding. (a) The original OTO spectrum calculated using a 650-ms recording. Notice the jaggedness below 10 Hz. (b) Applying different pad amounts.

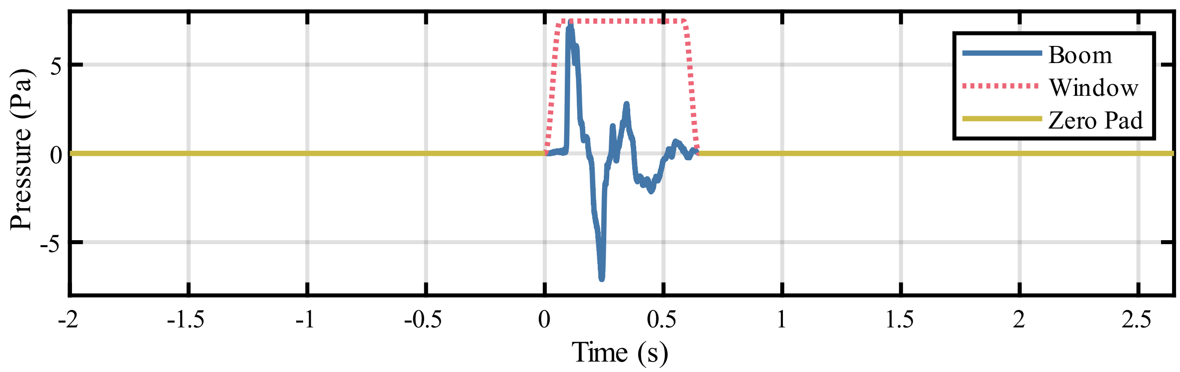

Figure 3.5. An example waveform with the recommended four seconds of zero padding applied to the recording. The pad is applied after windowing, the window height has been scaled to match the waveform amplitude, and the cosine fraction of the window has been increased to 0.2 for easier viewing.

To further analyze why 4 seconds of padding is a suitable amount, Figure 3.6 shows the narrowband spectra for four of the pad lengths used in Figure 3.4 with the OTO band lower and upper frequencies (-3 dB) indicated with dashed lines. Note that pad lengths of 0 and 1 second(s) result in frequency resolutions that do not have a narrowband frequency bin in each OTO band down to 1 Hz. This causes the low-frequency oscillations for these two pad lengths in Figure 3.4. A pad length of 2 seconds does place a data point in each band above 1 Hz, but not in the 1 Hz OTO band. Lastly, a pad length of 4 seconds results in at least one data point within each band of interest down to 1 Hz. Therefore, the final recording length must yield a frequency resolution that places at least one data point within every OTO band down to and including the lowest frequency band of interest.

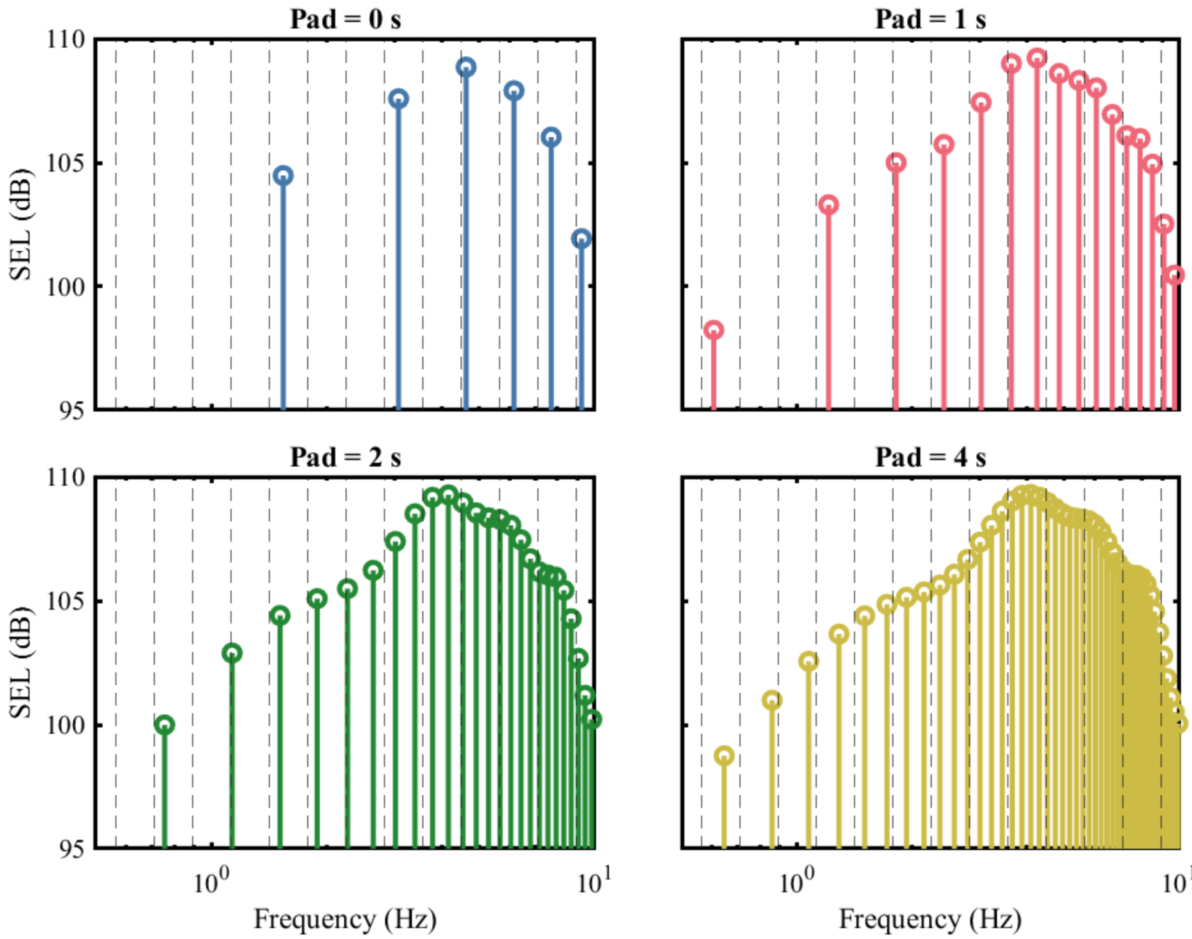

Figure 3.6. The narrowband spectra shown for four different total pad lengths. The colors correspond to those shown in Figure 3.4. Dashed lines represent the lower and upper frequencies of each OTO band.

3.2 Weather-robust Microphone Configurations for the GRS Systems

3.2.1 Lab Testing

Because of prior development (James *et al.*, 2020) and testing (Gee *et al.*, 2020) of weather-hardened microphone systems, and their use in sonic boom measurements (Downs *et al.*, 2022; Anderson *et al.*, 2022a; Durrant *et al.*, 2021b) and numerous rocket launches (Gee *et al.*, 2023; Cunningham *et al.*, 2023; Durrant *et al.*, 2023; Hart *et al.*, 2021), BYU has been part of extended discussions regarding microphone systems for X-59 community noise measurements. During the latter part of this R&D program, a smaller version of the ground-based weather-robust microphone configurations nicknamed COUGAR and COUGARxt at BYU was developed. The “COUGAR-cub” is a more compact microphone configuration that is being studied because of the desire to have a smaller windscreen system for the NASA GRS units. A comparison photo of all three configurations can be seen in Figure 3.7. Of note, in addition to being wider than the other configurations, the COUGARxt also has a thicker screen (3” vs 1.5” for the other configurations). It is also worth noting that the COUGAR-cub configuration does not have bird spikes, though those can be added in the future. Details on the measurements for each configuration can be seen in Figure 3.8.

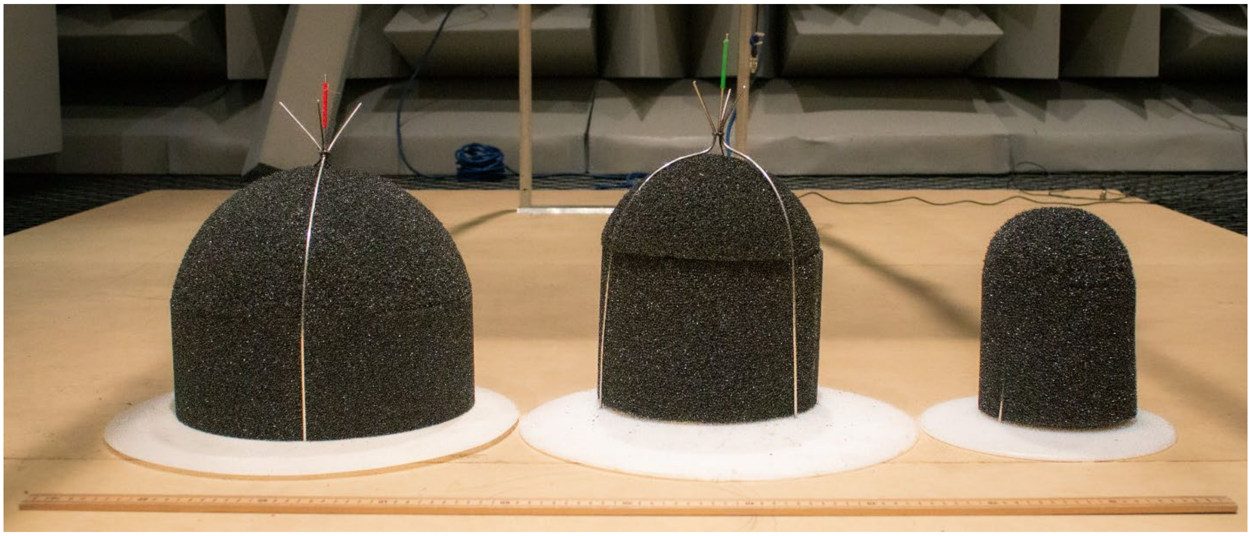

Figure 3.7. Comparison photo of (left to right) COUGARxt, COUGAR, and COUGAR-cub configurations.

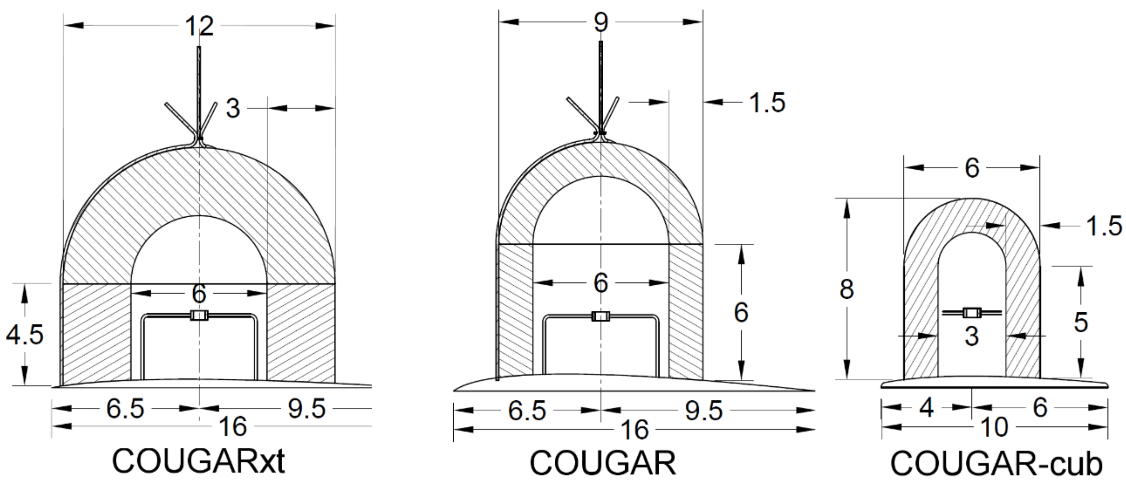

Figure 3.8. Cross-sections for (left to right) the COUGARxt, COUGAR, and COUGAR-cub. Units given in inches.

The COUGAR-cub was tested using existing measurement hardware and approaches alongside BYU's already-tested COUGAR and COUGARxt configurations to compare performance (Gee *et al.*, 2020, Anderson, 2021, Anderson *et al.*, 2022a). Some testing was repeated on the prior systems. The tests were performed inside of BYU's fully anechoic chamber using the Angular Recording Configuration (ARC). The ARC (pictured below) has a speaker mounted in it and allows for the movement of the speaker by increments of five degrees within a range of 5-90° about the origin. For testing, the different microphone configurations were located at the origin. Alongside the microphone configuration was a reference microphone (made visible by the blue tape in the photo); this enabled a reference of the speaker output and measurements were adjusted using these reference measurements (see Appendix D.5 for validation of this method).

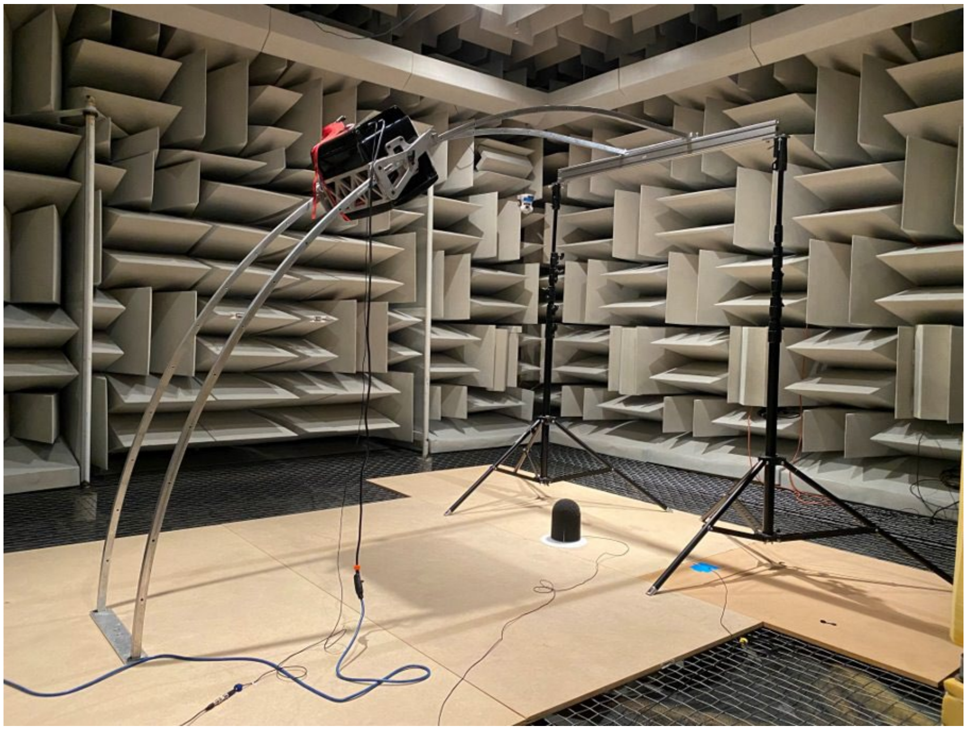

Figure 3.9. The ARC being used to test the COUGAR-cub in BYU's fully anechoic chamber. The interior dimensions of the chamber are 8.8 x 5.8 x 5.8 m (29 x 19.0 x 19.0 ft). The chamber is rated from 80 Hz to 20 kHz.

Several different tests were conducted on the different configurations, including elevation angle and azimuthal angle tests. The elevation angle is defined with 5° being grazing incidence (speaker near the ground) and 90° being normal incidence (speaker directly above the test article). A "baseline" measurement was made using a quarter-inch pressure-field microphone placed horizontally on the medium-density fiberboards at the same location that the COUGAR-cub and other test articles would be placed. The purpose of this baseline measurement is to enable comparisons against a more ideal measurement. Further details on these types of measurements can be found in Gee *et al.* (2020), Anderson (2021), and Anderson *et al.* (2022a).

3.2.1.1 Comparison with Prior Measurements

An important analysis is to verify that the results are similar to previous measurements. As a control measurement, the arc sweep involving the COUGAR in its standard orientation is used. The three measurement sets that can be used to verify repeatability occurred in Fall 2019, Summer 2020, and Spring 2023, and results are shown in Figure 3.10 relative to each measurement's respective baseline. Only four angles are shown for simplicity. Although not perfect matches, the spectra line up well and show several common trends. This indicates that these measurements can reliably provide insight into the overall response of the microphone configuration, within 0.5 dB up to 2 kHz and 1 dB at high frequencies.

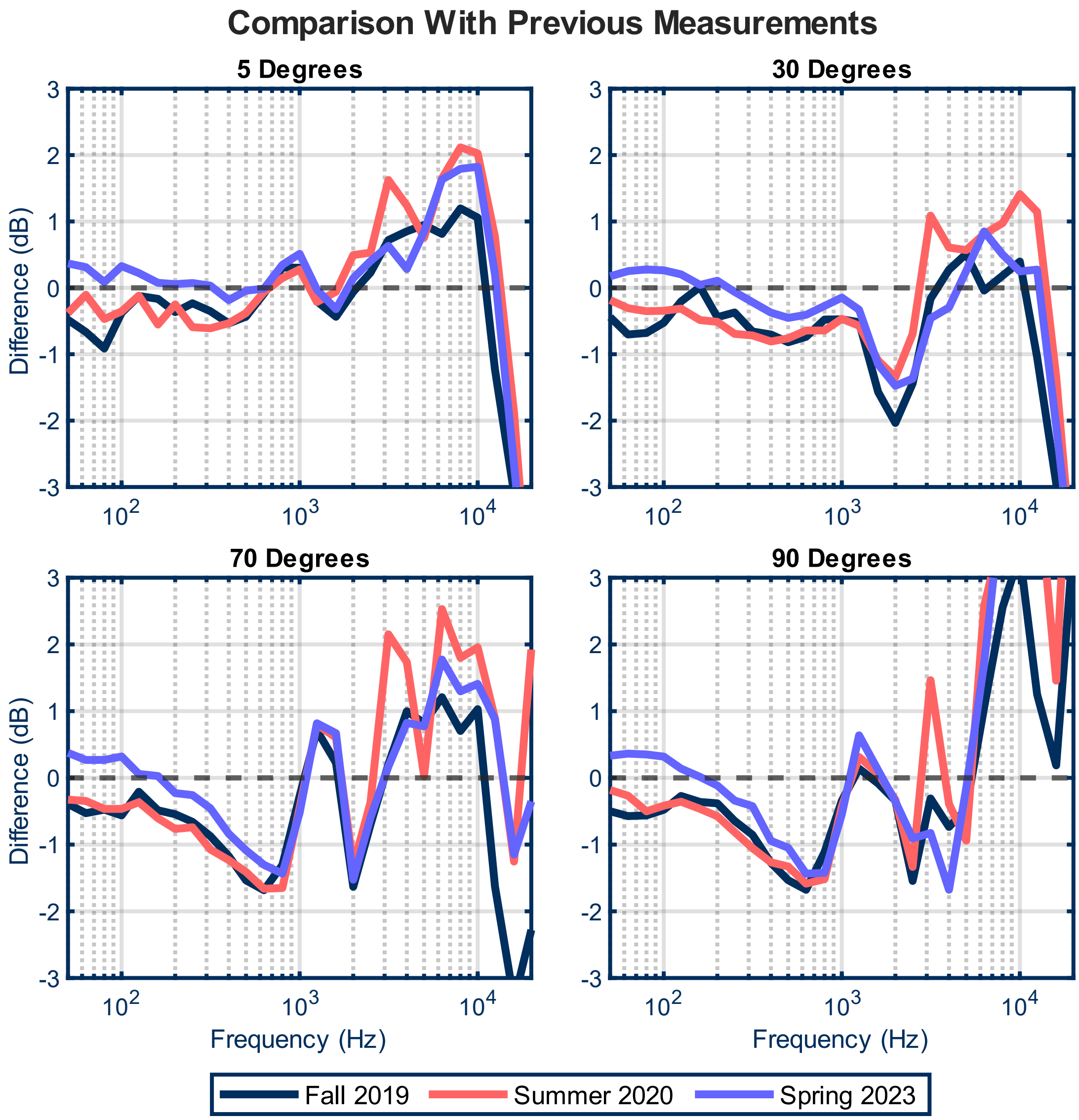

Figure 3.10. Comparison with prior results at four different elevation angles. The COUGAR configuration was compared to the baseline measurement and the difference is shown on the y-axes. Each COUGAR measurement was compared to the baseline measurement from its respective measurement campaign.

3.2.1.2 Determining a Suitable Recording Length

The question was brought up as to whether the recording length of 30 seconds was sufficiently long to average random errors due to inconsistent speaker output. To determine whether a 30-second recording was long enough, a COUGAR configuration was measured at an elevation angle of 10° for 60 seconds. The recording length effects could then be analyzed by choosing varying amounts of time within the recording to create results. This is shown in Figure 3.11, where all recording lengths produce nearly identical results. This indicates that not only is 30 seconds long enough, but it is more than enough to average out random errors.

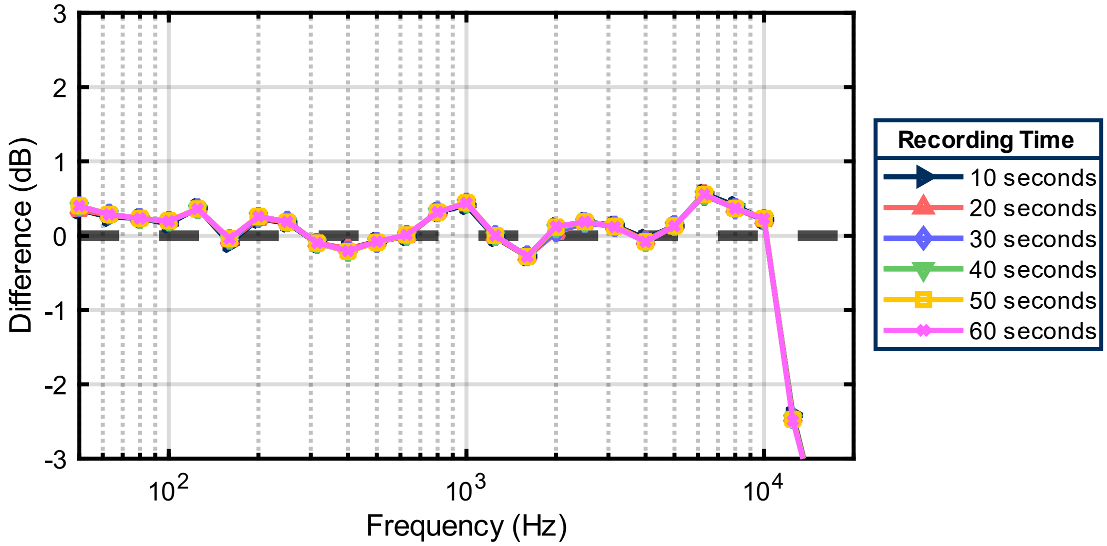

Figure 3.11. Determining whether 30 seconds is long enough to sufficiently reduce random errors. A 60-second recording was performed at an elevation angle of 10°. During the analysis, the recording was trimmed to different lengths. According to these results, 30 seconds is more than enough to average out the random errors. The difference on the y-axis is measured relative to the baseline measurement.

The effects due to the three different plate designs are shown in Figure 3.12. For this analysis, the microphone was placed inverted above the plate without a windscreen, and results are shown relative to the baseline measurement. Overall, all three ground plates produce similar results, and many of the differences seem to be explainable on physical grounds. For example, multiple trends are ordered based on either plate thickness or diameter. Overall, the COUGARxt plate, with its 16” diameter and thinner profile, yields the smoothest response with frequency, whereas the COUGAR-cub plate tends to have the most pronounced peaks. Additionally, several peaks and nulls in these spectra occur at the same frequency for the COUGAR and COUGARxt, with the COUGAR-cub having corresponding nulls at slightly higher frequencies. These peaks are likely related to plate diameter.

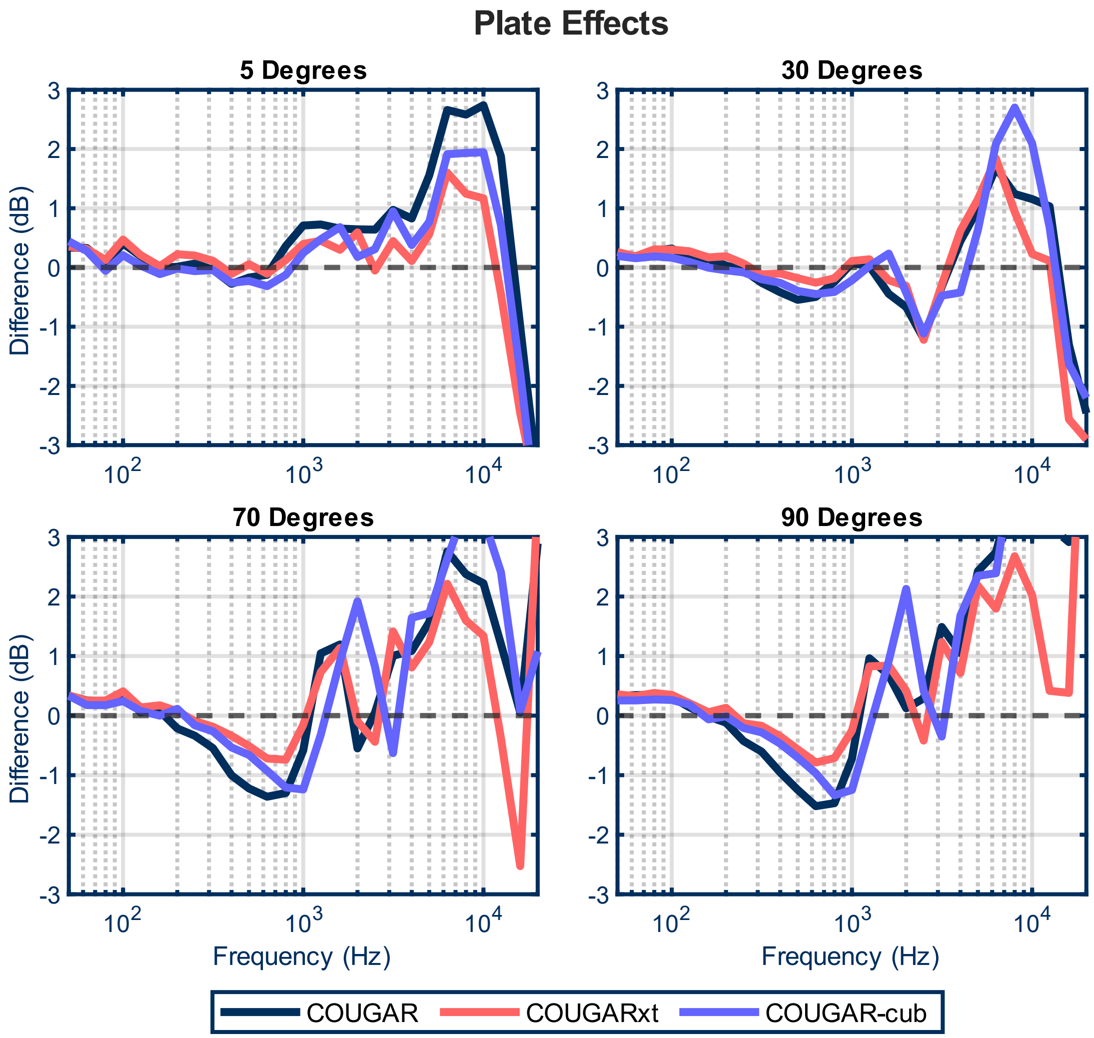

Figure 3.12. Inverted microphone above three ground plates, relative to the baseline at four different elevation angles for all three plates.

Figure 3.13 shows the case where the windscreen has been included, shown relative to the ground-plate-only results. The resulting plots are equal to the negative of the windscreen insertion losses. Again, there are physically-important trends in these results. Notice that the thicker COUGARxt windscreen has greater high-frequency insertion loss than the other two. At low elevation angles, the COUGAR and COUGAR-cub windscreen have similar insertion losses, a likely consequence of their equal thicknesses. At higher elevation angles (beginning with 75°), there appear to be windscreen cavity resonances that are related to the overall diameter of the windscreen. Notice that for a 90° elevation angle, the COUGARxt has the lowest-frequency null, followed by COUGAR, and then by COUGAR-cub. Also note that for these measurements, the bird spikes were omitted from the COUGARxt due to a lack of proper fitting in the lab. The differences are negligible; more information on the acoustic effects due to bird spikes can be found in Appendix D.

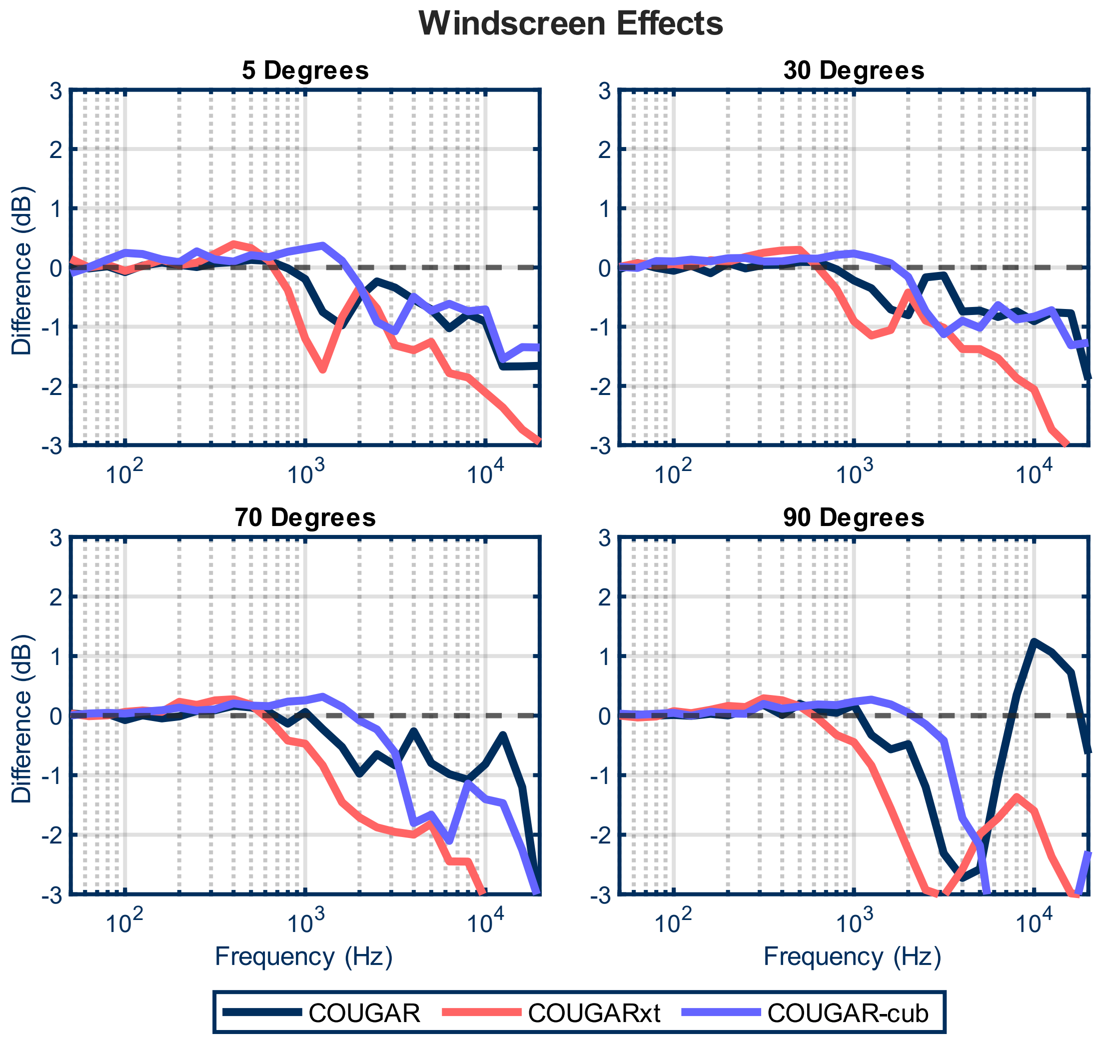

Figure 3.13. The effects of including the windscreen, shown relative to the case without the windscreen for four different elevation angles for all three plates. These plots are equivalent to the negative of the windscreen insertion loss.

The combined effects of the plates and windscreens create a unique acoustic response for each configuration. These total responses are shown in Figure 3.14 for all three configurations. While the plate effects tended to bias the signal positively at high frequencies, the negative bias from the windscreen attenuation at high frequencies tends to bring the spectra back down toward zero. Although these results appear noisier than the isolated plate and windscreen effects, many of the same artifacts are visible in Figure 3.14 as in the plate and windscreen results.

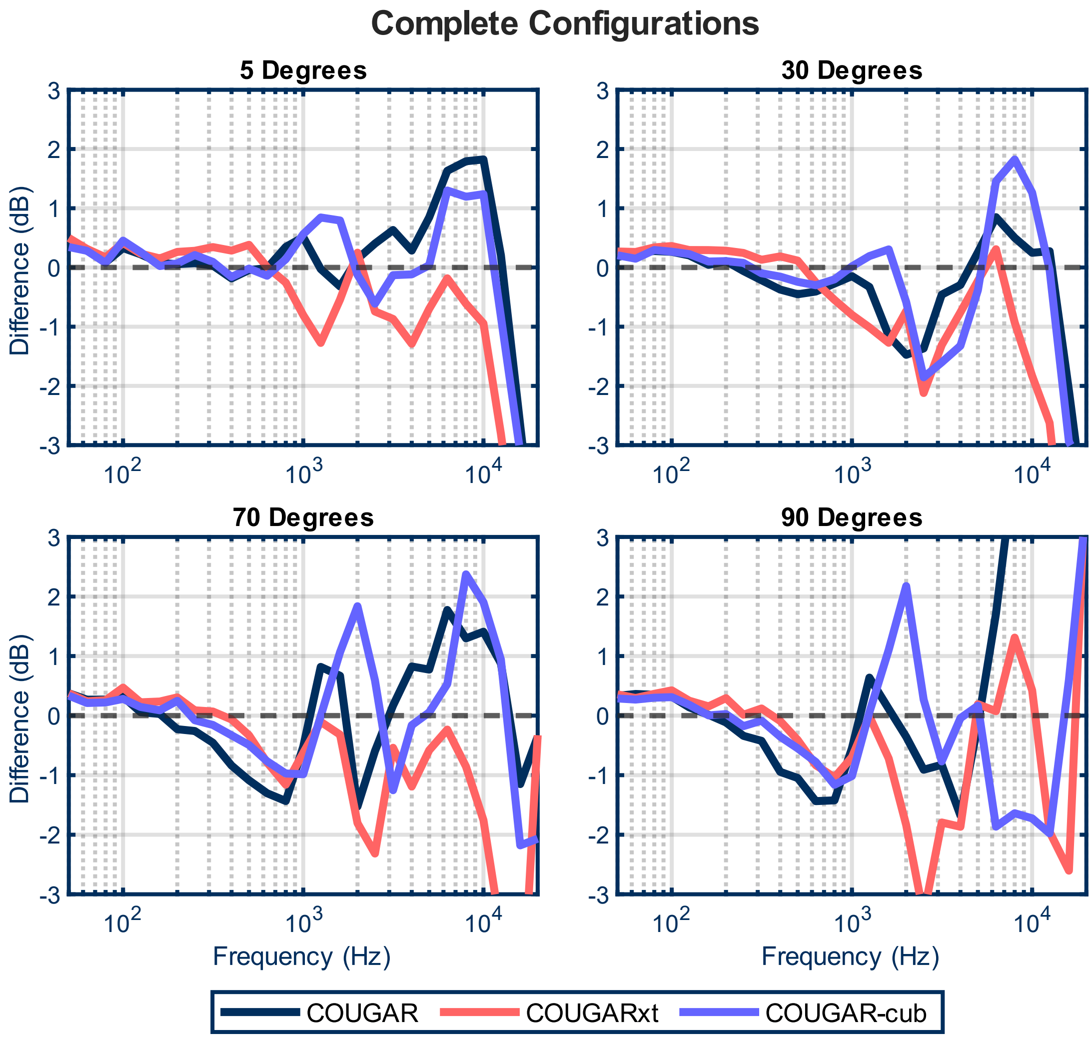

Figure 3.14. The complete configurations, shown relative to the baseline. Effects due to both the plates and the windscreens are visible in these results.

3.2.1.3 Azimuthal Variability

The azimuthal angle variability for the COUGAR and COUGARxt were tested in the past (Gee *et al.*, 2020; Anderson, 2021; Anderson *et al.*, 2022a) and then compared to the testing that was done on the COUGAR-cub this year (2023). The COUGAR-cub was only tested on the angles of 90° and 180°. This is because the previous testing done on the COUGAR and COUGARxt show that it was unnecessary to test more azimuthal angles, as the variability was insignificant.

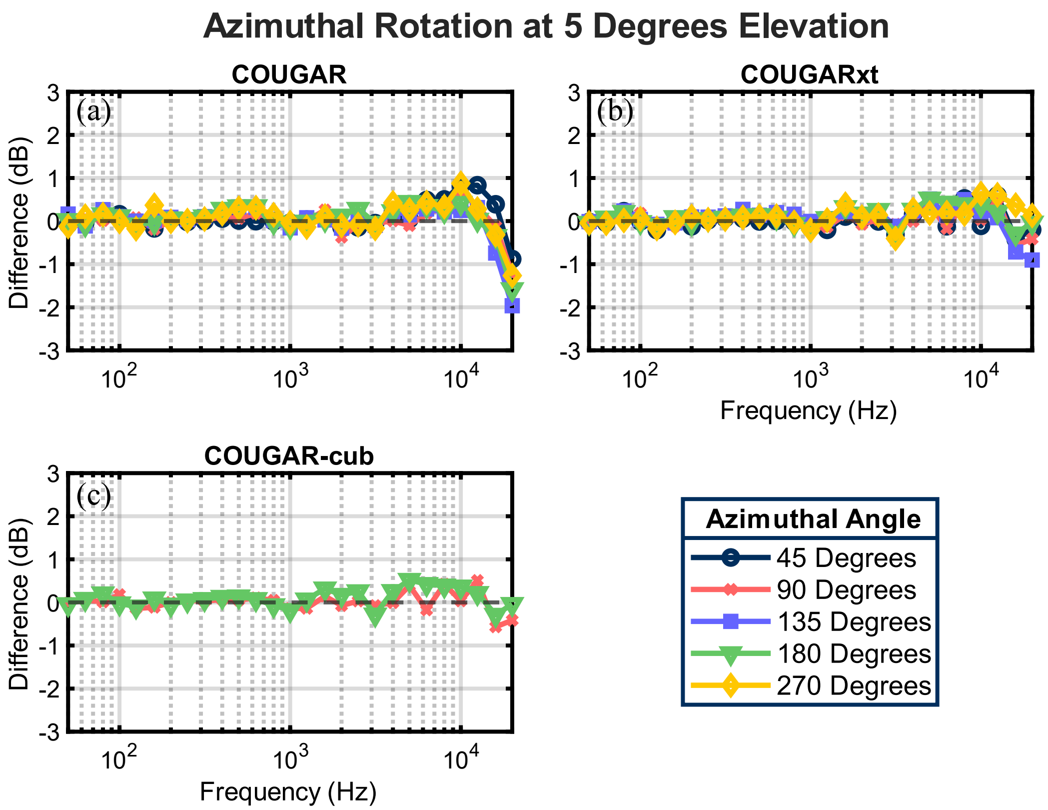

Figure 3.15. Dependence of (a) COUGAR, (b) COUGARxt, and (c) COUGAR-cub on azimuthal angle, relative to 0°, for 5° elevation. The COUGAR-cub was only tested on the orientations of 90 and 180°.

In Figure 3.15 there is little difference from the standard orientation (0°) at each different azimuthal orientation. At each of the five different azimuthal angle positions the COUGAR and COUGARxt both showed their own trends of difference from the original orientation. In Figure 3.15(a) the COUGAR starts moving towards -2 dB above 10 kHz; the COUGARxt displays a similar dip at the same frequency in Figure 3.15(b), but only reaching a difference of about -1 dB. These trends were repeated regardless of azimuthal position; likewise was the result for the two different azimuthal positions of the COUGAR-cub.

At 45° and 90° elevation, shown in Figure 3.16 and Figure 3.17, respectively, differences remain small regardless of azimuthal orientation. At 45°, differences remain within ±1 dB across frequency. At 90°, the COUGAR-cub and COUGARxt have azimuthally symmetric responses at all orientations, whereas COUGAR has some high-frequency dependence on azimuthal angle. Given the differences in plate diameter between COUGARxt and COUGAR-cub, the dominant effect (though minor) in determining azimuthal variation appears to be the maximum plate thickness. Overall, however, azimuthal angle has relatively little effect on the fidelity of the COUGAR family. While there may be some variation from the original orientation, these variations tend to remain within the range of ±1 dB. Nonetheless, future iterations of COUGAR may use the thickness of the COUGARxt and the COUGAR-cub plates.

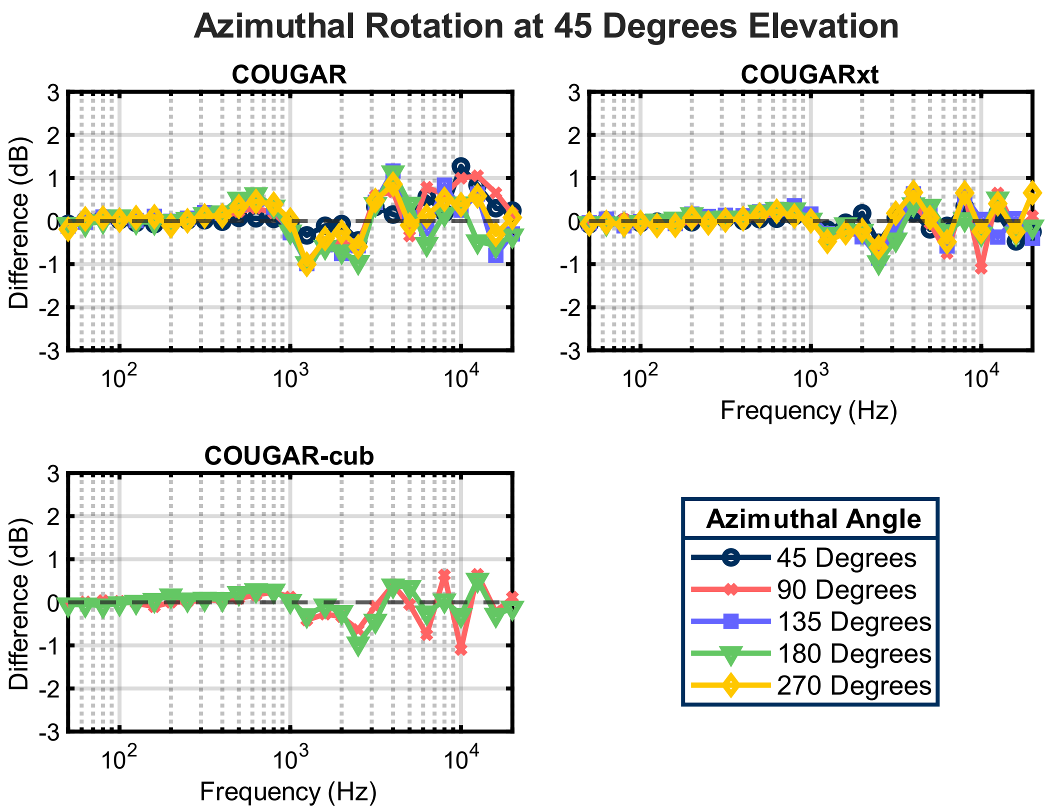

Figure 3.16. Same as Figure 3.15, but for 45° elevation.

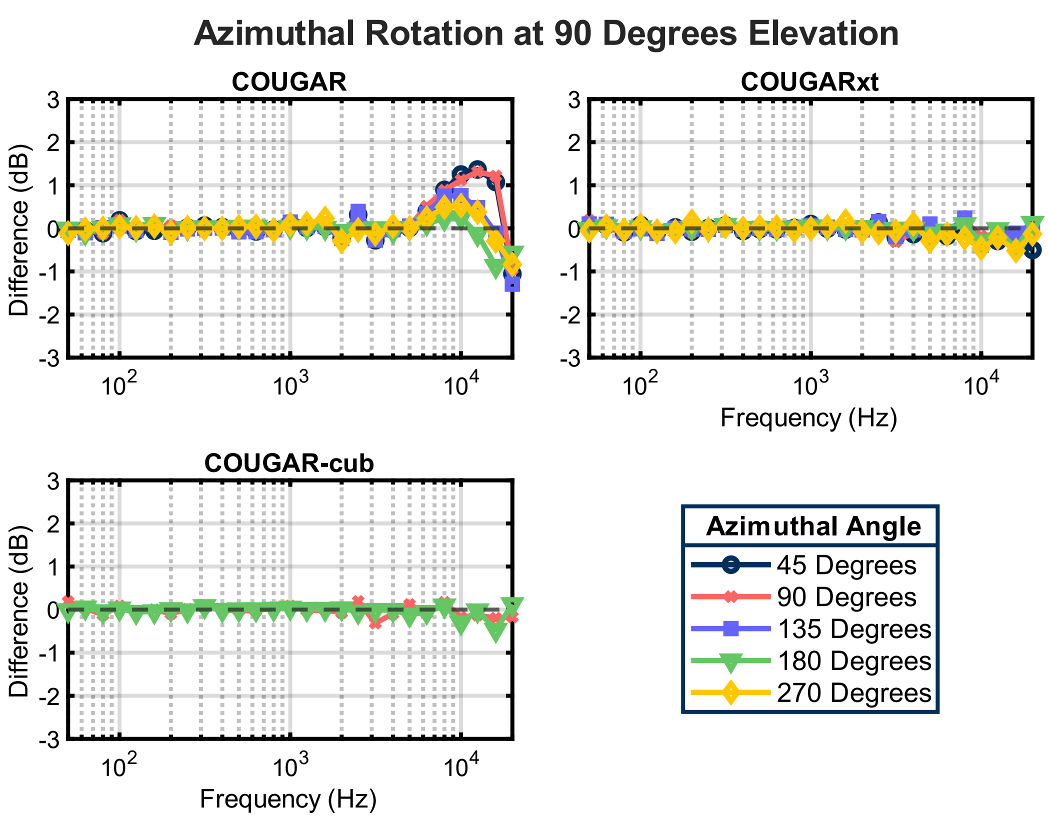

Figure 3.17. Same as Figure 3.15, but for 90° elevation.

3.2.2 Outdoor Testing

Similar to Anderson *et al.* (2022a), outdoor testing was performed to determine the wind noise rejection of each microphone configuration, now including the COUGAR-cub configuration. The setup is shown in Figure 3.18. Each microphone configuration used an NI 9250 data acquisition card. The COUGARxt, COUGAR-cub, and COUGAR used a GRAS 47AC microphone, which has previously been used in COUGAR and COUGARxt wind noise testing. A shorter version of the COUGAR-cub was also tested in Figure 3.18, but because it cannot accommodate a standard 1/2" microphone, it is not discussed further in this report except briefly in Appendix D.

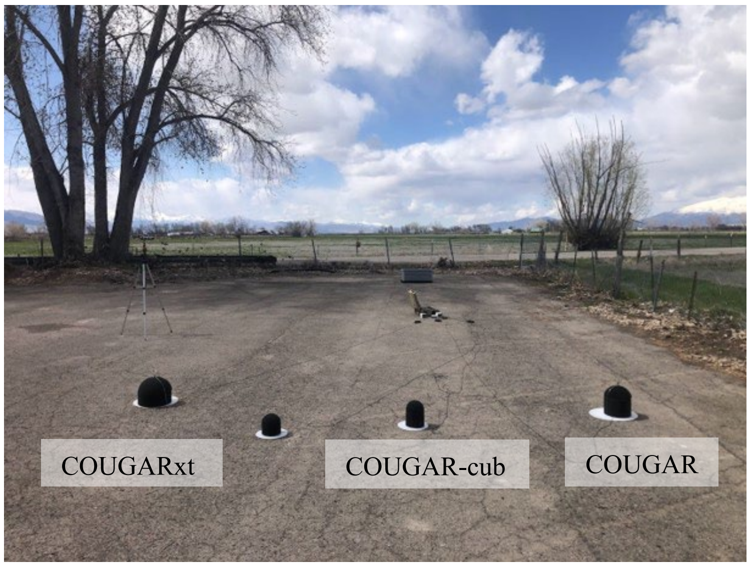

Figure 3.18. Setup for wind noise field testing. The direction of the wind was towards the camera.

Figure 3.19. Kestrel® 4500 Bluetooth weather meter set up on a tripod at the measurement site.

Additionally, a Kestrel® 4500 Bluetooth weather meter, shown in Figure 3.19, was set up to measure wind speeds, with a 1-second resolution in time. The wind speed reached up to 10 m/s during the 1.5-hour recording, though the speed typically stayed around 5 m/s. A summary of recorded wind speeds can be seen in Figure 3.20.

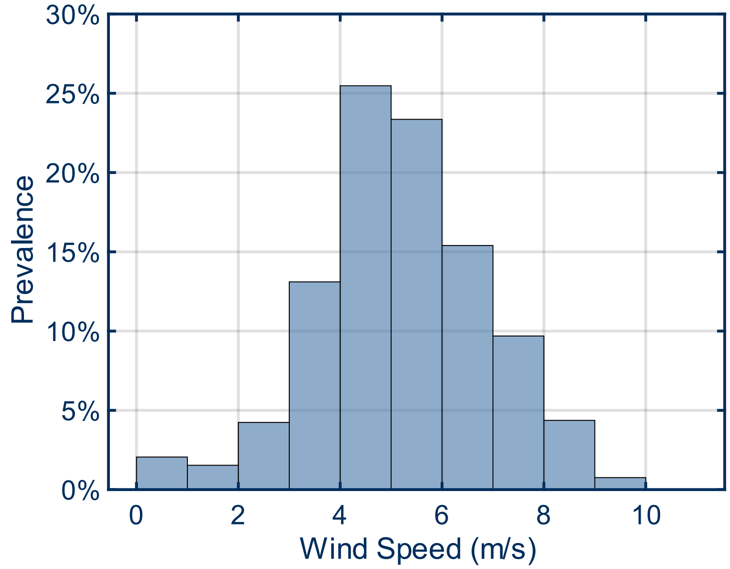

Figure 3.20. Histogram of recorded wind speeds in m/s.

One purpose of the outdoor testing was to determine if the thickness or diameter of the windscreen had a larger impact on wind noise rejection. The 3” windscreen for COUGARxt is twice as thick as the windscreens for COUGAR and COUGAR-cub (1.5”), and the outer diameter of each configuration is different with COUGARxt being the largest (12”) and COUGAR-cub (6”) being the smallest. The results of the wind noise testing for these three configurations are shown below in Figure 3.21. At low frequencies, dominated by wind pseudonoise, the spectrum of each microphone configuration behaves similarly. Wind pseudonoise is pressure perturbations measured by the microphone that are not from an acoustic source, but rather from the wind. Above 80 Hz, all three spectra converge once again. It is the 2-80 Hz region that is most interesting.

The pressure measured by a microphone at the center of a windscreen is a combination of the acoustic pressure and the turbulent pressure fluctuations as mitigated by the windscreen. Within the turbulence inertial subrange, pressure fluctuations vary linearly with the fractional-octave band, which produces a characteristic spectral slope indicative of wind noise. However, above a windscreen and windspeed-dependent crossover frequency, the turbulent pressure fluctuations are incoherent over the surface of the windscreen, and the characteristic spectral slope is −26.7 dB per decade (van den Berg, 2006. See also Cook *et al.*, 2021a, 2021b; Jones *et al.* 2020). At the frequencies where there is greatest separation between the three spectra (about 4 – 20 Hz) in Figure 3.21, the three spectra share this rolloff. Below that, they seem to have different crossover frequencies and slopes that differ from simple expected windscreen behavior. But, in the absence of ambient acoustic noise, it would be expected that each of the windscreens would maintain its −26.7 dB per decade rolloff until the dissipation subrange is reached where the rolloff becomes even steeper. This suggests that above 4 Hz, COUGARxt outperforms COUGAR by about 4 dB and COUGAR-cub by about 8 dB. Given that COUGAR and COUGAR-cub have the same thickness, it also suggests that outer diameter plays a critical role in wind noise rejection.

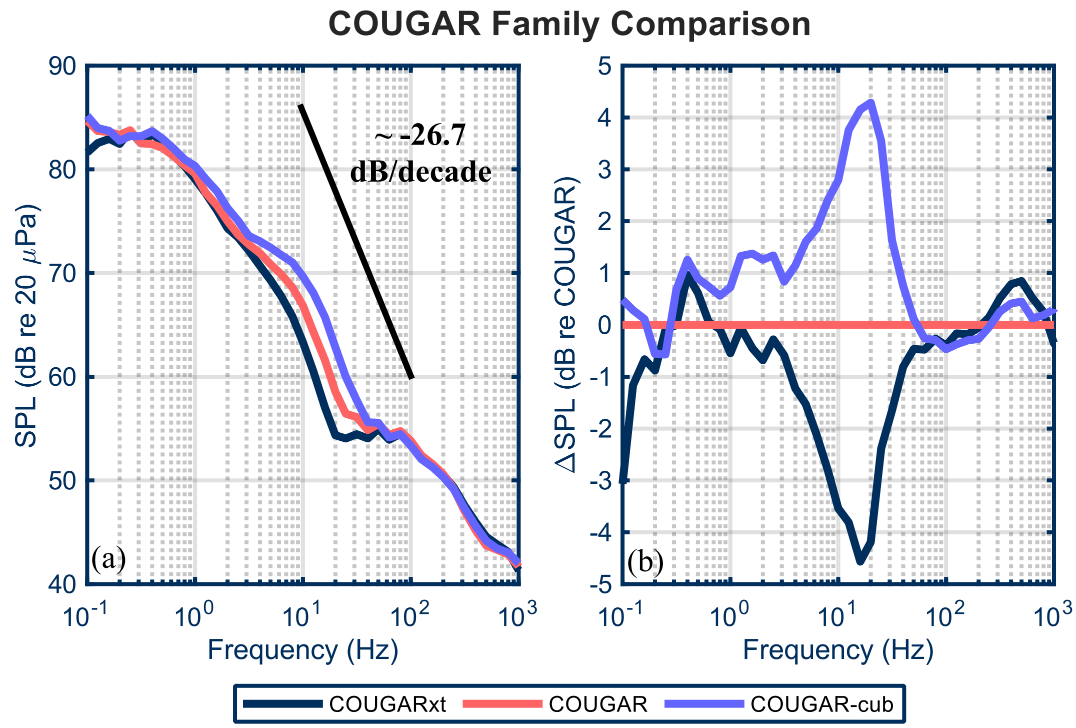

Figure 3.21. Wind noise field testing results. (a) Spectra of COUGARxt, COUGAR, and COUGAR-cub. An approximate -26.7 dB/decade line is shown. (b) Comparative spectra of the same microphone configurations.

Section 4 – Conclusion

4.1 Summary and Recommendations

This contractor report contains research-based recommendations from Brigham Young University regarding best practices for sonic boom measurements and analyses, especially pertaining to upcoming Quesst Mission X-59 validation and community noise testing. The following discussion is a summary of the key recommendations and results from this report.

First, contaminating noise artificially inflates metric values. This noise can be either ambient noise or electronic noise. Two filtering techniques have been developed and are recommended for use during X-59 community noise testing. The first is a sixth-order Butterworth magnitude filter with a corner frequency corresponding to the lowest frequency one-third octave band to drop below 3 dB SNR. The second filter is a frequency-domain brick wall filter, removing all spectral data above this same cutoff frequency. Both filters have been demonstrated to effectively remove contaminating noise corruption from simulated low-boom waveforms with real-world contaminating noise. In a direct comparison with work done by Klos (2022), both filters performed equally with other methods, and it is therefore recommended that the present methods as well the methods proposed by Klos (2022) all be used during X-59 testing. This recommendation is based on the fact that the different techniques are likely robust to different types of errors and can be used as a cross validation to ensure accurate metric calculations. Additionally, because the brick wall filter performs nearly identically to the Butterworth filter method, further attempts to fine-tune the high-frequency rolloff for sonic booms are unlikely to yield a large benefit for contaminating noise removal from metric calculations.

Not removing contaminating noise from metric calculations can bias other important research results. For example, contaminating noise was not removed from QSF18 recordings prior to calculating an estimated dose-response curve. Although the estimated dose used a combination of predictions and measurements, it is estimated that contaminating noise removal could shift the entire dose-response curve by several decibels, especially for the quietest booms.

Contaminating noise is also expected to be non-negligible during Quesst Phase 2 testing. Contaminating noise measurements taken during CarpetDIEM I (the same location as Phase 2 testing) has been superposed on simulated low booms, enabling metric bias calculations due to contaminating noise effects. This study indicates that higher-noise instrumentation, such as the PCB 378A07, has a noticeable impact on some metric calculations. Therefore, it is recommended to use high-sensitivity microphones and other low-noise instrumentation for X-59 low boom measurements.

Other sources of variability remain in sonic boom measurements. One effect is atmospheric boundary layer turbulence. This turbulence can cause large variations in N-wave metric values, such as those shown in this report. The resulting metrics measured across a 122 m (400-ft) linear turbulence array follow an approximately normal distribution. Some measurements were fairly consistent across the array while others exhibited large differences (> ±5 dB) across the array, resulting in large variability in the confidence interval for the mean value along the array. Due to this confidence interval uncertainty, additional research is needed to determine a suitable number of microphones for narrow confidence intervals during future low-boom aircraft certification procedures. Although simulations have indicated that low-boom metrics will vary less due to atmospheric turbulence than for N-waves, these effects need to be measured during Phase 2 testing. In addition to assessing the required number of microphones for narrow confidence intervals, this will also enable better understanding of low-boom physics, which will in turn help refine future models.

Aside from atmospheric turbulence, other factors may impact measured boom signatures on the ground. Determining which factors (such as aircraft trajectory or meteorology) are the most important for understanding measured signatures is a daunting task when considering each factor independently. Therefore, a regression technique known as Least absolute shrinkage and selection operator (Lasso) was used to determine the factors that most affected measured boom levels. After confirming that the contaminating noise mitigation techniques in this report successfully decorrelate contaminating noise from the boom metric values, Lasso Regression (LR) detected a dependence on aircraft trajectory at both QSF18 and CarpetDIEM. Although the low boom dive maneuver used at QSF18 would certainly affect the final metric values, the flights at CarpetDIEM had been expected to be nominally at cruise conditions. LR helped identify that some rays that arrived at the array originated from portions of the trajectory that were not at a steady, level cruise, which was clearly visible in the data after further analysis. This finding should be noted for the Phase 2 flights so that steady, level data is collected by extending the length of cruise portion of the trajectories compared to those flown at CarpetDIEM I. The greater altitude of the X-59 flights compared to CarpetDIEM I may also play a role in the flight path length extension. Additionally, several meteorological factors were identified by LR, but none were chosen consistently enough or given a large enough coefficient to give a general conclusion.

The LR framework also established an expected fidelity of predicted levels for X-59 flight tests if similar data are available. At CarpetDIEM, LR predicted metrics with an RMSE of 4.5 dB, while at QSF18 the RMSE was 7.4 dB. Thus, empirical models for the X-59 test flights are expected to be accurate within around 4-8 dB. Therefore, LR is a useful framework both for analyzing flight test data to determine which factors drive metric variability at each test and for preparing for future test flights. During the Quesst Phase 2 and 3 testing, increasing amounts of data can be added to the inputs and outputs, creating higher-fidelity results each time additional data are incorporated.

These same LR techniques were also used to determine what factors were the most important in determining discrepancies between PCBoom predictions and measured values, denoted as ΔPM. While preliminary, these results suggest that ΔPM is sensitive to many aircraft trajectory, meteorology, and contaminating noise factors. Notably, meteorological inputs from different altitudes were seen to drive ΔPM, suggesting that improving the LR inputs from weather balloon data may improve these results. Further investigation after applying turbulence filters in the PCBoom modeling may help identify places for PCBoom improvement or point to the need for more or better input factors into LR. Finally, a practical application of this framework could be applied to Quest Phase 3 community response tests in the case where planned noise doses are not matching measured doses over the course of the month-long tests. An LR model could be implemented to adjust the predicted dose within the preflight planning procedure.

Another topic assessed in this report is recommendations for sonic boom signal processing techniques. The first study investigated time-domain windowing effects on the final metric values. This analysis used a tapered-cosine window and found that the window length was largely irrelevant for metric calculations as long as the window did not attenuate the primary shocks. The second study determined that an OTO spectrum created from an FFT-based analysis will be smooth as long as there is at least one FFT frequency bin within each OTO band of interest. The frequency resolution can be adjusted either by using longer recordings or by zero padding. Zero padding may be preferred because no extra noise is included in the metric calculations. Because candidate (Loubeau and Page, 2018) low-boom human perception metrics are exposure metrics, zero padding does not affect final metric values.

The final topic addressed in this report is the potential design of a compact, weather-robust microphone configuration for the X-59 measurement systems. BYU designed the COUGAR-cub, an inverted microphone configuration with a 10-inch-diameter plate, 6-inch-diameter windscreen, and a windscreen height of 8 inches. This design was compared directly against similar designs, namely the COUGAR and the COUGARxt. Overall, the COUGAR-cub had larger plate effects than had been anticipated, and further research can be done to further refine the design. Additionally, when all three designs were subjected to wind noise testing, the dominant factor in reducing wind noise appears to be total windscreen diameter rather than the thickness. This indicates that a smaller windscreen will likely suffer from increased wind noise contamination if used for X-59 measurements. A short windscreen also creates challenges for fitting a microphone inside the cavity. Therefore, further work will need to be done leading up to X-59 testing to determine an optimal design that will enable NASA and contractors to achieve the highest possible measurement fidelity.

This report has discussed in detail the work performed by BYU as part of the NASA Quesst mission. This research has contributed to several facets of the upcoming measurement campaigns, including contaminating noise mitigation, sonic boom variability, and signal processing and measurement recommendations.

4.2 Future Updates

Elements of this contractor report are being published in the open academic literature. The reader is invited to contact the first author of this report at kentgee@byu.edu for updated references.

Appendix A – Required Effective Bandwidths for Metric Calculations

This is a continuation of the discussion in Section 1.1 within this report. In this appendix, plots are included to help determine appropriate cutoff frequencies for each metric. These plots are identical in nature to Figures 4 and 7 in Anderson *et al*. (2024b). Readers are encouraged to use these plots to gain additional insight into the effects of contaminating noise on sonic booms and the efficacy of the Butterworth and brick wall filtering techniques for removing contaminating noise. A direct comparison is not made here with the work by Klos (2022) on ISO 11204 adaptations because the notion of effective bandwidth is not well-defined for those methods. The reader is referred to Figure 1.4 in this report for a comparison with the ISO 11204 adaptations for sonic boom data.

A.1. Perfectly-defined Contaminating noise

This section contains plots produced using data where the contaminating noise during the boom is perfectly known. Although the contaminating noise will not be known perfectly during X-59 field measurements, the plots in this section are useful as a limiting case where the noise is perfectly stationary. This analysis contains 8,973 unique pairings of C609 simulations and real-world measured ambient noise from QSF18. The label "n-c" indicates the noisy minus the clean metrics, or the difference created by adding the contaminating noise. The label "f-c" indicates the filtered metric value minus the clean metric value, or how close the filters are able to get to returning the metric values to the clean conditions.

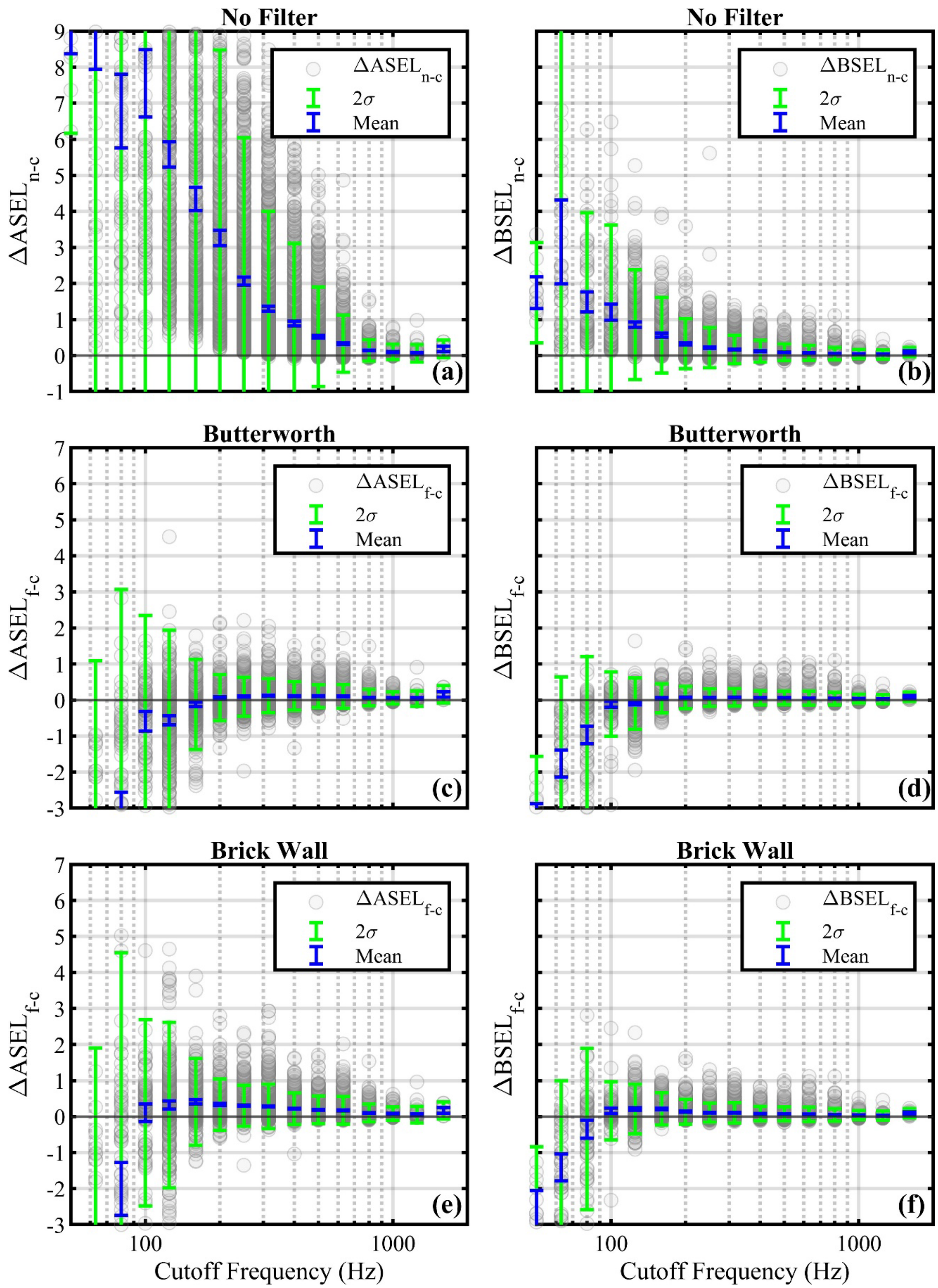

Figure A.1. Contaminating noise effects and the effects of filtering are shown on the ASEL and BSEL, both measured in decibels.

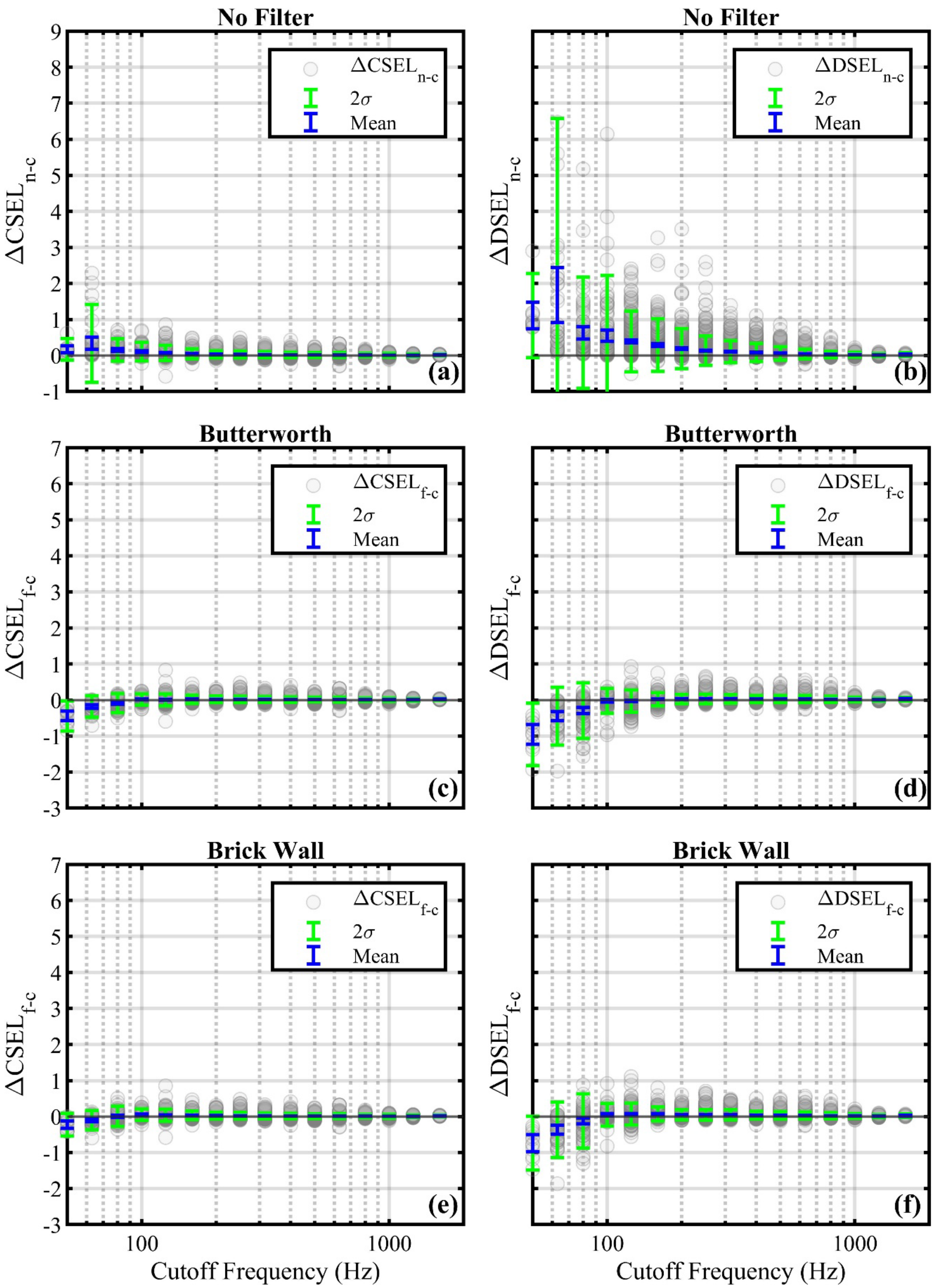

Figure A.2. Contaminating noise effects and the effects of filtering are shown on the CSEL and DSEL, both measured in decibels.

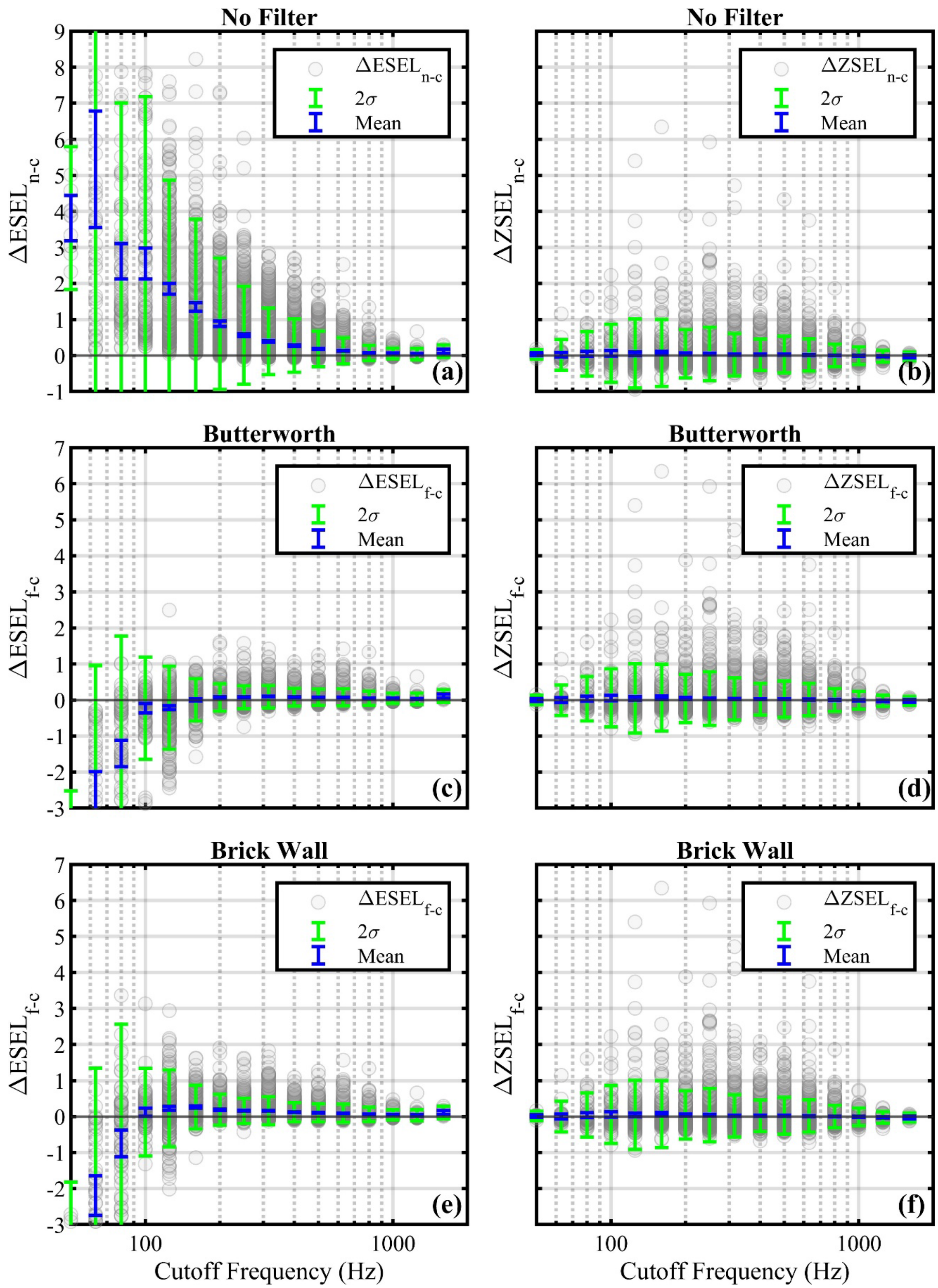

Figure A.3. Contaminating noise effects and the effects of filtering are shown on the ESEL and ZSEL, both measured in decibels.

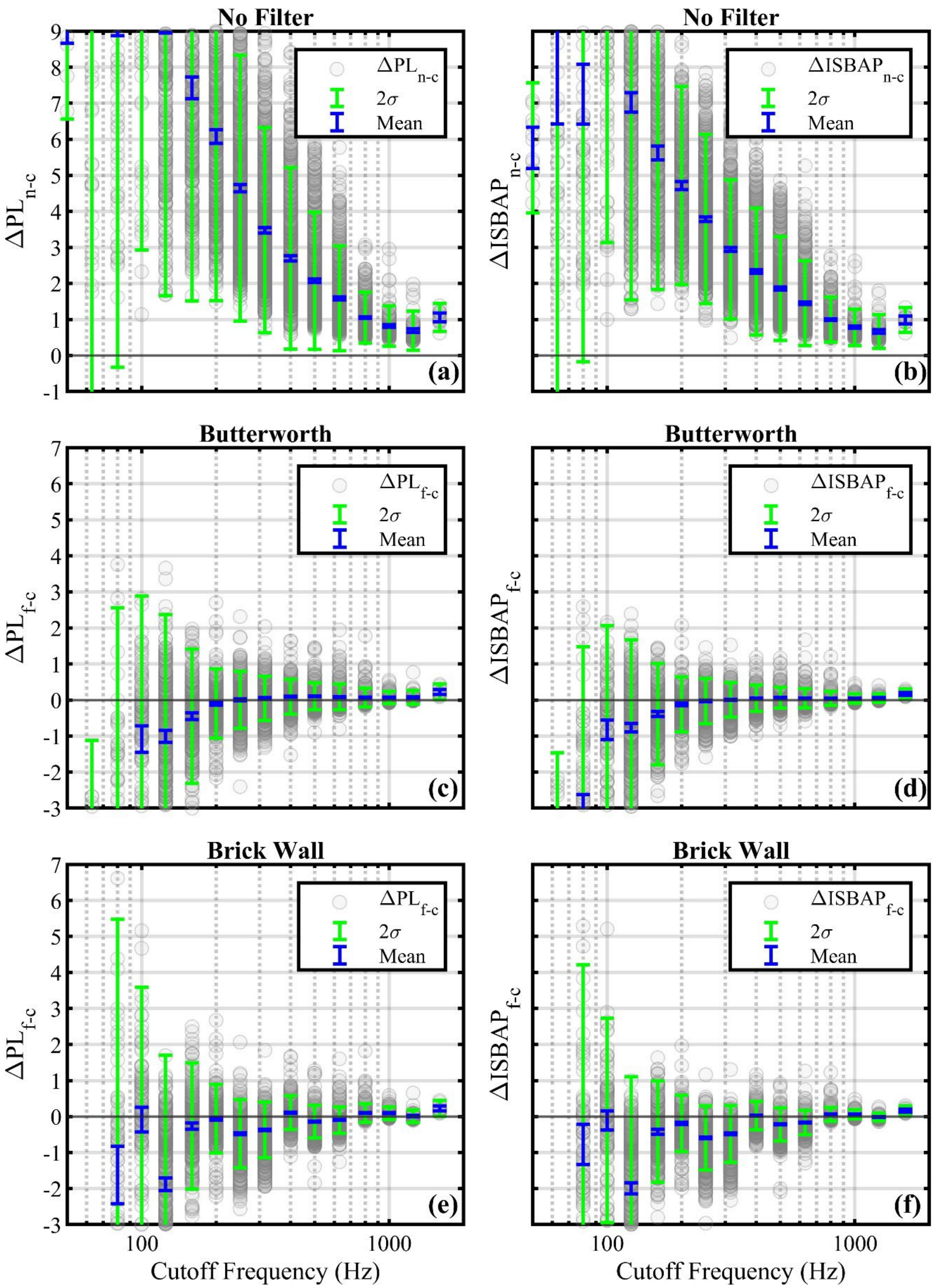

Figure A.4. Contaminating noise effects and the effects of filtering are shown on the PL and ISBAP, both measured in decibels.

A.2. Estimating Contaminating Noise from Ambient Recordings

The results in this section are created by applying 1300 ms of noise to the clean boom, exactly as described in Section 1 and shown in Figure 7 in Anderson *et al.* (2024b), where the first 650 ms of noise is used to estimate the noise during the latter half of the recording containing the sonic boom event. This is more representative of what will be encountered during X-59 measurements, where the contaminating noise is not perfectly known but can be estimated using the contaminating noise immediately preceding the boom. This analysis contains 8,956 unique pairings of C609 simulated ground waveforms and real-world measured ambient noise from QSF18. The label "n-c" indicates the noisy minus the clean metrics, or the difference created by adding the contaminating noise. The label "f-c" indicates the filtered metric value minus the clean metric value, or how close the filters are able to get to returning the metric values to the clean conditions.

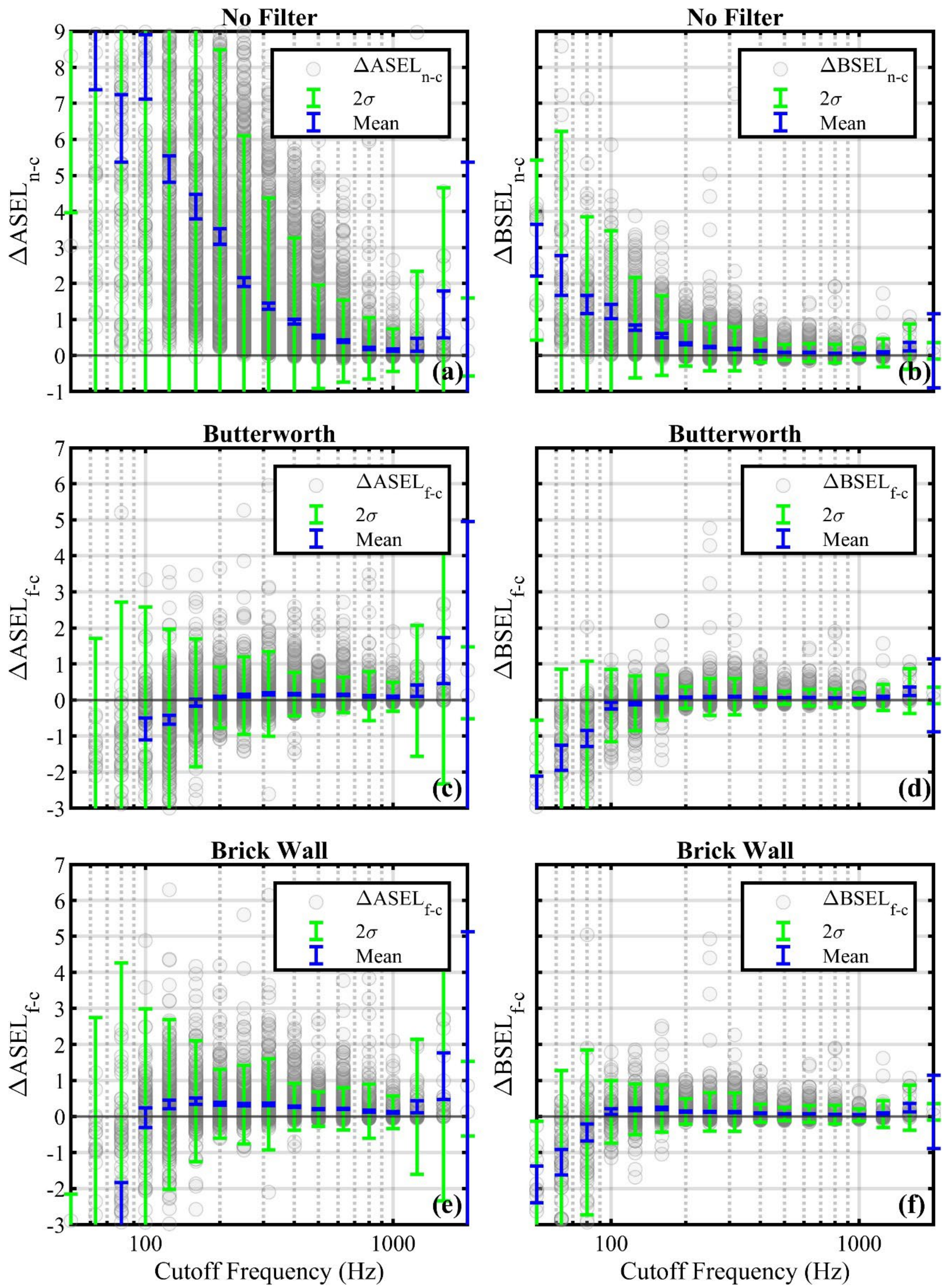

Figure A.5. Contaminating noise effects and the effects of filtering are shown on the ASEL and BSEL, both measured in decibels.

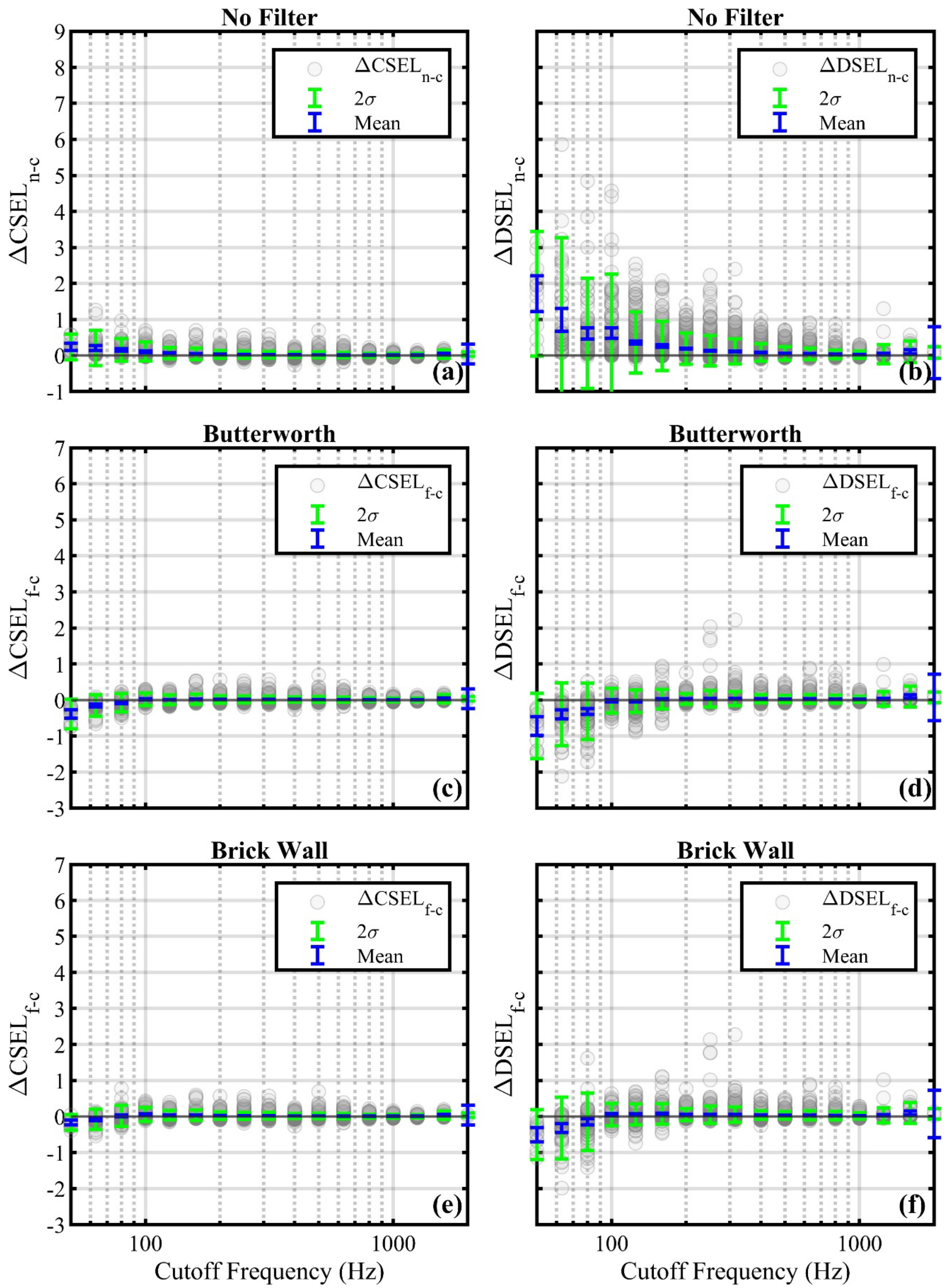

Figure A.6. Contaminating noise effects and the effects of filtering are shown on the CSEL and DSEL, both measured in decibels.

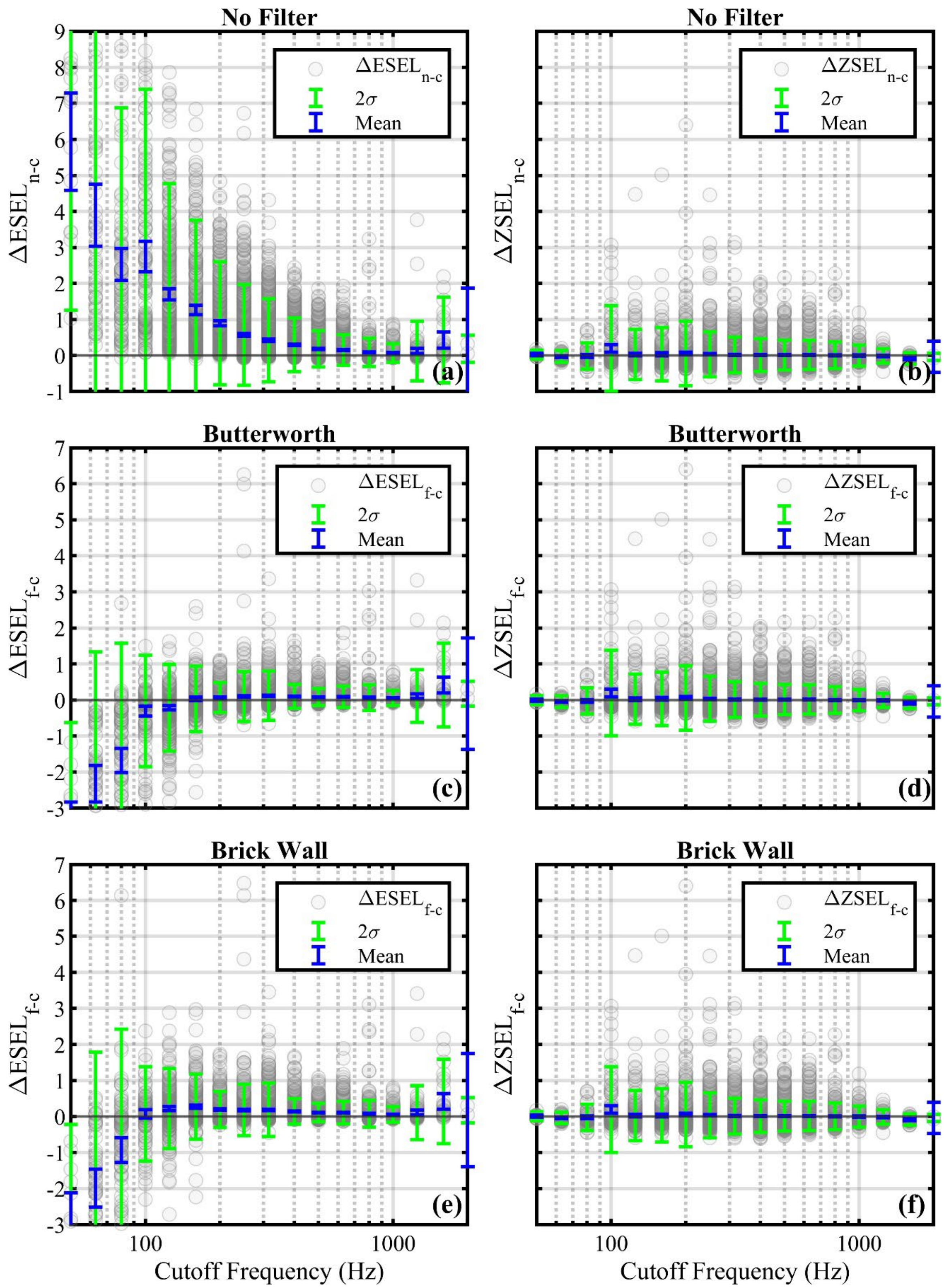

Figure A.7. Contaminating noise effects and the effects of filtering are shown on the ESEL and ZSEL, both measured in decibels.

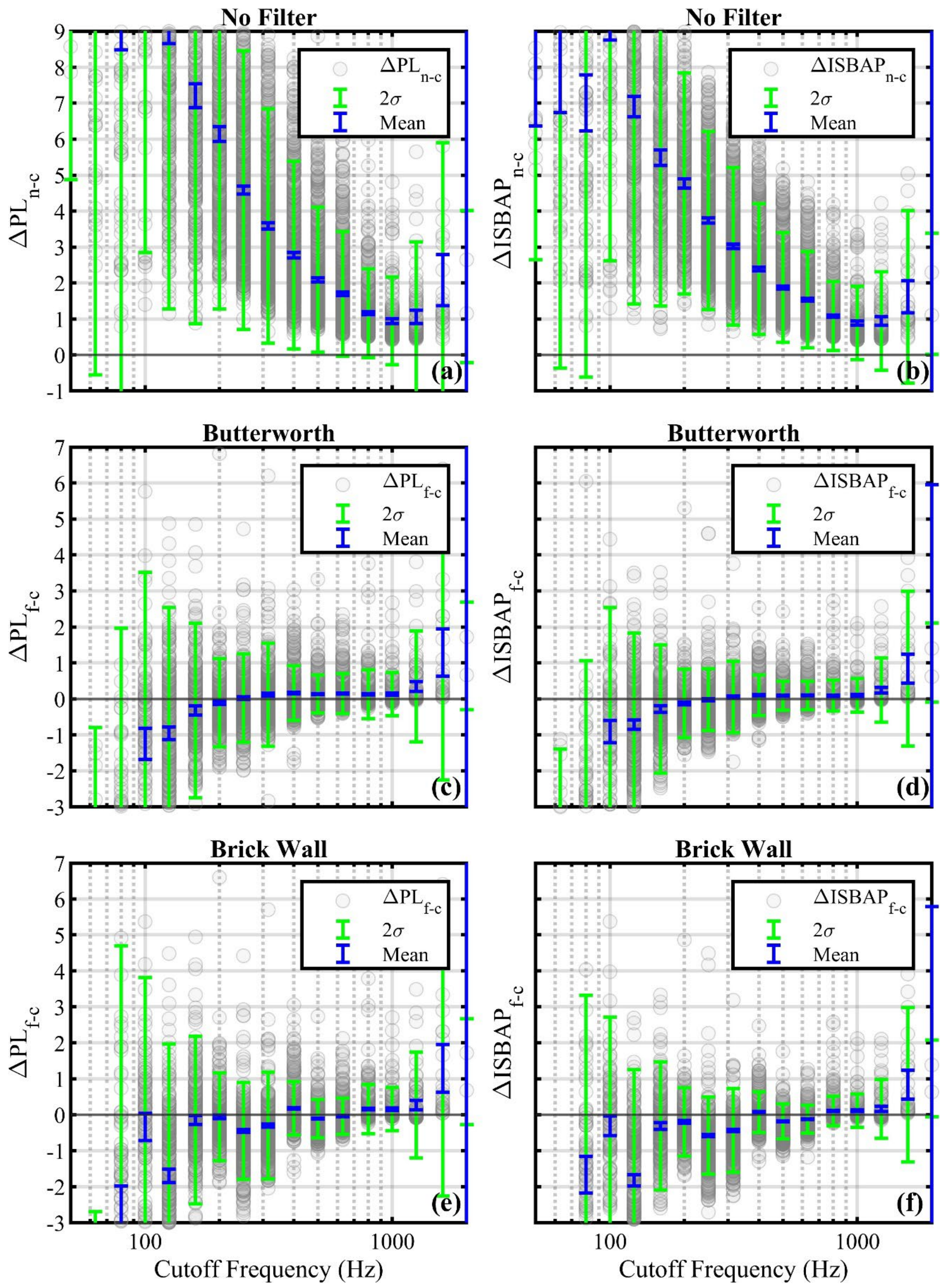

Figure A.8. Contaminating noise effects and the effects of filtering are shown on the PL and ISBAP, both measured in decibels.

Appendix B – Effects of Clipping on Sonic Boom Metrics

This appendix contains the continuation of the discussion in Section 2.1.1 In this appendix, the effects of clipping on CarpetDIEM N-waves and C609 simulated shaped booms are investigated. Each figure can be described as follows:

Clipping effects for (left) 231 measured CarpetDIEM booms and (right) 300 simulated C609 booms, shown as a function of the clipping percentage. The clipping percentage is defined as the percent of the peak pressure that has been clipped. Individual metric differences at specific clipping percentages are represented as dots. Twice the standard deviation of the distribution of data points at each clipping percentage is indicated by the green bars. The blue bars represent the 95% confidence interval for the mean value of the distribution at each clipping percentage.

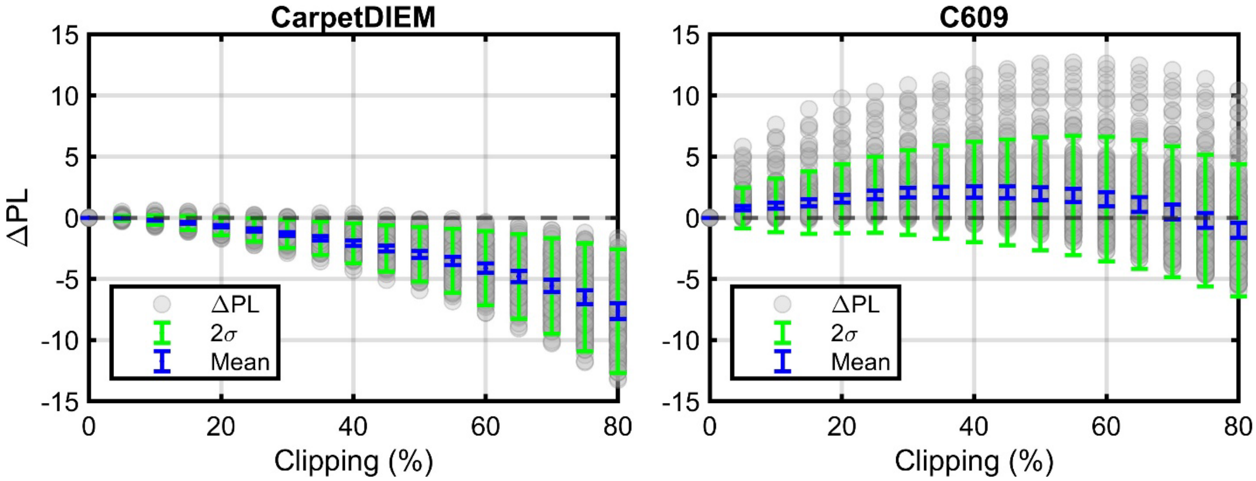

Figure B.1. Clipping effects on the PL metric.

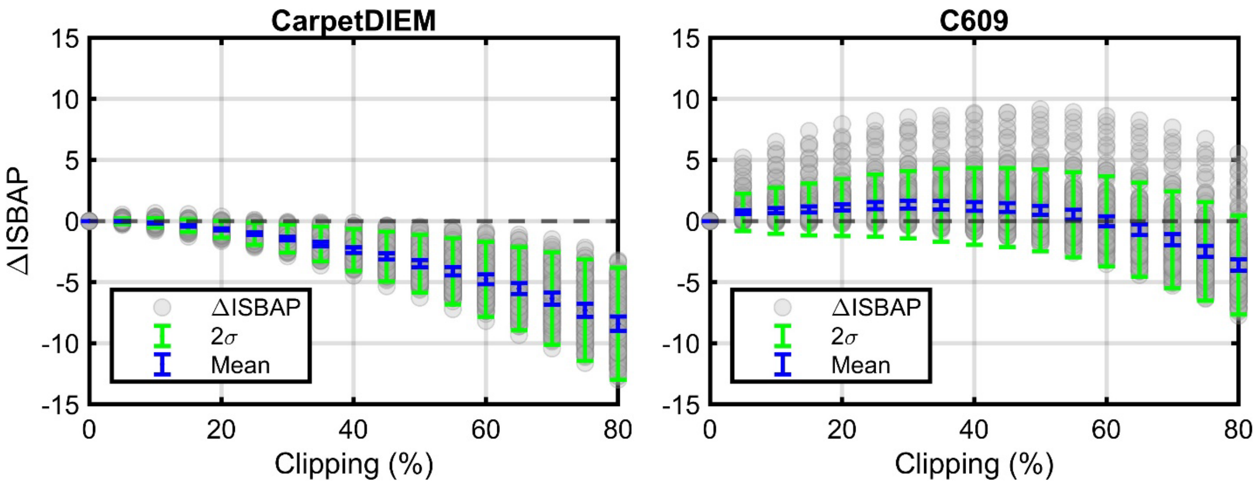

Figure B.2. Clipping effects on the ISBAP metric.

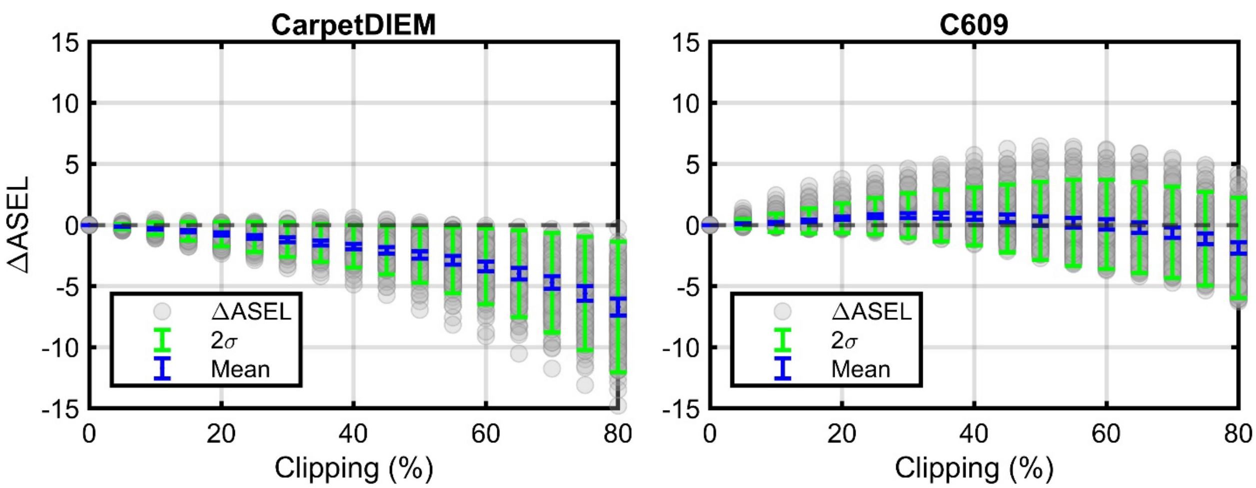

Figure B.3. Clipping effects on the ASEL metric.

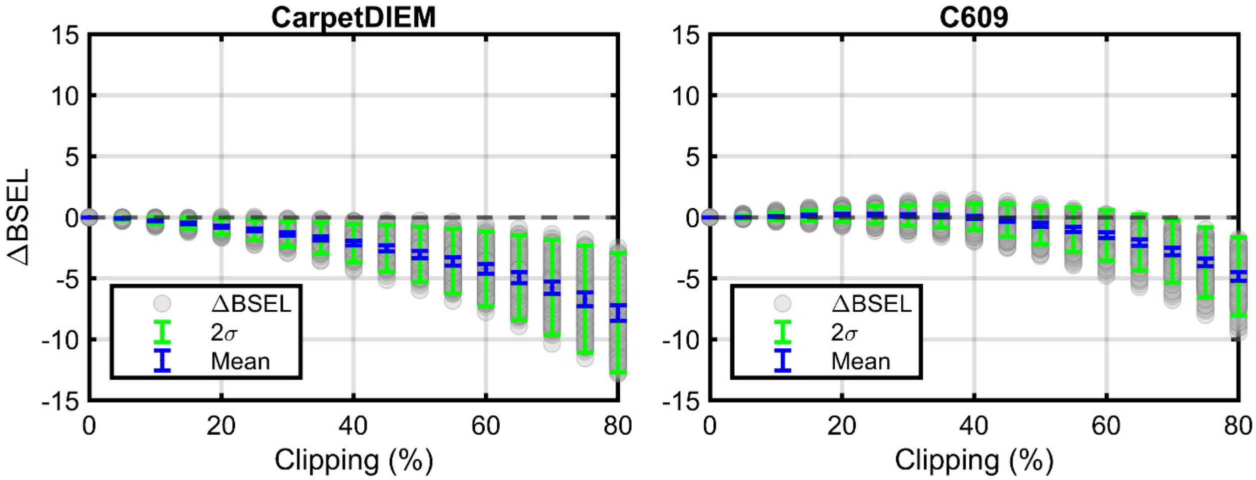

Figure B.4. Clipping effects on the BSEL metric.

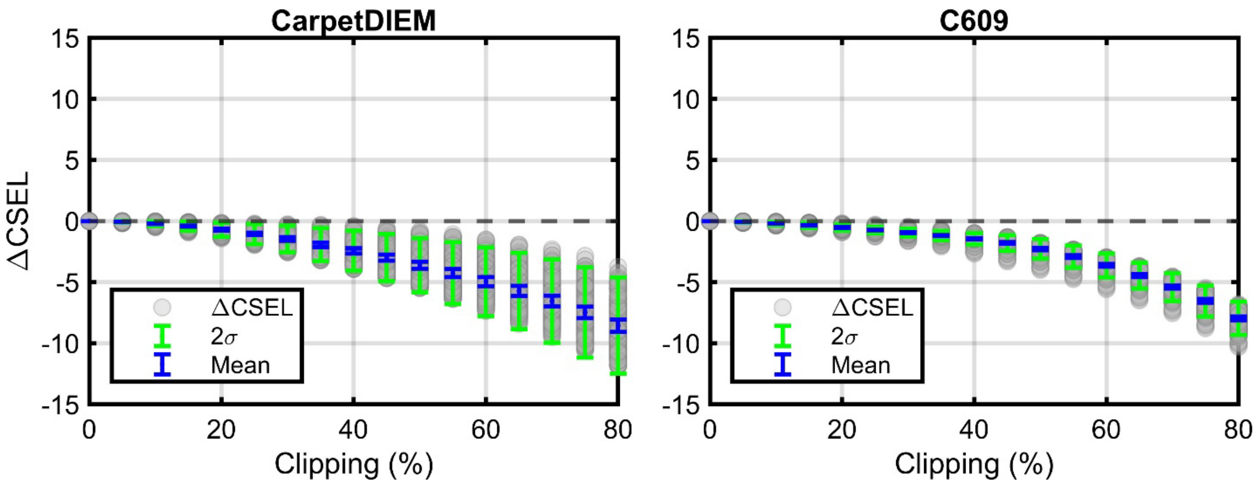

Figure B.5. Clipping effects on the CSEL metric.

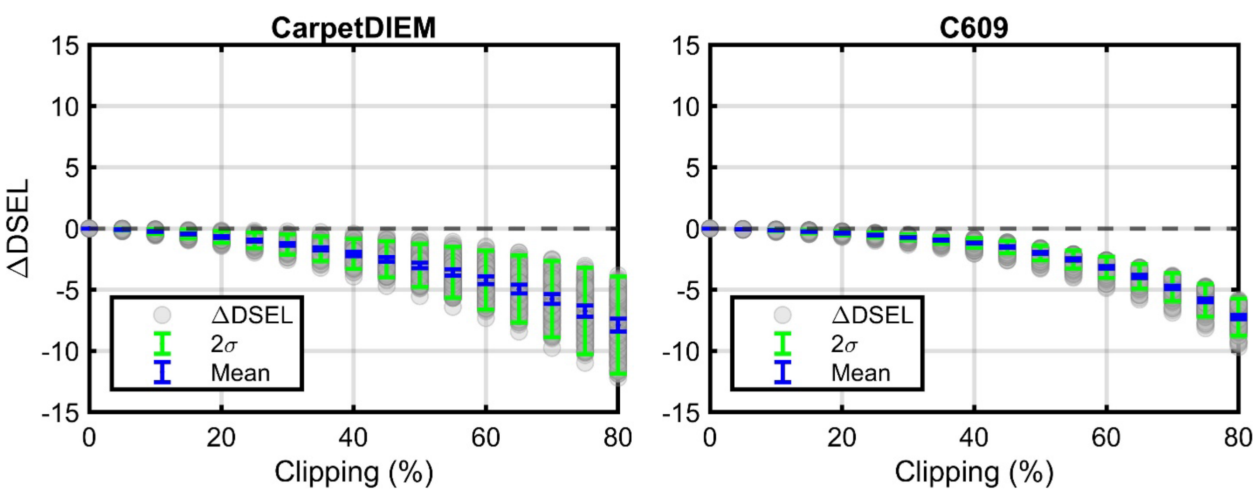

Figure B.6. Clipping effects on the DSEL metric.

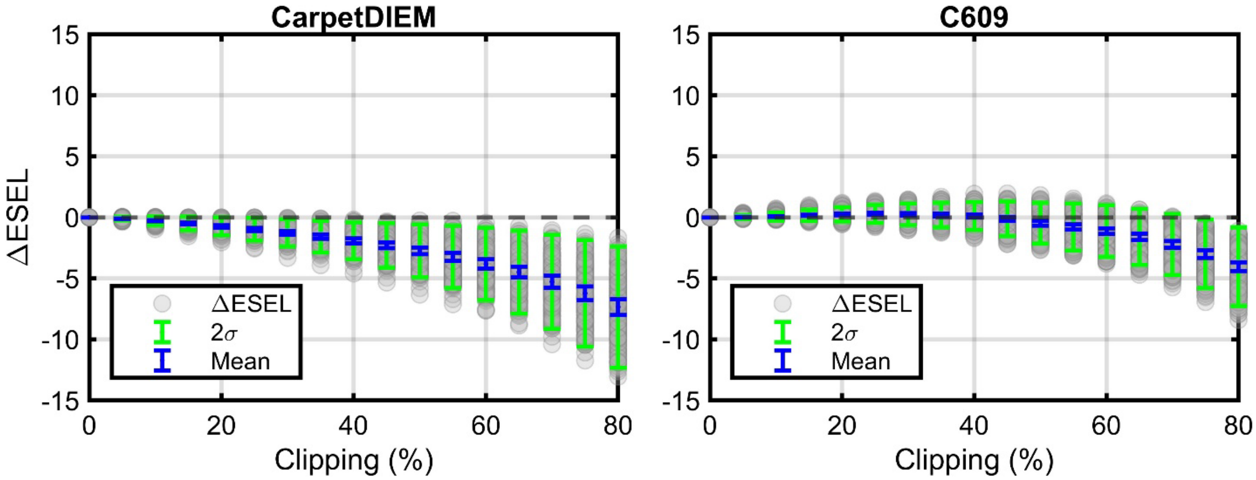

Figure B.7. Clipping effects on the ESEL metric.

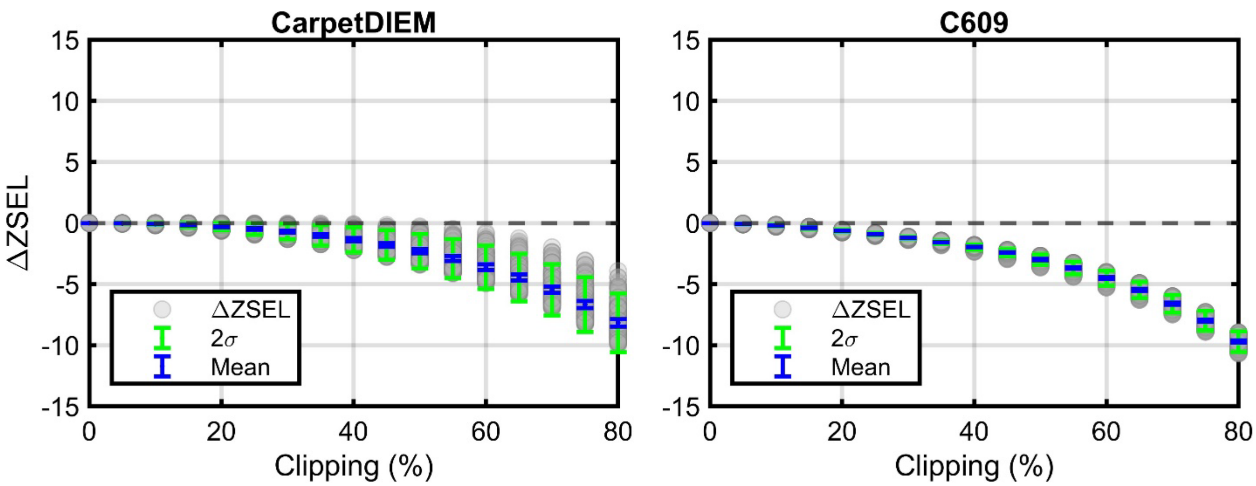

Figure B.8. Clipping effects on the ZSEL metric.

Appendix C – Lasso Regression Inputs and Outputs

This appendix documents the input and output tables for Lasso regression, as well as the input correlations. Table C.1 contains the inputs used for CarpetDIEM in Section 2.2.3 while Table C.2 lists the outputs. Table C.3 contains the correlations for the inputs. Table C.4 contains the inputs used for QSF18 in Section 2.2.4 , Table C.5 lists the outputs, and Table C.6 the input correlations.

Table C.1. Lasso regression inputs for CarpetDIEM.

#	**Input name**	**Description**
1	Flight number	There were 6 flights at CarpetDIEM I.
2	Pass number	Each flight had 4 passes, except flight 5 had 3 passes.
3	Site number	The site number the measurement was made at. Attended stations for CarpetDIEM I were limited to sites 19-54.
4	Mark time	The time of day the boom was generated by the aircraft.
5	Wind direction	Direction of the wind at the nearest ground weather station.
6	Wind speed	Wind speed at the nearest ground weather station.
7	Temperature	Temperature at the nearest ground weather station.
8	Relative humidity	Relative humidity at the nearest ground weather station.
9	Pressure	Atmospheric pressure at the nearest ground weather station.
10	Low altitude wind direction	Wind direction at 5,000 ft. elevation for the balloon launched before that flight.
11	Low altitude wind speed	Wind speed at 5,000 ft. elevation for the balloon launched before that flight.
12	Low altitude temperature	Temperature at 5,000 ft. elevation for the balloon launched before that flight.
13	Low altitude relative humidity	Relative humidity at 5,000 ft. elevation for the balloon launched before that flight.
14	Low altitude pressure	Atmospheric pressure at 5,000 ft. elevation for the balloon launched before that flight.
15	Low altitude dew point	Dew point at 5,000 ft. elevation for the balloon launched before that flight.
16	High altitude wind direction	Wind direction at 30,000 ft. elevation for the balloon launched before that flight.
17	High altitude wind speed	Wind speed at 30,000 ft. elevation for the balloon launched before that flight.

18	High altitude temperature	Temperature at 30,000 ft. elevation for the balloon launched before that flight.
19	High altitude relative humidity	Relative humidity at 30,000 ft. elevation for the balloon launched before that flight.
20	High altitude pressure	Atmospheric pressure at 30,000 ft. elevation for the balloon launched before that flight.
21	High altitude dew point	Dew point at 30,000 ft. elevation for the balloon launched before that flight.
22	Planetary boundary layer height	Height of the planetary boundary layer from CFSv2 modeled data.
23	Friction velocity	Friction velocity from CFSv2 modeled data.
24	X-plane	Location of the aircraft at time of ray emission in the x-direction.
25	Y-plane	Location of the aircraft at time of ray emission in the y-direction.
26	Altitude	Altitude of the aircraft at time of ray emission.
27	Mach	Mach number of the aircraft at time of ray emission.
28	Mach derivative	Mach number derivative of the aircraft at time of ray emission.
29	Mach 2^{nd} derivative	Mach number 2^{nd} derivative of the aircraft at time of ray emission.
30	Heading	Heading (horizontal angle) of the aircraft at time of ray emission.
31	Heading derivative	Derivative of heading (horizontal angle) of the aircraft at time of ray emission.
32	Heading 2^{nd} derivative	2^{nd} derivative of heading (horizontal angle) of the aircraft at time of ray emission.
33	Flight path angle (FPA)	Angle of the aircraft in the vertical direction at time of ray emission.
34	Flight path angle (FPA) derivative	Derivative of the angle of the aircraft in the vertical direction at time of ray emission.
35	Flight path angle (FPA) 2^{nd} derivative	2^{nd} derivative of the angle of the aircraft in the vertical direction at time of ray emission.
36	Weight	Weight of the aircraft at time of ray emission.
37	Horizontal distance	Distance from aircraft coordinates to measurement location coordinates in the horizontal direction at time of ray emission.
38	Straight-line distance	Distance from the aircraft x-y coordinates and altitude to the station x-y coordinates and altitude at time of ray emission.
39	Emission angle	Angle of the emitted ray that lands closest to the given measurement station, as predicted by PCBoom.

40	Emission angle squared	Squared angle of the emitted ray that lands closest to the given measurement station, as predicted by PCBoom.
41	Absolute value of emission angle	Absolute value of the angle of the emitted ray that lands closest to the given measurement station, as predicted by PCBoom.
42	Ambient PL	Ambient PL calculated over the 650ms immediately preceding the boom.
43	Ambient ASEL	Ambient ASEL calculated over the 650ms immediately preceding the boom.
44	Ambient BSEL	Ambient BSEL calculated over the 650ms immediately preceding the boom.
45	Ambient DSEL	Ambient DSEL calculated over the 650ms immediately preceding the boom.
46	Ambient ESEL	Ambient ESEL calculated over the 650ms immediately preceding the boom.
47	Ambient ISBAP	Ambient ISBAP calculated over the 650ms immediately preceding the boom.
48	Average ambient PL	Average ambient PL, calculated in 650ms windows and averaged over the 60s preceding the boom.
49	Average ambient ASEL	Average ambient ASEL, calculated in 650ms windows and averaged over the 60s preceding the boom.
50	Average ambient BSEL	Average ambient BSEL, calculated in 650ms windows and averaged over the 60s preceding the boom.
51	Average ambient DSEL	Average ambient DSEL, calculated in 650ms windows and averaged over the 60s preceding the boom.
52	Average ambient ESEL	Average ambient ESEL, calculated in 650ms windows and averaged over the 60s preceding the boom.
53	Average ambient ISBAP	Average ambient ISBAP, calculated in 650ms windows and averaged over the 60s preceding the boom.
54	PCBoom PL	PCBoom-modeled PL with F-function near-field input.
55	PCBoom ASEL	PCBoom-modeled ASEL with F-function near-field input.
56	PCBoom BSEL	PCBoom-modeled BSEL with F-function near-field input.
57	PCBoom DSEL	PCBoom-modeled DSEL with F-function near-field input.
58	PCBoom ESEL	PCBoom-modeled ESEL with F-function near-field input.
59	PCBoom ISBAP	PCBoom-modeled ISBAP with F-function near-field input.
60	PCBoom CFD PL	PCBoom-modeled PL with CFD near-field input.
61	PCBoom CFD ASEL	PCBoom-modeled ASEL with CFD near-field input.

62	PCBoom CFD BSEL	PCBoom-modeled BSEL with CFD near-field input.
63	PCBoom CFD DSEL	PCBoom-modeled DSEL with CFD near-field input.
64	PCBoom CFD ESEL	PCBoom-modeled ESEL with CFD near-field input.
65	PCBoom CFD ISBAP	PCBoom-modeled ISBAP with CFD near-field input.
66	PCBoom distance	Distance from the PCBoom-modeled ray landing point to the measurement station.
67	PCBoom peak pressure	PCBoom-modeled peak overpressure with F-function near-field input.
68	PCBoom CFD peak pressure	PCBoom-modeled peak overpressure with CFD near-field input.

Table C.2. Lasso regression outputs for CarpetDIEM.

#	**Output name**	**Description**
1	PL	Measured PL
2	ASEL	Measured ASEL
3	BSEL	Measured BSEL
4	DSEL	Measured DSEL
5	ESEL	Measured ESEL
6	ISBAP	Measured ISBAP
7	PCBoom PL ΔPM	PCBoom-modeled PL – measured PL
8	PCBoom ASEL ΔPM	PCBoom-modeled ASEL – measured ASEL
9	PCBoom BSEL ΔPM	PCBoom-modeled BSEL – measured BSEL
10	PCBoom DSEL ΔPM	PCBoom-modeled DSEL – measured DSEL
11	PCBoom ESEL ΔPM	PCBoom-modeled ESEL – measured ESEL
12	PCBoom ISBAP ΔPM	PCBoom-modeled ISBAP – measured ISBAP

Table C.3. Correlations for CarpetDIEM inputs used in Lasso regression. Positive correlations are shown in blue and negative correlations are shown in red.

	Flight number	Pass number	Station number	Mark time	Wind direction	Wind speed	Temperature	Relative humidity	Pressure	Low alt. wind speed	Low alt. wind speed	Low alt. temperature	Low alt. relative humidity	Low alt. pressure	Low alt. dew point	High alt. wind direction	High alt. wind speed	High alt. temperature	High alt. relative humidity	High alt. pressure	Hight alt. dew point	Planetary boundary layer height
Flight number	1.00	-0.05	-0.04	0.07	-0.23	0.04	0.06	-0.30	0.04	-0.47	0.06	0.88	-0.73	0.22	-0.67	-0.89	-0.46	-0.25	0.87	0.52	0.93	0.02
Pass number	-0.05	1.00	0.00	0.18	0.17	0.07	0.13	-0.06	0.02	-0.09	0.03	-0.05	0.02	0.08	0.02	0.07	0.09	0.08	-0.10	0.01	-0.07	0.25
Station number	-0.04	0.00	1.00	0.01	0.29	-0.29	-0.06	0.18	-0.87	0.03	0.00	-0.02	0.02	0.00	0.02	0.05	0.00	0.01	-0.04	-0.02	-0.04	0.01
Mark time	0.07	0.18	0.01	1.00	0.47	0.38	0.92	-0.80	0.03	-0.61	0.56	0.29	-0.29	0.81	-0.17	0.25	0.03	0.64	-0.41	0.45	-0.19	0.95
Wind direction	-0.23	0.17	0.29	0.47	1.00	0.08	0.39	-0.24	-0.34	-0.23	0.42	0.05	-0.15	0.49	-0.12	0.35	-0.16	0.50	-0.44	0.29	-0.26	0.52
Wind speed	0.04	0.07	-0.29	0.38	0.08	1.00	0.41	-0.50	0.30	-0.02	-0.05	0.14	-0.12	0.16	-0.01	0.20	0.00	-0.04	-0.08	-0.05	-0.13	0.33
Temperature	0.06	0.13	-0.06	0.92	0.39	0.41	1.00	-0.85	0.12	-0.63	0.56	0.25	-0.26	0.78	-0.17	0.20	0.05	0.65	-0.39	0.46	-0.16	0.86
Relative humidity	-0.30	-0.06	0.18	-0.80	-0.24	-0.50	-0.85	1.00	-0.15	0.50	-0.47	-0.50	0.43	-0.66	0.28	0.00	0.19	-0.42	0.09	-0.46	-0.07	-0.77
Pressure	0.04	0.02	-0.87	0.03	-0.34	0.30	0.12	-0.15	1.00	-0.09	0.05	0.03	-0.03	0.06	-0.05	-0.05	0.00	0.05	0.01	0.07	0.05	0.02
Low alt. wind speed	-0.47	-0.09	0.03	-0.61	-0.23	-0.02	-0.63	0.50	-0.09	1.00	-0.50	-0.50	0.61	-0.85	0.67	0.32	0.15	-0.53	-0.05	-0.79	-0.41	-0.50
Low alt. wind speed	0.06	0.03	0.00	0.56	0.42	-0.05	0.56	-0.47	0.05	-0.50	1.00	0.35	-0.28	0.73	-0.26	-0.09	-0.38	0.91	-0.28	0.78	0.08	0.71
Low alt. temperature	0.88	-0.05	-0.02	0.29	0.05	0.14	0.25	-0.50	0.03	-0.50	0.35	1.00	-0.91	0.51	-0.80	-0.68	-0.76	0.02	0.66	0.74	0.82	0.32
Low alt. relative humidity	-0.73	0.02	0.02	-0.29	-0.15	-0.12	-0.26	0.43	-0.03	0.61	-0.28	-0.91	1.00	-0.64	0.96	0.49	0.79	-0.07	-0.51	-0.78	-0.72	-0.28
Low alt. pressure	0.22	0.08	0.00	0.81	0.49	0.16	0.78	-0.66	0.06	-0.85	0.73	0.51	-0.64	1.00	-0.62	0.01	-0.37	0.75	-0.24	0.84	0.14	0.79
Low alt. dew point	-0.67	0.02	0.02	-0.17	-0.12	-0.01	-0.17	0.28	-0.05	0.67	-0.26	-0.80	0.96	-0.62	1.00	0.50	0.74	-0.09	-0.48	-0.79	-0.73	-0.15
High alt. wind diretion	-0.89	0.07	0.05	0.25	0.35	0.20	0.20	0.00	-0.05	0.32	-0.09	-0.68	0.49	0.01	0.50	1.00	0.39	0.22	-0.89	-0.46	-0.95	0.24
High alt. wind speed	-0.46	0.09	0.00	0.03	-0.16	0.00	0.05	0.19	0.00	0.15	-0.38	-0.76	0.79	-0.37	0.74	0.39	1.00	-0.08	-0.44	-0.66	-0.59	-0.12
High alt. temperature	-0.25	0.08	0.01	0.64	0.50	-0.04	0.65	-0.42	0.05	-0.53	0.91	0.02	-0.07	0.75	-0.09	0.22	-0.08	1.00	-0.61	0.62	-0.24	0.72
High alt. relative humidity	0.87	-0.10	-0.04	-0.41	-0.44	-0.08	-0.39	0.09	0.01	-0.05	-0.28	0.66	-0.51	-0.24	-0.48	-0.89	-0.44	-0.61	1.00	0.18	0.90	-0.42
High alt. pressure	0.52	0.01	-0.02	0.45	0.29	-0.05	0.46	-0.46	0.07	-0.79	0.78	0.74	-0.78	0.84	-0.79	-0.46	-0.66	0.62	0.18	1.00	0.57	0.51
Hight alt. dew point	0.93	-0.07	-0.04	-0.19	-0.26	-0.13	-0.16	-0.07	0.05	-0.41	0.08	0.82	-0.72	0.14	-0.73	-0.95	-0.59	-0.24	0.90	0.57	1.00	-0.19
Planetary boundary layer height	0.02	0.25	0.01	0.95	0.52	0.33	0.86	-0.77	0.02	-0.50	0.71	0.32	-0.28	0.79	-0.15	0.24	-0.12	0.72	-0.42	0.51	-0.19	1.00
Friction velociy	-0.39	0.23	0.02	0.75	0.41	0.40	0.67	-0.47	-0.01	-0.19	0.06	-0.27	0.20	0.36	0.29	0.68	0.49	0.33	-0.67	-0.17	-0.65	0.64
X-plane	0.48	0.41	-0.05	0.31	-0.11	0.10	0.29	-0.28	0.05	-0.50	-0.14	0.30	-0.30	0.23	-0.29	-0.31	0.16	-0.12	0.29	0.16	0.33	0.17
Y-plane	0.53	0.37	-0.06	0.22	-0.18	0.08	0.21	-0.24	0.06	-0.43	-0.18	0.32	-0.29	0.15	-0.27	-0.38	0.14	-0.19	0.37	0.13	0.39	0.09
Altitude	0.67	0.06	-0.04	0.10	-0.36	0.07	0.11	-0.15	0.05	-0.44	-0.36	0.31	-0.22	-0.01	-0.21	-0.55	0.31	-0.38	0.55	0.01	0.50	-0.11
Mach	0.17	0.54	-0.02	0.36	0.15	0.34	0.29	-0.36	-0.01	-0.15	0.09	0.30	-0.30	0.27	-0.21	0.03	-0.19	0.04	0.04	0.17	0.06	0.40
Mach Derivative	0.21	0.11	-0.01	-0.04	-0.12	0.10	0.04	0.03	0.13	-0.09	-0.22	0.07	-0.07	-0.07	-0.07	-0.17	0.11	-0.22	0.21	-0.06	0.17	-0.11
Mach 2nd Derivative	0.29	0.09	0.00	-0.18	-0.33	0.06	-0.13	0.18	0.14	-0.02	-0.42	0.04	-0.02	-0.25	-0.03	-0.27	0.20	-0.43	0.36	-0.20	0.24	-0.29
Heading	0.48	0.45	-0.02	0.31	-0.10	0.11	0.28	-0.27	0.04	-0.49	-0.13	0.31	-0.31	0.24	-0.30	-0.30	0.13	-0.12	0.29	0.17	0.33	0.18
Heading derivative	0.30	-0.23	-0.08	0.09	-0.05	0.06	0.13	-0.14	0.15	-0.21	0.05	0.25	-0.20	0.12	-0.18	-0.25	-0.06	-0.02	0.22	0.17	0.25	0.03
Heading 2nd derivative	0.00	0.23	0.10	0.10	0.11	0.09	0.10	0.00	0.01	-0.13	0.14	0.06	-0.11	0.16	-0.12	0.01	-0.10	0.14	-0.06	0.16	0.02	0.14
FPA	-0.18	0.07	0.05	0.15	0.16	-0.12	0.08	-0.07	-0.15	-0.02	0.24	-0.10	0.11	0.12	0.12	0.15	0.04	0.27	-0.24	0.07	-0.18	0.20
FPA derivative	-0.20	-0.16	0.04	0.18	0.32	-0.09	0.13	-0.16	-0.17	-0.10	0.38	0.03	-0.10	0.31	-0.11	0.20	-0.23	0.39	-0.29	0.26	-0.14	0.24
FPA 2nd derivative	-0.18	-0.26	0.01	0.15	0.32	-0.06	0.14	-0.17	-0.12	-0.10	0.41	0.07	-0.16	0.33	-0.17	0.19	-0.32	0.40	-0.27	0.32	-0.11	0.22
Weight	0.03	-1.00	0.01	-0.15	-0.13	-0.05	-0.10	0.04	-0.02	0.09	0.01	0.06	-0.04	-0.04	-0.03	-0.04	-0.12	-0.04	0.07	0.01	0.05	-0.21
Horizontal distance	0.15	-0.02	0.09	-0.05	-0.16	0.03	0.00	0.11	0.13	-0.04	-0.08	0.08	-0.04	-0.05	-0.04	-0.15	0.02	-0.11	0.16	0.00	0.14	-0.08
Straight-line distance	0.18	-0.02	0.09	-0.04	-0.18	0.04	0.00	0.10	0.13	-0.06	-0.09	0.09	-0.05	-0.05	-0.05	-0.18	0.03	-0.12	0.18	0.00	0.16	-0.08
Emission angle	-0.05	-0.02	-0.42	-0.01	-0.01	0.16	-0.03	-0.01	0.38	0.03	0.05	0.00	-0.02	0.03	-0.02	0.05	-0.07	0.04	-0.04	0.03	-0.03	0.02
Emission angle squared	-0.12	-0.01	-0.28	-0.02	-0.10	0.18	0.05	0.04	0.40	0.08	0.00	-0.09	0.07	-0.03	0.07	0.11	0.02	0.02	-0.09	-0.06	-0.11	-0.01
Abs. value of emission angle	-0.12	-0.01	-0.20	-0.01	-0.09	0.16	0.07	0.04	0.37	0.07	0.01	-0.08	0.07	-0.02	0.07	0.10	0.02	0.03	-0.10	-0.05	-0.10	0.00
Ambient PL	0.15	0.01	-0.34	-0.07	-0.31	0.20	-0.02	-0.06	0.51	0.05	-0.13	0.09	-0.05	-0.10	-0.03	-0.12	-0.02	-0.19	0.18	-0.06	0.12	-0.09
Ambient ASEL	0.14	0.01	-0.35	-0.07	-0.31	0.20	-0.02	-0.07	0.51	0.05	-0.13	0.08	-0.05	-0.10	-0.03	-0.12	-0.02	-0.18	0.18	-0.05	0.12	-0.08
Ambient BSEL	0.26	0.00	-0.37	-0.14	-0.43	0.22	-0.08	-0.04	0.52	0.08	-0.25	0.16	-0.11	-0.18	-0.08	-0.23	-0.05	-0.34	0.34	-0.09	0.23	-0.17
Ambient DSEL	0.18	0.00	-0.35	-0.04	-0.33	0.24	0.01	-0.09	0.52	0.01	-0.16	0.11	-0.08	-0.08	-0.06	-0.13	-0.01	-0.21	0.20	-0.06	0.14	-0.08
Ambient ESEL	0.17	0.01	-0.35	-0.07	-0.32	0.20	-0.01	-0.07	0.51	0.02	-0.14	0.11	-0.07	-0.09	-0.05	-0.15	-0.02	-0.19	0.20	-0.04	0.15	-0.09
Ambient ISBAP	0.22	0.00	-0.36	-0.09	-0.37	0.24	-0.04	-0.06	0.53	0.05	-0.22	0.14	-0.10	-0.13	-0.07	-0.17	-0.03	-0.29	0.27	-0.09	0.18	-0.12
Avg. ambient PL	0.09	0.02	-0.33	-0.09	-0.26	0.24	-0.04	-0.04	0.50	0.10	-0.11	0.06	-0.02	-0.12	0.00	-0.08	-0.05	-0.16	0.14	-0.07	0.08	-0.08
Avg. ambient ASEL	0.09	0.02	-0.34	-0.09	-0.26	0.24	-0.04	-0.05	0.49	0.09	-0.11	0.06	-0.02	-0.11	0.00	-0.08	-0.04	-0.16	0.14	-0.07	0.08	-0.08
Avg. ambient BSEL	0.19	0.03	-0.40	-0.18	-0.39	0.29	-0.13	-0.02	0.55	0.17	-0.21	0.13	-0.07	-0.21	-0.03	-0.17	-0.10	-0.31	0.29	-0.11	0.18	-0.16
Avg. ambient DSEL	0.10	0.04	-0.36	-0.06	-0.27	0.28	-0.02	-0.08	0.53	0.09	-0.12	0.08	-0.04	-0.10	-0.01	-0.07	-0.05	-0.17	0.14	-0.06	0.08	-0.05
Avg. ambient ESEL	0.10	0.03	-0.34	-0.09	-0.27	0.24	-0.04	-0.06	0.50	0.08	-0.10	0.07	-0.03	-0.11	-0.01	-0.10	-0.05	-0.16	0.15	-0.06	0.10	-0.08
Avg. ambient ISBAP	0.13	0.04	-0.38	-0.12	-0.32	0.30	-0.08	-0.04	0.55	0.15	-0.18	0.10	-0.06	-0.16	-0.02	-0.10	-0.08	-0.25	0.21	-0.10	0.12	-0.10
PCBoom PL	-0.03	-0.05	-0.42	-0.10	-0.11	0.07	-0.11	-0.06	0.21	0.20	-0.15	-0.06	0.10	-0.19	0.14	0.03	0.06	-0.17	0.05	-0.19	-0.05	-0.09
PCBoom ASEL	0.03	-0.05	-0.40	-0.04	-0.08	0.07	-0.05	-0.12	0.19	0.11	-0.09	0.01	0.03	-0.10	0.06	-0.01	0.01	-0.12	0.07	-0.10	0.00	-0.04
PCBoom BSEL	0.08	-0.03	-0.41	0.01	-0.05	0.08	0.00	-0.16	0.21	0.00	-0.05	0.07	-0.05	-0.01	-0.03	-0.05	-0.02	-0.07	0.08	-0.01	0.06	0.00
PCBoom DSEL	0.04	-0.04	-0.41	-0.02	-0.07	0.08	-0.04	-0.13	0.21	0.06	-0.08	0.02	0.01	-0.07	0.03	-0.02	0.01	-0.10	0.07	-0.07	0.02	-0.03
PCBoom ESEL	0.05	-0.04	-0.41	-0.02	-0.07	0.07	-0.03	-0.13	0.20	0.05	-0.08	0.03	0.00	-0.06	0.02	-0.03	0.01	-0.10	0.07	-0.06	0.03	-0.03
PCBoom ISBAP	-0.02	-0.04	-0.43	-0.08	-0.10	0.08	-0.09	-0.08	0.23	0.17	-0.14	-0.05	0.09	-0.16	0.12	0.03	0.05	-0.16	0.05	-0.16	-0.04	-0.08
PCBoom CFD PL	-0.05	-0.03	-0.46	-0.13	-0.14	0.09	-0.13	-0.04	0.27	0.23	-0.18	-0.09	0.13	-0.22	0.16	0.04	0.06	-0.20	0.04	-0.22	-0.06	-0.13
PCBoom CFD ASEL	0.00	-0.03	-0.45	-0.06	-0.10	0.10	-0.06	-0.11	0.24	0.14	-0.11	-0.02	0.06	-0.13	0.09	0.01	0.03	-0.14	0.06	-0.13	-0.02	-0.06
PCBoom CFD BSEL	0.05	0.00	-0.46	-0.01	-0.07	0.11	-0.01	-0.14	0.26	0.05	-0.07	0.03	0.00	-0.05	0.02	-0.02	0.00	-0.09	0.06	-0.05	0.02	-0.02
PCBoom CFD DSEL	0.00	-0.01	-0.46	-0.06	-0.09	0.10	-0.06	-0.10	0.26	0.12	-0.11	-0.02	0.05	-0.12	0.08	0.00	0.03	-0.13	0.05	-0.12	-0.02	-0.06
PCBoom CFD ESEL	0.01	-0.01	-0.45	-0.06	-0.09	0.09	-0.05	-0.11	0.25	0.10	-0.10	-0.01	0.04	-0.11	0.06	-0.01	0.03	-0.12	0.06	-0.10	0.00	-0.06
PCBoom CFD ISBAP	-0.04	-0.02	-0.47	-0.12	-0.13	0.09	-0.11	-0.05	0.28	0.21	-0.17	-0.08	0.11	-0.20	0.14	0.04	0.06	-0.18	0.04	-0.20	-0.06	-0.12
PCBoom Distance	0.14	-0.04	-0.06	0.06	-0.10	-0.02	0.08	-0.06	0.09	-0.11	-0.03	0.09	-0.08	0.05	-0.07	-0.10	0.03	-0.04	0.10	0.04	0.10	0.01
PCBoom peak pressure	0.14	-0.01	-0.48	0.08	-0.11	0.09	0.08	-0.20	0.29	-0.09	-0.07	0.07	-0.05	0.02	-0.03	-0.08	0.08	-0.08	0.09	-0.01	0.08	0.02
PCBoom CFD peak pressure	0.10	-0.02	-0.52	0.06	-0.13	0.11	0.08	-0.19	0.34	-0.04	-0.08	0.04	-0.01	-0.02	0.02	-0.06	0.09	-0.08	0.07	-0.05	0.04	0.00

	Friction velociy	X-plane	Y-plane	Altitude	Mach	Mach derivative	Mach 2nd derivative	Heading	Heading derivative	Heading 2nd derivative	FPA	FPA derivative	FPA 2nd derivative	Weight	Horizontal distance	Straight-line distance	Emission angle	Emission angle squared	Abs. value of emission angle	Ambient PL
Flight number	-0.39	0.48	0.53	0.67	0.17	0.21	0.29	0.48	0.30	0.00	-0.18	-0.20	-0.18	0.03	0.15	0.18	-0.05	-0.12	-0.12	0.15
Pass number	0.23	0.41	0.37	0.06	0.54	0.11	0.09	0.45	-0.23	0.23	0.07	-0.16	-0.26	-1.00	-0.02	-0.02	-0.02	-0.01	-0.01	0.01
Station number	0.02	-0.05	-0.06	-0.04	-0.02	-0.01	0.00	-0.02	-0.08	0.10	0.05	0.04	0.01	0.01	0.09	0.09	-0.42	-0.28	-0.20	-0.34
Mark time	0.75	0.31	0.22	0.10	0.36	-0.04	-0.18	0.31	0.09	0.10	0.15	0.18	0.15	-0.15	-0.05	-0.04	-0.01	-0.02	-0.01	-0.07
Wind direction	0.41	-0.11	-0.18	-0.36	0.15	-0.12	-0.33	-0.10	-0.05	0.11	0.16	0.32	0.32	-0.13	-0.16	-0.18	-0.01	-0.10	-0.09	-0.31
Wind speed	0.40	0.10	0.08	0.07	0.34	0.10	0.06	0.11	0.06	0.09	-0.12	-0.09	-0.06	-0.05	0.03	0.04	0.16	0.18	0.16	0.20
Temperature	0.67	0.29	0.21	0.11	0.29	0.04	-0.13	0.28	0.13	0.10	0.08	0.13	0.14	-0.10	0.00	0.00	-0.03	0.05	0.07	-0.02
Relative humidity	-0.47	-0.28	-0.24	-0.15	-0.36	0.03	0.18	-0.27	-0.14	0.00	-0.07	-0.16	-0.17	0.04	0.11	0.10	-0.01	0.04	0.04	-0.06
Pressure	-0.01	0.05	0.06	0.05	-0.01	0.13	0.14	0.04	0.15	0.01	-0.15	-0.17	-0.12	-0.02	0.13	0.13	0.38	0.40	0.37	0.51
Low alt. wind speed	-0.19	-0.50	-0.43	-0.44	-0.15	-0.09	-0.02	-0.49	-0.21	-0.13	-0.02	-0.10	-0.10	0.09	-0.04	-0.06	0.03	0.08	0.07	0.05
Low alt. wind speed	0.06	-0.14	-0.18	-0.36	0.09	-0.22	-0.42	-0.13	0.05	0.14	0.24	0.38	0.41	0.01	-0.08	-0.09	0.05	0.00	0.01	-0.13
Low alt. temperature	-0.27	0.30	0.32	0.31	0.30	0.07	0.04	0.31	0.25	0.06	-0.10	0.03	0.07	0.06	0.08	0.09	0.00	-0.09	-0.08	0.09
Low alt. relative humidity	0.20	-0.30	-0.29	-0.22	-0.30	-0.07	-0.02	-0.31	-0.20	-0.11	0.11	-0.10	-0.16	-0.04	-0.04	-0.05	-0.02	0.07	0.07	-0.05
Low alt. pressure	0.36	0.23	0.15	-0.01	0.27	-0.07	-0.25	0.24	0.12	0.16	0.12	0.31	0.33	-0.04	-0.05	-0.05	0.03	-0.03	-0.02	-0.10
Low alt. dew point	0.29	-0.29	-0.27	-0.21	-0.21	-0.07	-0.03	-0.30	-0.18	-0.12	0.12	-0.11	-0.17	-0.03	-0.04	-0.05	-0.02	0.07	0.07	-0.03
High alt. wind diretion	0.68	-0.31	-0.38	-0.55	0.03	-0.17	-0.27	-0.30	-0.25	0.01	0.15	0.20	0.19	-0.04	-0.15	-0.18	0.05	0.11	0.10	-0.12
High alt. wind speed	0.49	0.16	0.14	0.31	-0.19	0.11	0.20	0.13	-0.06	-0.10	0.04	-0.23	-0.32	-0.12	0.02	0.03	-0.07	0.02	0.02	-0.02
High alt. temperature	0.33	-0.12	-0.19	-0.38	0.04	-0.22	-0.43	-0.12	-0.02	0.14	0.27	0.39	0.40	-0.04	-0.11	-0.12	0.04	0.02	0.03	-0.19
High alt. relative humidity	-0.67	0.29	0.37	0.55	0.04	0.21	0.36	0.29	0.22	-0.06	-0.24	-0.29	-0.27	0.07	0.16	0.18	-0.04	-0.09	-0.10	0.18
High alt. pressure	-0.17	0.16	0.13	0.01	0.17	-0.06	-0.20	0.17	0.17	0.16	0.07	0.26	0.32	0.01	0.00	0.00	0.03	-0.06	-0.05	-0.06
Hight alt. dew point	-0.65	0.33	0.39	0.50	0.06	0.17	0.24	0.33	0.25	0.02	-0.18	-0.14	-0.11	0.05	0.14	0.16	-0.03	-0.11	-0.10	0.12
Planetary boundary layer height	0.64	0.17	0.09	-0.11	0.40	-0.11	-0.29	0.18	0.03	0.14	0.20	0.24	0.22	-0.21	-0.08	-0.08	0.02	-0.01	0.00	-0.09
Friction velociy	1.00	0.17	0.07	0.03	0.18	-0.02	-0.09	0.16	-0.04	0.00	0.14	0.06	0.00	-0.21	-0.07	-0.06	-0.01	0.03	0.03	-0.08
X-plane	0.17	1.00	0.98	0.71	0.31	0.29	0.31	0.98	0.04	0.09	-0.05	-0.28	-0.38	-0.44	0.01	0.04	-0.09	-0.19	-0.16	0.11
Y-plane	0.07	0.98	1.00	0.73	0.29	0.28	0.34	0.96	0.07	0.06	-0.06	-0.32	-0.41	-0.40	0.04	0.07	-0.09	-0.18	-0.16	0.14
Altitude	0.03	0.71	0.73	1.00	0.08	0.36	0.53	0.69	0.25	-0.04	-0.20	-0.43	-0.48	-0.11	0.21	0.25	-0.10	-0.08	-0.08	0.13
Mach	0.18	0.31	0.29	0.08	1.00	0.08	-0.06	0.35	-0.03	0.18	-0.17	-0.07	-0.03	-0.53	-0.13	-0.12	0.02	-0.03	-0.01	0.03
Mach Derivative	-0.02	0.29	0.28	0.36	0.08	1.00	0.71	0.38	0.23	0.43	-0.72	-0.79	-0.62	-0.12	0.47	0.47	0.01	0.48	0.53	0.08
Mach 2nd Derivative	-0.09	0.31	0.34	0.53	-0.06	0.71	1.00	0.40	0.22	0.38	-0.50	-0.84	-0.86	-0.11	0.75	0.76	-0.04	0.59	0.57	0.05
Heading	0.16	0.98	0.96	0.69	0.35	0.38	0.40	1.00	-0.01	0.25	-0.10	-0.38	-0.48	-0.47	0.09	0.12	-0.09	-0.11	-0.10	0.09
Heading derivative	-0.04	0.04	0.07	0.25	-0.03	0.23	0.22	-0.01	1.00	-0.15	-0.28	-0.20	-0.09	0.22	0.33	0.33	0.03	0.35	0.38	0.07
Heading 2nd derivative	0.00	0.09	0.06	-0.04	0.18	0.43	0.38	0.25	-0.15	1.00	-0.31	-0.40	-0.39	-0.21	0.35	0.35	-0.01	0.34	0.33	-0.10
FPA	0.14	-0.05	-0.06	-0.20	-0.17	-0.72	-0.50	-0.10	-0.28	-0.31	1.00	0.70	0.41	-0.06	-0.34	-0.33	-0.05	-0.47	-0.53	-0.11
FPA derivative	0.06	-0.28	-0.32	-0.43	-0.07	-0.79	-0.84	-0.38	-0.20	-0.40	0.70	1.00	0.92	0.18	-0.61	-0.62	0.00	-0.57	-0.57	-0.09
FPA 2nd derivative	0.00	-0.38	-0.41	-0.48	-0.03	-0.62	-0.86	-0.48	-0.09	-0.39	0.41	0.92	1.00	0.28	-0.64	-0.66	0.05	-0.49	-0.45	-0.04
Weight	-0.21	-0.44	-0.40	-0.11	-0.53	-0.12	-0.11	-0.47	0.22	-0.21	-0.06	0.18	0.28	1.00	0.03	0.02	0.02	0.03	0.03	-0.01
Horizontal distance	-0.07	0.01	0.04	0.21	-0.13	0.47	0.75	0.09	0.33	0.35	-0.34	-0.61	-0.64	0.03	1.00	1.00	-0.11	0.81	0.78	-0.02
Straight-line distance	-0.06	0.04	0.07	0.25	-0.12	0.47	0.76	0.12	0.33	0.35	-0.33	-0.62	-0.66	0.02	1.00	1.00	-0.11	0.80	0.76	-0.01
Emission angle	-0.01	-0.09	-0.09	-0.10	0.02	0.01	-0.04	-0.09	0.03	-0.01	-0.05	0.00	0.05	0.02	-0.11	-0.11	1.00	0.10	0.05	0.11
Emission angle squared	0.03	-0.19	-0.18	-0.08	-0.03	0.48	0.59	-0.11	0.35	0.34	-0.47	-0.57	-0.49	0.03	0.81	0.80	0.10	1.00	0.96	0.03
Abs. value of emission angle	0.03	-0.16	-0.16	-0.08	-0.01	0.53	0.57	-0.10	0.38	0.33	-0.53	-0.57	-0.45	0.03	0.78	0.76	0.05	0.96	1.00	0.11
Ambient PL	-0.08	0.11	0.14	0.13	0.03	0.08	0.05	0.09	0.07	-0.10	-0.11	-0.09	-0.04	-0.01	-0.02	-0.01	0.11	0.03	0.11	1.00
Ambient ASEL	-0.08	0.11	0.13	0.13	0.03	0.06	0.03	0.09	0.06	-0.11	-0.09	-0.07	-0.03	-0.02	-0.04	-0.03	0.11	0.01	0.09	1.00
Ambient BSEL	-0.14	0.18	0.21	0.25	0.03	0.17	0.20	0.15	0.18	-0.11	-0.20	-0.22	-0.18	-0.01	0.12	0.13	0.07	0.14	0.20	0.91
Ambient DSEL	-0.04	0.17	0.19	0.19	0.04	0.10	0.10	0.14	0.13	-0.12	-0.13	-0.12	-0.09	-0.01	0.04	0.05	0.09	0.07	0.16	0.97
Ambient ESEL	-0.08	0.14	0.16	0.17	0.03	0.08	0.06	0.11	0.10	-0.11	-0.11	-0.10	-0.06	-0.01	0.00	0.01	0.08	0.04	0.12	0.99
Ambient ISBAP	-0.08	0.18	0.21	0.23	0.03	0.16	0.17	0.15	0.17	-0.11	-0.18	-0.20	-0.15	-0.01	0.11	0.12	0.09	0.13	0.21	0.94
Avg. ambient PL	-0.08	0.04	0.06	0.05	0.08	0.05	-0.01	0.02	0.01	-0.08	-0.11	-0.04	0.01	-0.03	-0.10	-0.09	0.14	-0.01	0.08	0.94
Avg. ambient ASEL	-0.08	0.04	0.06	0.05	0.08	0.03	-0.03	0.02	0.00	-0.09	-0.09	-0.02	0.02	-0.03	-0.11	-0.11	0.14	-0.03	0.06	0.93
Avg. ambient BSEL	-0.18	0.05	0.09	0.11	0.11	0.13	0.11	0.04	0.09	-0.08	-0.21	-0.16	-0.10	-0.03	0.01	0.01	0.13	0.10	0.17	0.89
Avg. ambient DSEL	-0.06	0.06	0.08	0.07	0.11	0.07	0.01	0.04	0.03	-0.08	-0.13	-0.06	-0.01	-0.04	-0.08	-0.07	0.15	0.02	0.11	0.93
Avg. ambient ESEL	-0.09	0.05	0.07	0.06	0.08	0.04	-0.01	0.03	0.02	-0.09	-0.11	-0.04	0.01	-0.03	-0.10	-0.09	0.13	-0.01	0.08	0.94
Avg. ambient ISBAP	-0.10	0.05	0.08	0.08	0.13	0.13	0.08	0.04	0.07	-0.08	-0.20	-0.13	-0.07	-0.04	-0.01	-0.01	0.16	0.09	0.18	0.91
PCBoom PL	0.00	0.06	0.09	-0.02	-0.02	-0.14	-0.35	-0.02	-0.12	-0.43	0.10	0.17	0.22	0.04	-0.78	-0.77	0.31	-0.47	-0.46	0.23
PCBoom ASEL	0.00	0.10	0.13	0.01	0.01	-0.14	-0.37	0.02	-0.10	-0.42	0.10	0.20	0.25	0.03	-0.80	-0.80	0.30	-0.51	-0.49	0.22
PCBoom BSEL	0.00	0.17	0.19	0.06	0.03	-0.11	-0.36	0.09	-0.09	-0.39	0.09	0.20	0.26	0.01	-0.80	-0.80	0.31	-0.52	-0.49	0.21
PCBoom DSEL	0.00	0.14	0.16	0.03	0.01	-0.13	-0.36	0.05	-0.10	-0.41	0.10	0.19	0.24	0.02	-0.80	-0.79	0.31	-0.51	-0.49	0.22
PCBoom ESEL	0.00	0.14	0.16	0.04	0.02	-0.13	-0.37	0.05	-0.10	-0.41	0.10	0.20	0.25	0.02	-0.81	-0.80	0.31	-0.52	-0.49	0.22
PCBoom ISBAP	0.00	0.09	0.11	-0.01	-0.01	-0.13	-0.34	0.00	-0.11	-0.43	0.09	0.16	0.21	0.03	-0.77	-0.77	0.32	-0.47	-0.45	0.24
PCBoom CFD PL	-0.02	0.06	0.09	-0.03	-0.02	-0.06	-0.28	-0.01	-0.11	-0.39	0.03	0.08	0.14	0.01	-0.72	-0.72	0.33	-0.39	-0.38	0.23
PCBoom CFD ASEL	0.00	0.09	0.12	0.00	0.01	-0.07	-0.32	0.02	-0.09	-0.38	0.05	0.12	0.19	0.01	-0.75	-0.75	0.33	-0.43	-0.42	0.22
PCBoom CFD BSEL	0.01	0.16	0.18	0.03	0.03	-0.05	-0.31	0.08	-0.09	-0.35	0.05	0.12	0.19	-0.01	-0.76	-0.75	0.34	-0.44	-0.43	0.21
PCBoom CFD DSEL	0.00	0.12	0.14	0.00	0.01	-0.06	-0.30	0.04	-0.10	-0.37	0.05	0.11	0.17	0.00	-0.75	-0.74	0.34	-0.43	-0.42	0.22
PCBoom CFD ESEL	-0.01	0.12	0.14	0.01	0.01	-0.06	-0.31	0.05	-0.10	-0.37	0.05	0.12	0.19	0.00	-0.76	-0.75	0.34	-0.44	-0.43	0.22
PCBoom CFD ISBAP	-0.01	0.08	0.11	-0.03	-0.02	-0.05	-0.28	0.01	-0.10	-0.38	0.03	0.07	0.14	0.00	-0.71	-0.71	0.34	-0.38	-0.38	0.24
PCBoom Distance	0.02	0.20	0.22	0.19	-0.12	0.08	0.19	0.17	0.34	-0.12	0.02	-0.14	-0.18	0.04	0.31	0.31	-0.11	0.20	0.19	0.10
PCBoom peak pressure	0.06	0.31	0.32	0.20	0.05	-0.08	-0.28	0.21	0.10	-0.43	0.05	0.14	0.19	-0.02	-0.58	-0.57	0.16	-0.37	-0.37	0.27
PCBoom CFD peak pressure	0.06	0.28	0.29	0.17	0.02	-0.01	-0.22	0.19	0.13	-0.40	-0.01	0.06	0.12	0.00	-0.52	-0.51	0.18	-0.28	-0.28	0.27

	Ambient ASEL	Ambient BSEL	Ambient DSEL	Ambient ESEL	Ambient ISBAP	Avg. ambient PL	Avg. ambient ASEL	Avg. ambient BSEL	Avg. ambient DSEL	Avg. ambient ESEL	Avg. ambient ISBAP	PCBoom PL	PCBoom ASEL	PCBoom BSEL	PCBoom DSEL	PCBoom ESEL	PCBoom ISBAP	PCBoom CFD PL	PCBoom CFD ASEL	PCBoom CFD BSEL	PCBoom CFD DSEL	PCBoom CFD ESEL	PCBoom CFD ISBAP	PCBoom Distance	PCBoom peak pressure	PCBoom CFD peak pressure
Flight number	0.14	0.26	0.18	0.17	0.22	0.09	0.09	0.19	0.10	0.10	0.13	-0.03	0.03	0.08	0.04	0.05	-0.02	-0.05	0.00	0.05	0.00	0.01	-0.04	0.14	0.14	0.10
Pass number	0.01	0.00	0.00	0.01	0.00	0.02	0.02	0.03	0.04	0.03	0.04	-0.05	-0.05	-0.03	-0.04	-0.04	-0.04	-0.03	-0.03	0.00	-0.01	-0.01	-0.02	-0.04	-0.01	-0.02
Station number	-0.35	-0.37	-0.35	-0.35	-0.36	-0.33	-0.34	-0.40	-0.36	-0.34	-0.38	-0.42	-0.40	-0.41	-0.41	-0.41	-0.43	-0.46	-0.45	-0.46	-0.46	-0.45	-0.47	-0.06	-0.48	-0.52
Mark time	-0.07	-0.14	-0.04	-0.07	-0.09	-0.09	-0.09	-0.18	-0.06	-0.09	-0.12	-0.10	-0.04	0.01	-0.02	-0.02	-0.08	-0.13	-0.06	-0.01	-0.06	-0.06	-0.12	0.06	0.08	0.06
Wind direction	-0.31	-0.43	-0.33	-0.32	-0.37	-0.26	-0.26	-0.39	-0.27	-0.27	-0.32	-0.11	-0.08	-0.05	-0.07	-0.07	-0.10	-0.14	-0.10	-0.07	-0.09	-0.09	-0.13	-0.10	-0.11	-0.13
Wind speed	0.20	0.22	0.24	0.20	0.24	0.24	0.24	0.29	0.28	0.24	0.30	0.07	0.07	0.08	0.08	0.07	0.08	0.09	0.10	0.11	0.10	0.09	0.09	-0.02	0.09	0.11
Temperature	-0.02	-0.08	0.01	-0.01	-0.04	-0.04	-0.04	-0.13	-0.02	-0.04	-0.08	-0.11	-0.05	0.00	-0.04	-0.03	-0.09	-0.13	-0.06	-0.01	-0.06	-0.05	-0.11	0.08	0.08	0.08
Relative humidity	-0.07	-0.04	-0.09	-0.07	-0.06	-0.04	-0.05	-0.02	-0.08	-0.06	-0.04	-0.06	-0.12	-0.16	-0.13	-0.13	-0.08	-0.04	-0.11	-0.14	-0.10	-0.11	-0.05	-0.06	-0.20	-0.19
Pressure	0.51	0.52	0.52	0.51	0.53	0.50	0.49	0.55	0.53	0.50	0.55	0.21	0.19	0.21	0.21	0.20	0.23	0.27	0.24	0.26	0.26	0.25	0.28	0.09	0.29	0.34
Low alt. wind speed	0.05	0.08	0.01	0.02	0.05	0.10	0.09	0.17	0.09	0.08	0.15	0.20	0.11	0.00	0.06	0.05	0.17	0.23	0.14	0.05	0.12	0.10	0.21	-0.11	-0.09	-0.04
Low alt. wind speed	-0.13	-0.25	-0.16	-0.14	-0.22	-0.11	-0.11	-0.21	-0.12	-0.10	-0.18	-0.15	-0.09	-0.05	-0.08	-0.08	-0.14	-0.18	-0.11	-0.07	-0.11	-0.10	-0.17	-0.03	-0.07	-0.08
Low alt. temperature	0.08	0.16	0.11	0.11	0.14	0.06	0.06	0.13	0.08	0.07	0.10	-0.06	0.01	0.07	0.02	0.03	-0.05	-0.09	-0.02	0.03	-0.02	-0.01	-0.08	0.09	0.07	0.04
Low alt. relative humidity	-0.05	-0.11	-0.08	-0.07	-0.10	-0.02	-0.02	-0.07	-0.04	-0.03	-0.06	0.10	0.03	-0.05	0.01	0.00	0.09	0.13	0.06	0.00	0.05	0.04	0.11	-0.08	-0.05	-0.01
Low alt. pressure	-0.10	-0.18	-0.08	-0.09	-0.13	-0.12	-0.11	-0.21	-0.10	-0.11	-0.16	-0.19	-0.10	-0.01	-0.07	-0.06	-0.16	-0.22	-0.13	-0.05	-0.12	-0.11	-0.20	0.05	0.02	-0.02
Low alt. dew point	-0.03	-0.08	-0.06	-0.05	-0.07	0.00	0.00	-0.03	-0.01	-0.01	-0.02	0.14	0.06	-0.03	0.03	0.02	0.12	0.16	0.09	0.02	0.08	0.06	0.14	-0.07	-0.03	0.02
High alt. wind diretion	-0.12	-0.23	-0.13	-0.15	-0.17	-0.08	-0.08	-0.17	-0.07	-0.10	-0.10	0.03	-0.01	-0.05	-0.02	-0.03	0.03	0.04	0.01	-0.02	0.00	-0.01	0.04	-0.10	-0.08	-0.06
High alt. wind speed	-0.02	-0.05	-0.01	-0.02	-0.03	-0.05	-0.04	-0.10	-0.05	-0.05	-0.08	0.06	0.01	-0.02	0.01	0.01	0.05	0.06	0.03	0.00	0.03	0.03	0.06	0.03	0.08	0.09
High alt. temperature	-0.18	-0.34	-0.21	-0.19	-0.29	-0.16	-0.16	-0.31	-0.17	-0.16	-0.25	-0.17	-0.12	-0.07	-0.10	-0.10	-0.16	-0.20	-0.14	-0.09	-0.13	-0.12	-0.18	-0.04	-0.08	-0.08
High alt. relative humidity	0.18	0.34	0.20	0.20	0.27	0.14	0.14	0.29	0.14	0.15	0.21	0.05	0.07	0.08	0.07	0.07	0.05	0.04	0.06	0.06	0.05	0.06	0.04	0.10	0.09	0.07
High alt. pressure	-0.05	-0.09	-0.06	-0.04	-0.09	-0.07	-0.07	-0.11	-0.06	-0.06	-0.10	-0.19	-0.10	-0.01	-0.07	-0.06	-0.16	-0.22	-0.13	-0.05	-0.12	-0.10	-0.20	0.04	-0.01	-0.05
Hight alt. dew point	0.12	0.23	0.14	0.15	0.18	0.08	0.08	0.18	0.08	0.10	0.12	-0.05	0.00	0.06	0.02	0.03	-0.04	-0.06	-0.02	0.02	-0.02	0.00	-0.06	0.10	0.08	0.04
Planetary boundary layer height	-0.08	-0.17	-0.08	-0.09	-0.12	-0.08	-0.08	-0.16	-0.05	-0.08	-0.10	-0.09	-0.04	0.00	-0.03	-0.03	-0.08	-0.13	-0.06	-0.02	-0.06	-0.06	-0.12	0.01	0.02	0.00
Friction velociy	-0.08	-0.14	-0.04	-0.08	-0.08	-0.08	-0.08	-0.18	-0.06	-0.09	-0.10	0.00	0.00	0.00	0.00	0.00	0.00	-0.02	0.00	0.01	0.00	-0.01	-0.01	0.02	0.06	0.06
X-plane	0.11	0.18	0.17	0.14	0.18	0.04	0.04	0.05	0.06	0.05	0.05	0.06	0.10	0.17	0.14	0.14	0.09	0.06	0.09	0.16	0.12	0.12	0.08	0.20	0.31	0.28
Y-plane	0.13	0.21	0.19	0.16	0.21	0.06	0.06	0.09	0.08	0.07	0.08	0.09	0.13	0.19	0.16	0.16	0.11	0.09	0.12	0.18	0.14	0.14	0.11	0.22	0.32	0.29
Altitude	0.13	0.25	0.19	0.17	0.23	0.05	0.05	0.11	0.07	0.06	0.08	-0.02	0.01	0.06	0.03	0.04	-0.01	-0.03	0.00	0.03	0.00	0.01	-0.03	0.19	0.20	0.17
Mach	0.03	0.03	0.04	0.03	0.03	0.08	0.08	0.11	0.11	0.08	0.13	-0.02	0.01	0.03	0.01	0.02	-0.01	-0.02	0.01	0.03	0.01	0.01	-0.02	-0.12	0.05	0.02
Mach Derivative	0.06	0.17	0.10	0.08	0.16	0.05	0.03	0.13	0.07	0.04	0.13	-0.14	-0.14	-0.11	-0.13	-0.13	-0.13	-0.06	-0.07	-0.05	-0.06	-0.06	-0.05	0.08	-0.08	-0.01
Mach 2nd Derivative	0.03	0.20	0.10	0.06	0.17	-0.01	-0.03	0.11	0.01	-0.01	0.08	-0.35	-0.37	-0.36	-0.36	-0.37	-0.34	-0.28	-0.32	-0.31	-0.30	-0.31	-0.28	0.19	-0.28	-0.22
Heading	0.09	0.15	0.14	0.11	0.15	0.02	0.02	0.04	0.04	0.03	0.04	-0.02	0.02	0.09	0.05	0.05	0.00	-0.01	0.02	0.08	0.04	0.05	0.01	0.17	0.21	0.19
Heading derivative	0.06	0.18	0.13	0.10	0.17	0.01	0.00	0.09	0.03	0.02	0.07	-0.12	-0.10	-0.09	-0.10	-0.10	-0.11	-0.11	-0.09	-0.09	-0.10	-0.10	-0.10	0.34	0.10	0.13
Heading 2nd derivative	-0.11	-0.11	-0.12	-0.11	-0.11	-0.08	-0.09	-0.08	-0.08	-0.09	-0.08	-0.43	-0.42	-0.39	-0.41	-0.41	-0.43	-0.39	-0.38	-0.35	-0.37	-0.37	-0.38	-0.12	-0.43	-0.40
FPA	-0.09	-0.20	-0.13	-0.11	-0.18	-0.11	-0.09	-0.21	-0.13	-0.11	-0.20	0.10	0.10	0.09	0.10	0.10	0.09	0.03	0.05	0.05	0.05	0.05	0.03	0.02	0.05	-0.01
FPA derivative	-0.07	-0.22	-0.12	-0.10	-0.20	-0.04	-0.02	-0.16	-0.06	-0.04	-0.13	0.17	0.20	0.20	0.19	0.20	0.16	0.08	0.12	0.12	0.11	0.12	0.07	-0.14	0.14	0.06
FPA 2nd derivative	-0.03	-0.18	-0.09	-0.06	-0.15	0.01	0.02	-0.10	-0.01	0.01	-0.07	0.22	0.25	0.26	0.24	0.25	0.21	0.14	0.19	0.19	0.17	0.19	0.14	-0.18	0.19	0.12
Weight	-0.02	-0.01	-0.01	-0.01	-0.01	-0.03	-0.03	-0.03	-0.04	-0.03	-0.04	0.04	0.03	0.01	0.02	0.02	0.03	0.01	0.01	-0.01	0.00	0.00	0.00	0.04	-0.02	0.00
Horizontal distance	-0.04	0.12	0.04	0.00	0.11	-0.10	-0.11	0.01	-0.08	-0.10	-0.01	-0.78	-0.80	-0.80	-0.80	-0.81	-0.77	-0.72	-0.75	-0.76	-0.75	-0.76	-0.71	0.31	-0.58	-0.52
Straight-line distance	-0.03	0.13	0.05	0.01	0.12	-0.09	-0.11	0.01	-0.07	-0.09	-0.01	-0.77	-0.80	-0.80	-0.79	-0.80	-0.77	-0.72	-0.75	-0.75	-0.74	-0.75	-0.71	0.31	-0.57	-0.51
Emission angle	0.11	0.07	0.09	0.08	0.09	0.14	0.14	0.13	0.15	0.13	0.16	0.31	0.30	0.31	0.31	0.31	0.32	0.33	0.33	0.34	0.34	0.34	0.34	-0.11	0.16	0.18
Emission angle squared	0.01	0.14	0.07	0.04	0.13	-0.01	-0.03	0.10	0.02	-0.01	0.09	-0.47	-0.51	-0.52	-0.51	-0.52	-0.47	-0.39	-0.43	-0.44	-0.43	-0.44	-0.38	0.20	-0.37	-0.28
Abs. value of emission angle	0.09	0.20	0.16	0.12	0.21	0.08	0.06	0.17	0.11	0.08	0.18	-0.46	-0.49	-0.49	-0.49	-0.49	-0.45	-0.38	-0.42	-0.43	-0.42	-0.43	-0.38	0.19	-0.37	-0.28
Ambient PL	1.00	0.91	0.97	0.99	0.94	0.94	0.93	0.89	0.93	0.94	0.91	0.23	0.22	0.21	0.22	0.22	0.24	0.23	0.22	0.21	0.22	0.22	0.24	0.10	0.27	0.27
Ambient ASEL	1.00	0.90	0.97	0.99	0.93	0.94	0.94	0.89	0.94	0.94	0.91	0.24	0.22	0.22	0.23	0.22	0.25	0.24	0.22	0.22	0.23	0.22	0.24	0.09	0.28	0.28
Ambient BSEL	0.90	1.00	0.96	0.94	0.98	0.78	0.77	0.86	0.80	0.79	0.84	0.21	0.18	0.18	0.19	0.18	0.21	0.22	0.20	0.19	0.20	0.19	0.22	0.23	0.29	0.30
Ambient DSEL	0.97	0.96	1.00	0.99	0.98	0.87	0.87	0.86	0.88	0.88	0.87	0.22	0.21	0.20	0.21	0.21	0.23	0.22	0.21	0.20	0.21	0.21	0.23	0.18	0.30	0.30
Ambient ESEL	0.99	0.94	0.99	1.00	0.95	0.92	0.91	0.88	0.92	0.92	0.90	0.23	0.21	0.21	0.22	0.21	0.23	0.23	0.21	0.21	0.22	0.21	0.23	0.14	0.30	0.29
Ambient ISBAP	0.93	0.98	0.98	0.95	1.00	0.81	0.81	0.85	0.83	0.82	0.86	0.21	0.19	0.19	0.20	0.19	0.22	0.22	0.20	0.19	0.21	0.20	0.22	0.21	0.29	0.29
Avg. ambient PL	0.94	0.78	0.87	0.92	0.81	1.00	1.00	0.94	0.99	1.00	0.97	0.23	0.21	0.21	0.22	0.21	0.24	0.23	0.22	0.21	0.22	0.22	0.24	-0.03	0.22	0.22
Avg. ambient ASEL	0.94	0.77	0.87	0.91	0.81	1.00	1.00	0.93	0.99	1.00	0.96	0.24	0.22	0.22	0.23	0.22	0.24	0.24	0.23	0.22	0.23	0.22	0.24	-0.04	0.23	0.23
Avg. ambient BSEL	0.89	0.86	0.86	0.88	0.85	0.94	0.93	1.00	0.95	0.94	0.98	0.21	0.19	0.17	0.19	0.18	0.21	0.23	0.21	0.19	0.21	0.20	0.23	0.03	0.22	0.24
Avg. ambient DSEL	0.94	0.80	0.88	0.92	0.83	0.99	0.99	0.95	1.00	0.99	0.98	0.23	0.21	0.21	0.22	0.21	0.23	0.24	0.22	0.21	0.23	0.22	0.24	-0.02	0.23	0.24
Avg. ambient ESEL	0.94	0.79	0.88	0.92	0.82	1.00	1.00	0.94	0.99	1.00	0.97	0.23	0.22	0.21	0.22	0.22	0.24	0.24	0.22	0.21	0.23	0.22	0.24	-0.02	0.23	0.23
Avg. ambient ISBAP	0.91	0.84	0.87	0.90	0.86	0.97	0.96	0.98	0.98	0.97	1.00	0.22	0.19	0.18	0.20	0.19	0.22	0.23	0.21	0.20	0.21	0.20	0.23	0.00	0.21	0.23
PCBoom PL	0.24	0.21	0.22	0.23	0.21	0.23	0.24	0.21	0.23	0.23	0.22	1.00	0.99	0.98	0.99	0.99	1.00	0.99	0.99	0.97	0.98	0.98	0.98	-0.09	0.96	0.95
PCBoom ASEL	0.22	0.18	0.21	0.21	0.19	0.21	0.22	0.19	0.21	0.22	0.19	0.99	1.00	0.99	1.00	1.00	0.99	0.97	0.99	0.98	0.98	0.99	0.97	-0.09	0.97	0.96
PCBoom BSEL	0.22	0.18	0.20	0.21	0.19	0.21	0.22	0.17	0.21	0.21	0.18	0.98	0.99	1.00	1.00	1.00	0.98	0.96	0.98	0.99	0.98	0.98	0.96	-0.09	0.98	0.96
PCBoom DSEL	0.23	0.19	0.21	0.22	0.20	0.22	0.23	0.19	0.22	0.22	0.20	0.99	1.00	1.00	1.00	1.00	0.99	0.97	0.98	0.99	0.99	0.99	0.97	-0.09	0.98	0.97
PCBoom ESEL	0.22	0.18	0.21	0.21	0.19	0.21	0.22	0.18	0.21	0.22	0.19	0.99	1.00	1.00	1.00	1.00	0.99	0.97	0.98	0.99	0.98	0.99	0.97	-0.09	0.98	0.96
PCBoom ISBAP	0.25	0.21	0.23	0.23	0.22	0.24	0.24	0.21	0.23	0.24	0.22	1.00	0.99	0.98	0.99	0.99	1.00	0.99	0.99	0.98	0.99	0.99	0.99	-0.09	0.96	0.96
PCBoom CFD PL	0.24	0.22	0.22	0.23	0.22	0.23	0.24	0.23	0.24	0.24	0.23	0.99	0.97	0.96	0.97	0.97	0.99	1.00	0.99	0.98	0.99	0.99	1.00	-0.08	0.93	0.96
PCBoom CFD ASEL	0.22	0.20	0.21	0.21	0.20	0.22	0.23	0.21	0.22	0.22	0.21	0.99	0.99	0.98	0.98	0.98	0.99	0.99	1.00	0.99	1.00	1.00	0.99	-0.07	0.95	0.97
PCBoom CFD BSEL	0.22	0.19	0.20	0.21	0.19	0.21	0.22	0.19	0.21	0.21	0.20	0.97	0.98	0.99	0.99	0.99	0.98	0.98	0.99	1.00	1.00	1.00	0.98	-0.07	0.97	0.98
PCBoom CFD DSEL	0.23	0.20	0.21	0.22	0.21	0.22	0.23	0.21	0.23	0.23	0.21	0.98	0.98	0.98	0.99	0.98	0.99	0.99	1.00	1.00	1.00	1.00	0.99	-0.07	0.96	0.98
PCBoom CFD ESEL	0.22	0.19	0.21	0.21	0.20	0.22	0.22	0.20	0.22	0.22	0.20	0.98	0.99	0.98	0.99	0.99	0.99	0.99	1.00	1.00	1.00	1.00	0.99	-0.07	0.96	0.98
PCBoom CFD ISBAP	0.24	0.22	0.23	0.23	0.22	0.24	0.24	0.23	0.24	0.24	0.23	0.98	0.97	0.96	0.97	0.97	0.99	1.00	0.99	0.98	0.99	0.99	1.00	-0.07	0.94	0.97
PCBoom Distance	0.09	0.23	0.18	0.14	0.21	-0.03	-0.04	0.03	-0.02	-0.02	0.00	-0.09	-0.09	-0.09	-0.09	-0.09	-0.09	-0.08	-0.07	-0.07	-0.07	-0.07	-0.07	1.00	0.23	0.26
PCBoom peak pressure	0.28	0.29	0.30	0.30	0.29	0.22	0.23	0.22	0.23	0.23	0.21	0.96	0.97	0.98	0.98	0.98	0.96	0.93	0.95	0.97	0.96	0.96	0.94	0.23	1.00	0.98
PCBoom CFD peak pressure	0.28	0.30	0.30	0.29	0.29	0.22	0.23	0.24	0.24	0.23	0.23	0.95	0.96	0.96	0.97	0.96	0.96	0.96	0.97	0.98	0.98	0.98	0.97	0.26	0.98	1.00

Table C.4. Lasso Regression inputs for QSF18.

#	Input name	Description
1	Time values	Time of day boom the was generated.
2	Aircraft	Two aircraft were used at QSF18.
3	Tower humidity	Relative humidity as measured by a ground weather station (tower).
4	Tower pressure	Pressure as measured by a ground weather station (tower).
5	Tower temperature	Temperature as measured by a ground weather station (tower).
6	Tower Wind Direction	Sine of wind direction as measured by a ground weather station (tower).
7	Tower Wind Direction 2	Cosine of wind direction as measured by a ground weather station (tower).
8	Tower Wind Speed	Pressure as measured by a ground weather station (tower).
9	Low altitude humidity	Relative humidity as measured by weather balloon at 2,000 ft.
10	Low altitude pressure	Atmospheric pressure as measured by weather balloon at 2,000 ft.
11	Low altitude temperature	Temperature as measured by weather balloon at 2,000 ft.
12	Low altitude wind direction	Sine of wind direction as measured by weather balloon at 2,000 ft.
13	Low altitude wind direction 2	Cosine of wind direction as measured by weather balloon at 2,000 ft.
14	Low wind speed	Wind speed as measured by weather balloon at 2,000 ft.
15	High altitude humidity	Relative humidity as measured by weather balloon at 30,000 ft.
16	High altitude pressure	Atmospheric pressure as measured by weather balloon at 30,000 ft.
17	High altitude temperature	Temperature as measured by weather balloon at 30,000 ft.
18	High altitude wind direction	Sine of wind direction as measured by weather balloon at 30,000 ft.
19	High altitude wind direction 2	Cosine of wind direction as measured by weather balloon at 30,000 ft.
20	High wind speed	Wind speed as measured by weather balloon at 30,000 ft.

21	Atmospheric boundary layer height	Atmospheric boundary layer height as modeled by CFSv2.
22	Friction velocity	Friction velocity from CFSv2 modeled data.
23	Exchange coefficient	Exchange coefficient from CFSv2 modeled data.
24	Latent heat flux	Latent heat flux from CFSv2 modeled data.
25	Sensible heat flux	Sensible heat flux from CFSv2 modeled data.
26	Temperature gradient	Change in temperature from ground to 30,000 ft.
27	Aircraft weight	Average weight of the aircraft during dive maneuver.
28	Aircraft altitude	Average altitude of the aircraft during dive maneuver.
29	Heading	Heading (horizontal angle) of the aircraft at time of ray emission.
30	Dive depth	Difference in altitude from start of dive to end of dive.
31	Dive slope	Dive depth divided by the time it took to complete the dive.
32	Average Mach	Average Mach number of the aircraft during the dive maneuver.
33	Ambient PL	Ambient noise Perceived Level (PL) in the 650 ms immediately preceding the boom.
34	Angle	Difference in angle between aircraft heading and angle to the microphone station.
35	Station Distance	Horizontal distance of the aircraft to the microphone station.

Table C.5. Lasso regression outputs for QSF18.

#	**Output name**	**Description**
1	PL	Measured PL
2	ASEL	Measured ASEL
3	BSEL	Measured BSEL
4	DSEL	Measured DSEL
5	ESEL	Measured ESEL
6	ISBAP	Measured ISBAP
7	Rise time	Measured 10-90 rise time
8	Max Pascals	Measured maximum overpressure
9	OASPL	Measured Overall Sound Pressure Level
10	CSEL	Measured CSEL
11	ZSEL	Measured ZSEL

Table C.6. Correlations for QSF18 inputs used in Lasso regression. Positive correlations are shown in blue and negative correlations are shown in red.

	TimeVals	Aircraft	TowerHum	TowerPres	TowerTem	TowerWin	TowerWin	TowerWin	LowAltHur	LowAltPre	LowAltTen	LowAltWir	LowAltWir	LowAltWir	HighAltHur	HighAltPre	HighAltTer	HighAltWir	HighAltWir	HighAltWir	ABLHeight	FrictionVel	ExchangeC	LatentHea	SensibleHe	TempGrad	AircraftWe	AircraftAlt	Heading	DiveDepth	DiveSlope	AvgMach	AmbientPL	Angle	StationDist
TimeVals	1.00	0.25	-0.18	-0.01	-0.11	-0.10	0.31	0.38	0.16	0.02	-0.24	0.02	0.18	0.06	0.33	-0.22	-0.03	0.30	-0.33	0.31	0.13	0.34	0.33	0.28	0.46	-0.13	0.00	0.07	0.23	0.02	-0.34	-0.18	0.18	0.29	-0.15
Aircraft	0.25	1.00	-0.03	-0.03	-0.01	0.14	-0.12	-0.05	-0.09	0.01	-0.06	0.17	0.09	0.12	0.03	-0.01	-0.04	-0.12	0.07	-0.01	0.07	0.01	0.03	0.05	0.05	-0.01	-0.24	-0.10	0.12	-0.20	0.07	0.15	0.00	0.10	0.14
TowerHum	-0.18	-0.03	1.00	-0.73	0.66	0.20	-0.27	0.25	0.81	-0.72	0.73	0.27	-0.74	0.16	-0.68	0.79	0.67	-0.53	0.55	-0.69	-0.72	-0.36	-0.48	-0.60	-0.63	0.65	0.10	0.64	0.09	-0.18	-0.05	-0.16	0.10	0.31	-0.18
TowerPres	-0.01	-0.03	-0.73	1.00	-0.97	-0.11	0.59	-0.07	-0.56	0.99	-0.97	0.06	0.96	-0.13	0.73	-0.84	-0.87	0.64	-0.61	0.82	0.75	0.67	0.77	0.89	0.84	-0.97	-0.05	-0.63	-0.20	-0.02	0.10	0.00	-0.05	-0.07	-0.12
TowerTem	-0.11	-0.01	0.66	-0.97	1.00	0.11	-0.65	-0.04	0.47	-0.95	0.98	-0.13	-0.95	0.03	-0.73	0.85	0.90	-0.66	0.63	-0.83	-0.77	-0.73	-0.83	-0.91	-0.87	1.00	0.02	0.57	0.18	0.02	-0.03	0.02	0.01	0.01	0.20
TowerWin	-0.10	0.14	0.20	-0.11	0.11	1.00	0.17	-0.09	0.09	-0.11	0.16	0.60	-0.14	-0.19	-0.23	0.37	0.18	-0.55	0.54	-0.29	-0.30	-0.12	-0.13	-0.10	-0.25	0.10	-0.04	-0.04	-0.39	-0.16	0.43	0.21	0.10	-0.19	-0.20
TowerWin	0.31	-0.12	-0.27	0.59	-0.65	0.17	1.00	0.41	0.08	0.57	-0.62	0.45	0.49	-0.08	0.54	-0.42	-0.42	0.43	-0.42	0.62	0.34	0.68	0.70	0.69	0.67	-0.67	0.09	-0.23	-0.42	-0.01	-0.02	-0.11	0.11	0.02	-0.51
TowerWin	0.38	-0.05	0.25	-0.07	-0.04	-0.09	0.41	1.00	0.53	-0.10	-0.06	0.22	-0.09	0.42	0.10	0.01	0.12	0.29	-0.34	0.16	0.06	0.42	0.34	0.20	0.25	-0.07	0.06	0.37	0.09	0.03	-0.44	-0.33	0.22	0.20	-0.52
LowAltHur	0.16	-0.09	0.81	-0.56	0.47	0.09	0.08	0.53	1.00	-0.58	0.49	0.44	-0.59	0.33	-0.35	0.64	0.62	-0.25	0.17	-0.37	-0.49	0.06	-0.08	-0.26	-0.26	0.44	0.12	0.67	0.05	-0.05	-0.29	-0.19	0.20	0.37	-0.35
LowAltPre	0.02	0.01	-0.72	0.99	-0.95	-0.11	0.57	-0.10	-0.58	1.00	-0.95	-0.01	0.94	-0.26	0.68	-0.82	-0.84	0.63	-0.57	0.81	0.70	0.63	0.73	0.87	0.82	-0.95	-0.07	-0.67	-0.14	-0.04	0.16	0.00	-0.09	-0.02	-0.11
LowAltTen	-0.24	-0.06	0.73	-0.97	0.98	0.16	-0.62	-0.06	0.49	-0.95	1.00	-0.05	-0.96	0.06	-0.69	0.85	0.85	-0.69	0.67	-0.85	-0.81	-0.77	-0.86	-0.94	-0.91	0.99	0.04	0.59	0.06	0.02	-0.02	0.04	0.02	-0.04	0.14
LowAltWir	0.02	0.17	0.27	0.06	-0.13	0.60	0.45	0.22	0.44	-0.01	-0.05	1.00	-0.06	0.23	-0.05	0.30	0.07	-0.34	0.21	-0.08	-0.03	0.35	0.31	0.23	0.04	-0.16	0.01	0.06	-0.39	-0.16	0.15	0.12	0.10	0.01	-0.36
LowAltWir	0.18	0.09	-0.74	0.96	-0.95	-0.14	0.49	-0.09	-0.59	0.94	-0.96	-0.06	1.00	-0.11	0.59	-0.80	-0.82	0.59	-0.55	0.74	0.79	0.68	0.77	0.88	0.83	-0.95	-0.05	-0.62	0.01	-0.05	0.10	0.02	-0.05	0.03	-0.06
LowAltWir	0.06	0.12	0.16	-0.13	0.03	-0.19	-0.08	0.42	0.33	-0.26	0.06	0.23	-0.11	1.00	-0.11	0.11	0.06	-0.01	-0.21	-0.13	0.34	0.36	0.28	0.07	-0.04	0.03	0.08	0.33	0.21	0.09	-0.33	0.07	0.20	0.09	-0.03
HighAltHur	0.33	0.03	-0.68	0.73	-0.73	-0.23	0.54	0.10	-0.35	0.68	-0.69	-0.05	0.59	-0.11	1.00	-0.78	-0.70	0.69	-0.71	0.82	0.51	0.44	0.56	0.60	0.75	-0.73	0.05	-0.32	-0.17	0.12	-0.21	-0.01	0.04	0.00	-0.21
HighAltPre	-0.22	-0.01	0.79	-0.84	0.85	0.37	-0.42	0.01	0.64	-0.82	0.85	0.30	-0.80	0.11	-0.78	1.00	0.88	-0.83	0.77	-0.89	-0.73	-0.48	-0.62	-0.69	-0.81	0.83	0.05	0.53	0.06	-0.07	0.07	0.08	0.05	0.07	0.04
HighAltTer	-0.03	-0.04	0.67	-0.87	0.90	0.18	-0.42	0.12	0.62	-0.84	0.85	0.07	-0.82	0.06	-0.70	0.88	1.00	-0.56	0.50	-0.71	-0.70	-0.45	-0.58	-0.67	-0.68	0.88	0.04	0.60	0.13	0.01	-0.11	-0.09	0.05	0.05	0.11
HighAltWir	0.30	-0.12	-0.53	0.64	-0.66	-0.55	0.43	0.29	-0.25	0.63	-0.69	-0.34	0.59	-0.01	0.69	-0.83	-0.56	1.00	-0.95	0.90	0.59	0.58	0.64	0.65	0.83	-0.66	-0.02	-0.25	0.06	0.16	-0.36	-0.30	0.01	0.09	-0.11
HighAltWir	-0.33	0.07	0.55	-0.61	0.63	0.54	-0.42	-0.34	0.17	-0.57	0.67	0.21	-0.55	-0.21	-0.71	0.77	0.50	-0.95	1.00	-0.86	-0.67	-0.67	-0.72	-0.68	-0.82	0.64	0.00	0.18	-0.10	-0.22	0.43	0.21	-0.05	-0.08	0.11
HighAltWir	0.31	-0.01	-0.69	0.82	-0.83	-0.29	0.62	0.16	-0.37	0.81	-0.85	-0.08	0.74	-0.13	0.82	-0.89	-0.71	0.90	-0.86	1.00	0.65	0.66	0.75	0.79	0.92	-0.83	-0.04	-0.47	-0.15	0.06	-0.10	-0.17	-0.02	0.01	-0.19
ABLHeight	0.13	0.07	-0.72	0.75	-0.77	-0.30	0.34	0.06	-0.49	0.70	-0.81	-0.03	0.79	0.34	0.51	-0.73	-0.70	0.59	-0.67	0.65	1.00	0.73	0.79	0.77	0.67	-0.76	0.00	-0.48	-0.02	0.11	-0.06	0.12	-0.03	-0.14	0.00
FrictionVel	0.34	0.01	-0.36	0.67	-0.73	-0.12	0.68	0.42	0.06	0.63	-0.77	0.35	0.68	0.36	0.44	-0.48	-0.45	0.58	-0.67	0.66	0.73	1.00	0.98	0.92	0.81	-0.76	0.05	-0.21	-0.03	-0.05	-0.14	-0.15	0.11	0.17	-0.29
ExchangeC	0.33	0.03	-0.48	0.77	-0.83	-0.13	0.70	0.34	-0.08	0.73	-0.86	0.31	0.77	0.28	0.56	-0.62	-0.58	0.64	-0.72	0.75	0.79	0.98	1.00	0.96	0.87	-0.85	0.02	-0.31	-0.07	-0.02	-0.11	-0.11	0.08	0.12	-0.28
LatentHea	0.28	0.05	-0.60	0.89	-0.91	-0.10	0.69	0.20	-0.26	0.87	-0.94	0.23	0.88	0.07	0.60	-0.69	-0.67	0.65	-0.68	0.79	0.77	0.92	0.96	1.00	0.92	-0.93	-0.03	-0.46	-0.06	-0.05	-0.02	-0.11	0.03	0.10	-0.21
SensibleHe	0.46	0.05	-0.63	0.84	-0.87	-0.25	0.67	0.25	-0.26	0.82	-0.91	0.04	0.83	-0.04	0.75	-0.81	-0.68	0.83	-0.82	0.92	0.67	0.81	0.87	0.92	1.00	-0.89	-0.04	-0.40	0.02	-0.01	-0.16	-0.22	0.04	0.17	-0.21
TempGrad	-0.13	-0.01	0.65	-0.97	1.00	0.10	-0.67	-0.07	0.44	-0.95	0.99	-0.16	-0.95	0.03	-0.73	0.83	0.88	-0.66	0.64	-0.83	-0.76	-0.76	-0.85	-0.93	-0.89	1.00	0.02	0.56	0.18	0.03	-0.02	0.04	0.00	0.00	0.22
AircraftWe	0.00	-0.24	0.10	-0.05	0.02	-0.04	0.09	0.06	0.12	-0.07	0.04	0.01	-0.05	0.08	0.05	0.05	0.04	-0.02	0.00	-0.04	0.00	0.05	0.02	-0.03	-0.04	0.02	1.00	0.14	0.02	-0.04	-0.16	0.05	0.03	0.07	0.05
AircraftAlt	0.07	-0.10	0.64	-0.63	0.57	-0.04	-0.23	0.37	0.67	-0.67	0.59	0.06	-0.62	0.33	-0.32	0.53	0.60	-0.25	0.18	-0.47	-0.48	-0.21	-0.31	-0.46	-0.40	0.56	0.14	1.00	0.12	-0.19	-0.47	-0.27	0.20	0.16	-0.04
Heading	0.23	0.12	0.09	-0.20	0.18	-0.39	-0.42	0.09	0.05	-0.14	0.06	-0.39	0.01	0.21	-0.17	0.06	0.13	0.06	-0.10	-0.15	-0.02	-0.03	-0.07	-0.06	0.02	0.18	0.02	0.12	1.00	0.14	-0.36	-0.13	0.10	0.56	0.25
DiveDepth	0.02	-0.20	-0.18	-0.02	0.02	-0.16	-0.01	0.03	-0.05	-0.04	0.02	-0.16	-0.05	0.09	0.12	-0.07	0.01	0.16	-0.22	0.06	0.11	-0.05	-0.02	-0.05	-0.01	0.03	-0.04	-0.19	0.14	1.00	-0.43	0.45	-0.01	-0.05	-0.02
DiveSlope	-0.34	0.07	-0.05	0.10	-0.03	0.43	-0.02	-0.44	-0.29	0.16	-0.02	0.15	0.10	-0.33	-0.21	0.07	-0.11	-0.36	0.43	-0.10	-0.06	-0.14	-0.11	-0.02	-0.16	-0.02	-0.16	-0.47	-0.36	-0.43	1.00	0.08	-0.15	-0.27	0.02
AvgMach	-0.18	0.15	-0.16	0.00	0.02	0.21	-0.11	-0.33	-0.19	0.00	0.04	0.12	0.02	0.07	-0.01	0.08	-0.09	-0.30	0.21	-0.17	0.12	-0.15	-0.11	-0.11	-0.22	0.04	0.05	-0.27	-0.13	0.45	0.08	1.00	-0.07	-0.21	0.03
AmbientPL	0.18	0.00	0.10	-0.05	0.01	0.10	0.11	0.22	0.20	-0.09	0.02	0.10	-0.05	0.20	0.04	0.05	0.05	0.01	-0.05	-0.02	-0.03	0.11	0.08	0.03	0.04	0.00	0.03	0.20	0.10	-0.01	-0.15	-0.07	1.00	0.06	-0.15
Angle	0.29	0.10	0.31	-0.07	0.01	-0.19	0.02	0.20	0.37	-0.02	-0.04	0.01	0.03	0.09	0.00	0.07	0.05	0.09	-0.08	0.01	-0.14	0.17	0.12	0.10	0.17	0.00	0.07	0.16	0.56	-0.05	-0.27	-0.21	0.06	1.00	0.02
StationDist	-0.15	0.14	-0.18	-0.12	0.20	-0.20	-0.51	-0.52	-0.35	-0.11	0.14	-0.36	-0.06	-0.03	-0.21	0.04	0.11	-0.11	0.11	-0.19	0.00	-0.29	-0.28	-0.21	-0.21	0.22	0.05	-0.04	0.25	-0.02	0.02	0.03	-0.15	0.02	1.00

Appendix D – Additional Microphone Configuration Characterization

This appendix is designed to store the other useful data collected during the laboratory testing discussed in Section 3.2.1 above. Here, more detail is shown so that further conclusions can be drawn in the future.

D.1. Additional COUGAR Testing

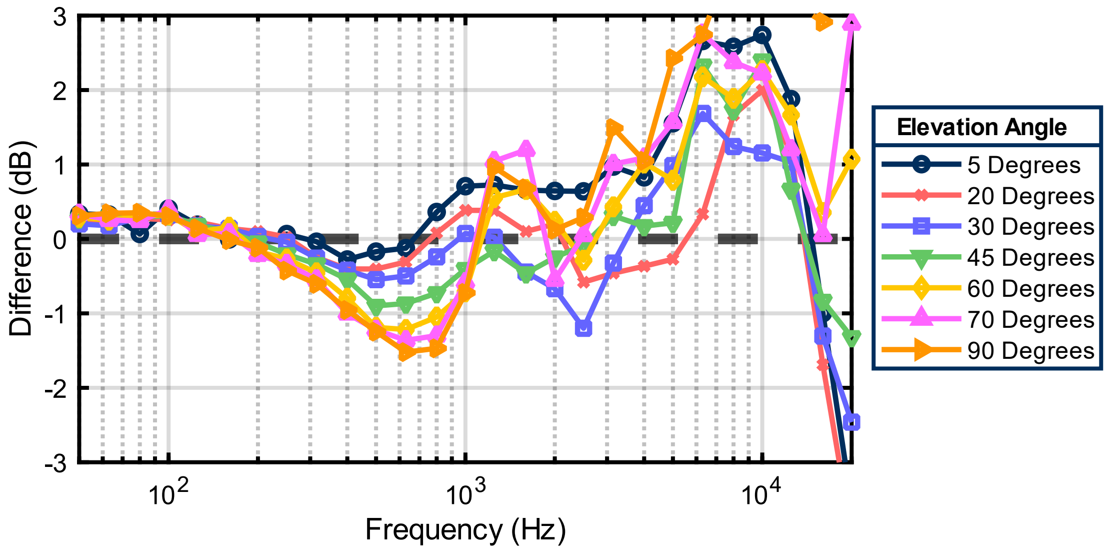

Figure D.1. Effects of inverting the microphone over the ground plate without a windscreen, shown relative to the baseline. These curves represent the plate effects.

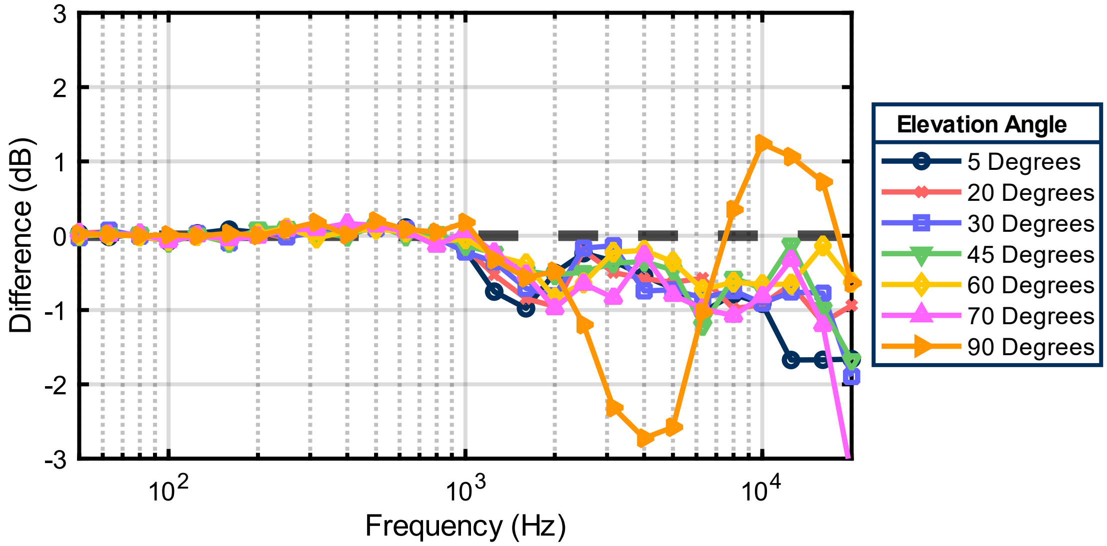

Figure D.2. Effects of placing the windscreen over the inverted microphone, shown relative to the baseline. These curves represent the negative of the windscreen insertion loss.

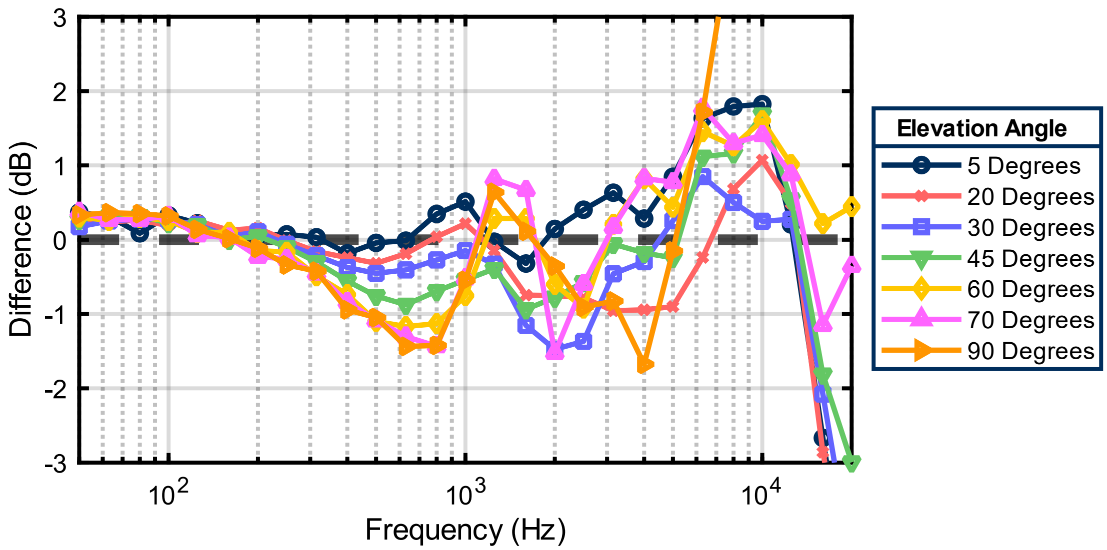

Figure D.3. The completed COUGAR configuration, shown relative to the baseline. These curves represent the cumulative effects of both the plate and the windscreen and both effects are still visible.

D.2. Additional COUGARxt Testing

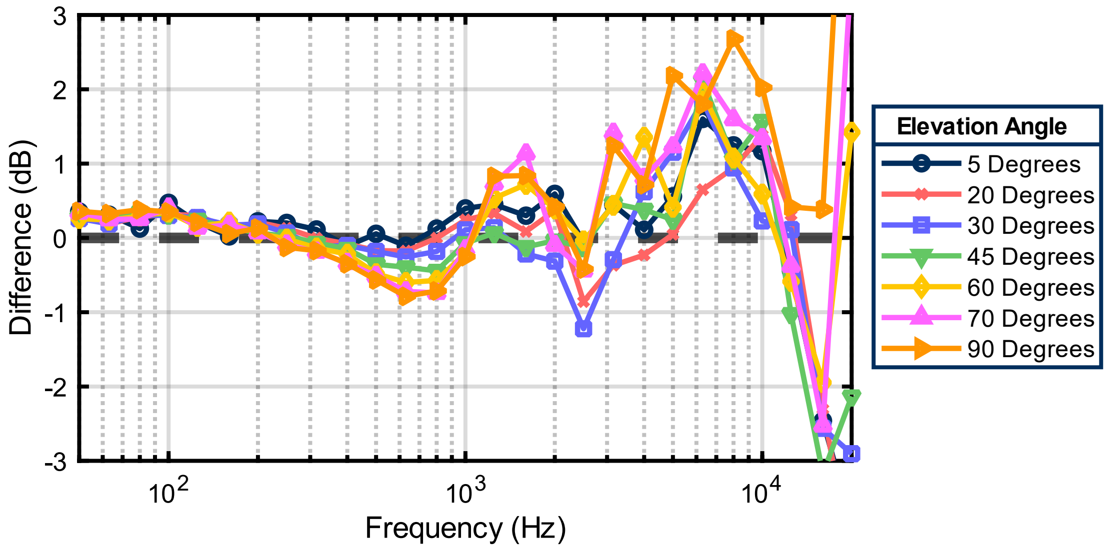

Figure D.4. Effects of inverting the microphone over the ground plate without a windscreen, shown relative to the baseline. These curves represent the plate effects.

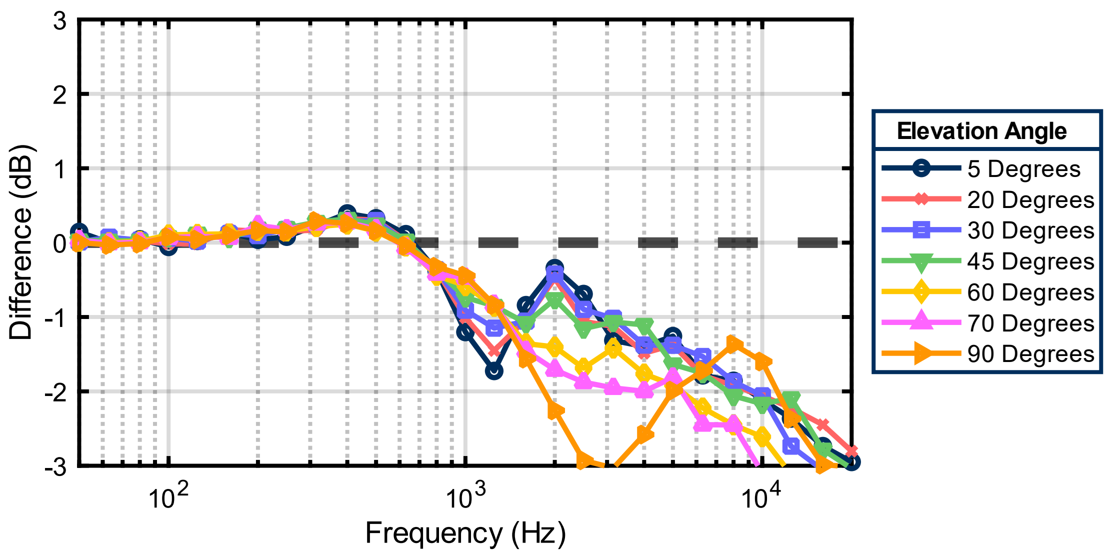

Figure D.5. Effects of placing the windscreen over the inverted microphone, shown relative to the baseline. These curves represent the negative of the windscreen insertion loss.

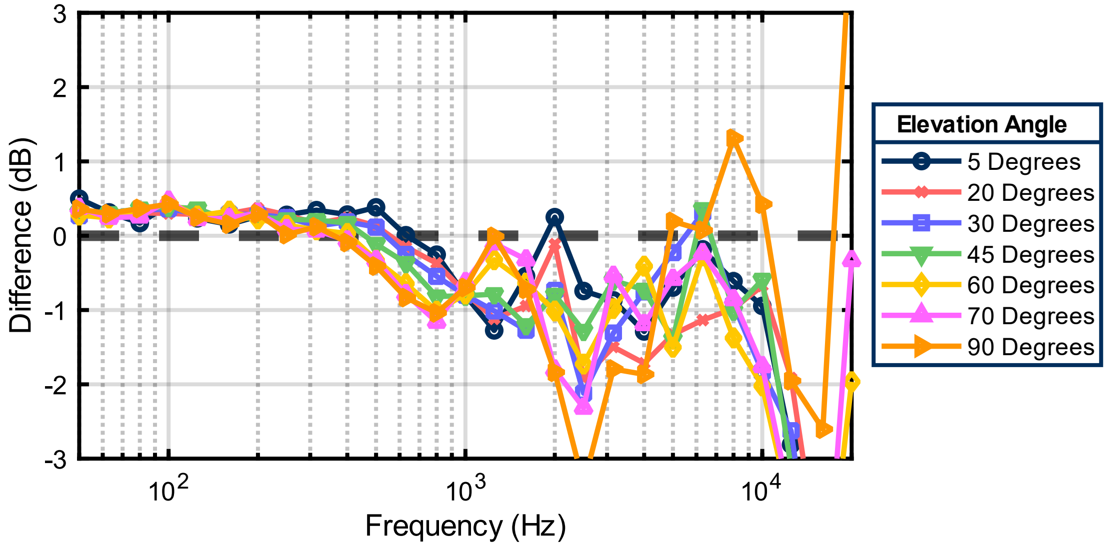

Figure D.6. The completed COUGARxt configuration, shown relative to the baseline. These curves represent the cumulative effects of both the plate and the windscreen and both effects are still visible.

D.3. Additional COUGAR-cub Testing

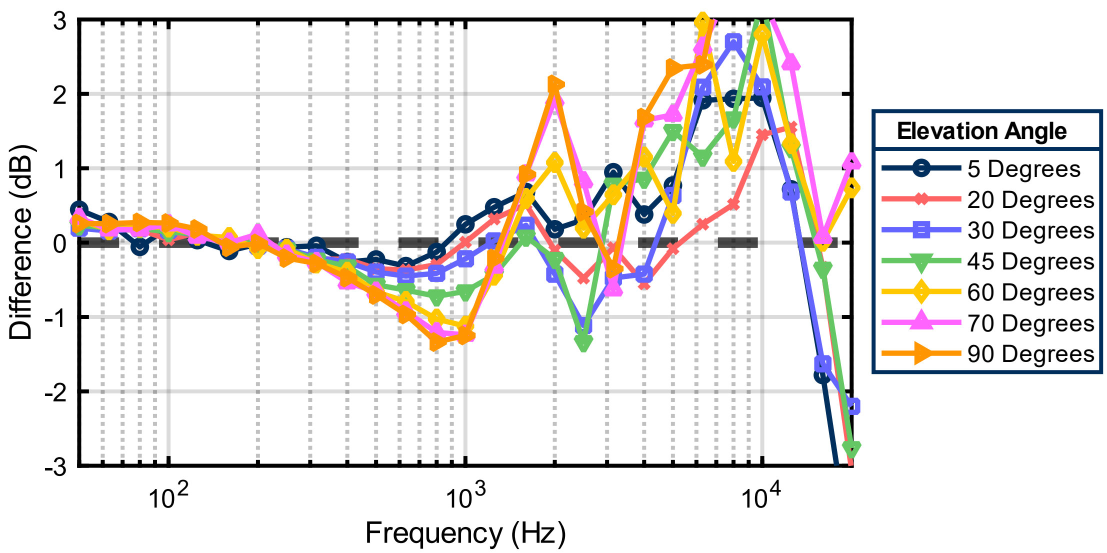

Figure D.7. Effects of inverting the microphone over the ground plate without a windscreen, shown relative to the baseline. These curves represent the plate effects.

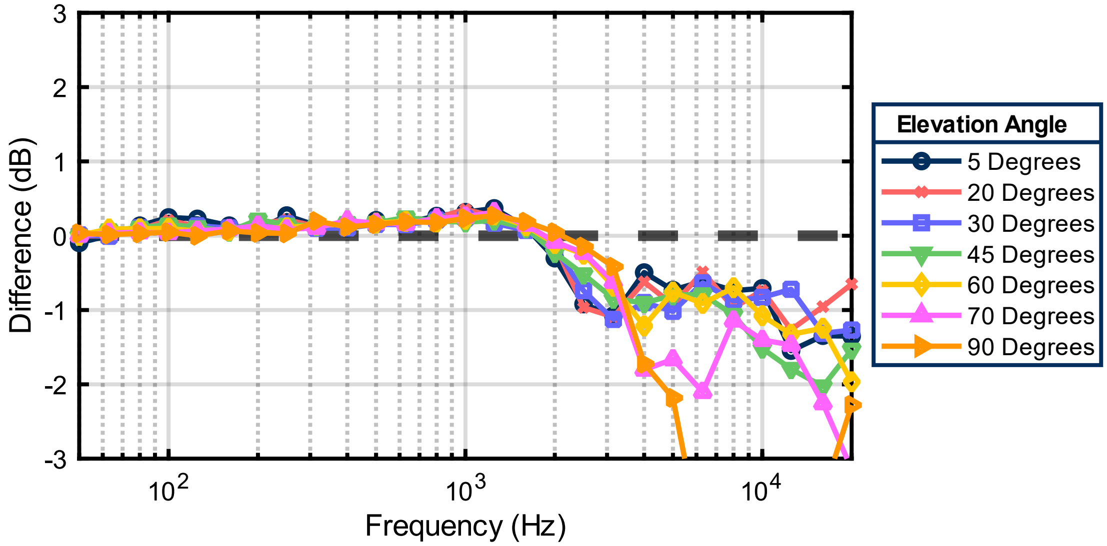

Figure D.8. Effects of placing the windscreen over the inverted microphone, shown relative to the baseline. These curves represent the negative of the windscreen insertion loss.

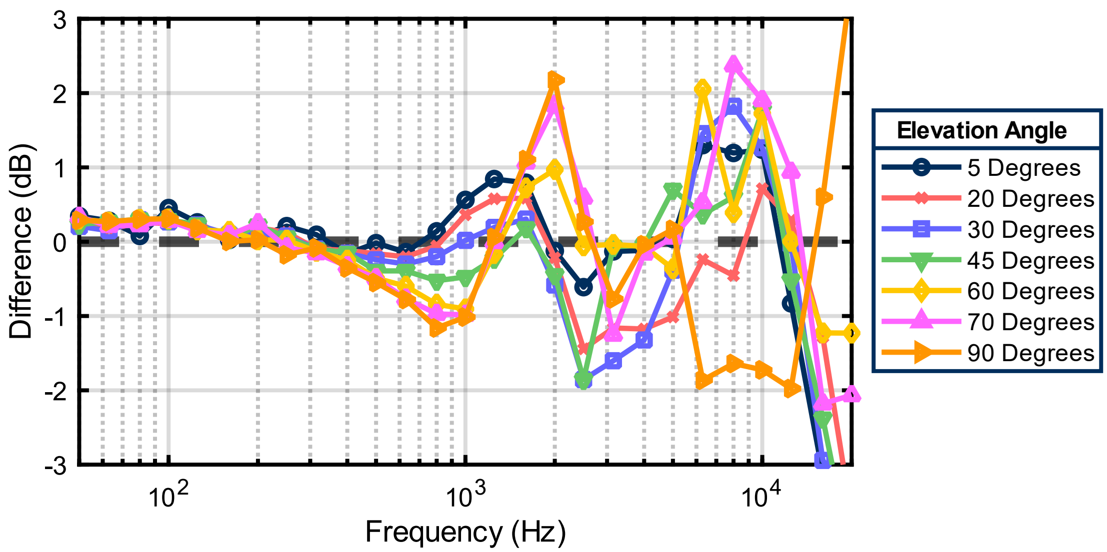

Figure D.9. The completed COUGAR-cub configuration, shown relative to the baseline. These curves represent the cumulative effects of both the plate and the windscreen and both effects are still visible.

D.4. Additional Azimuthal Variability Testing

Here is the complete set of graphs for the elevation and azimuthal angle analyses discussed in Section 3.2.1.3 above.

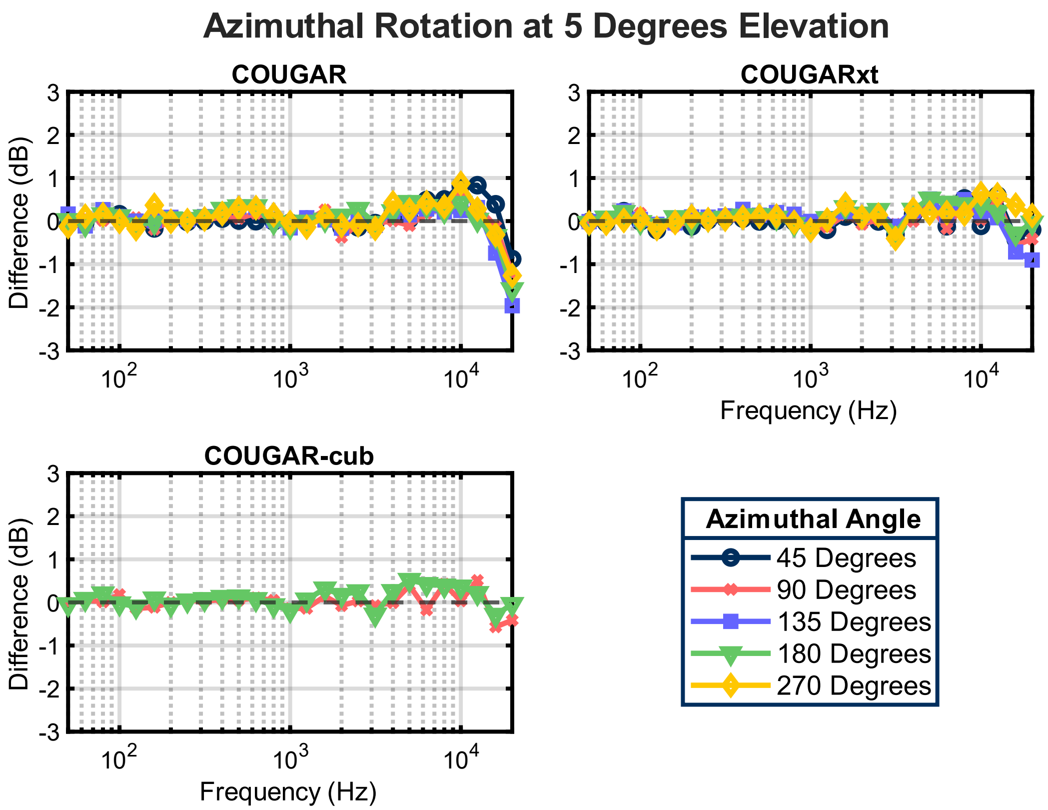

Figure D.10. Dependence of COUGAR, COUGARxt, and COUGAR-cub on azimuthal angle, relative to 0°, for 5° elevation. The COUGAR-cub was only tested on the orientations of 90 and 180°.

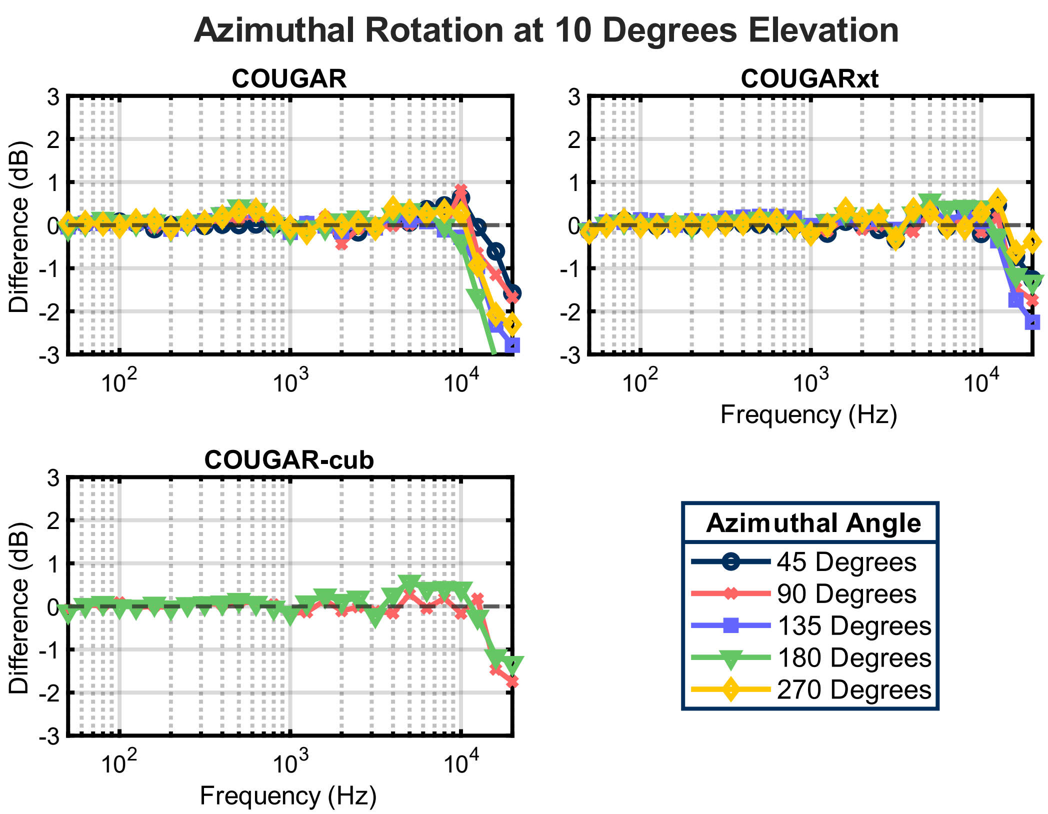

Figure D.11. Same as Figure 5.10, but for 10° elevation.

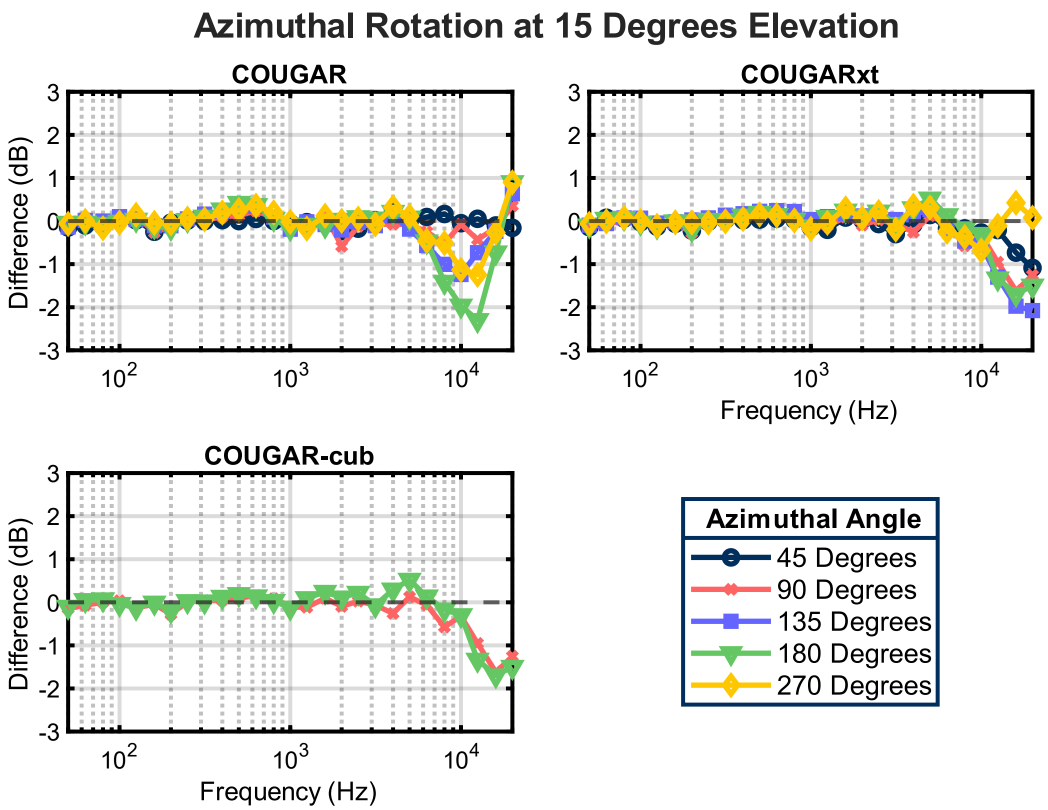

Figure D.12. Same as Figure 5.10, but for 15° elevation.

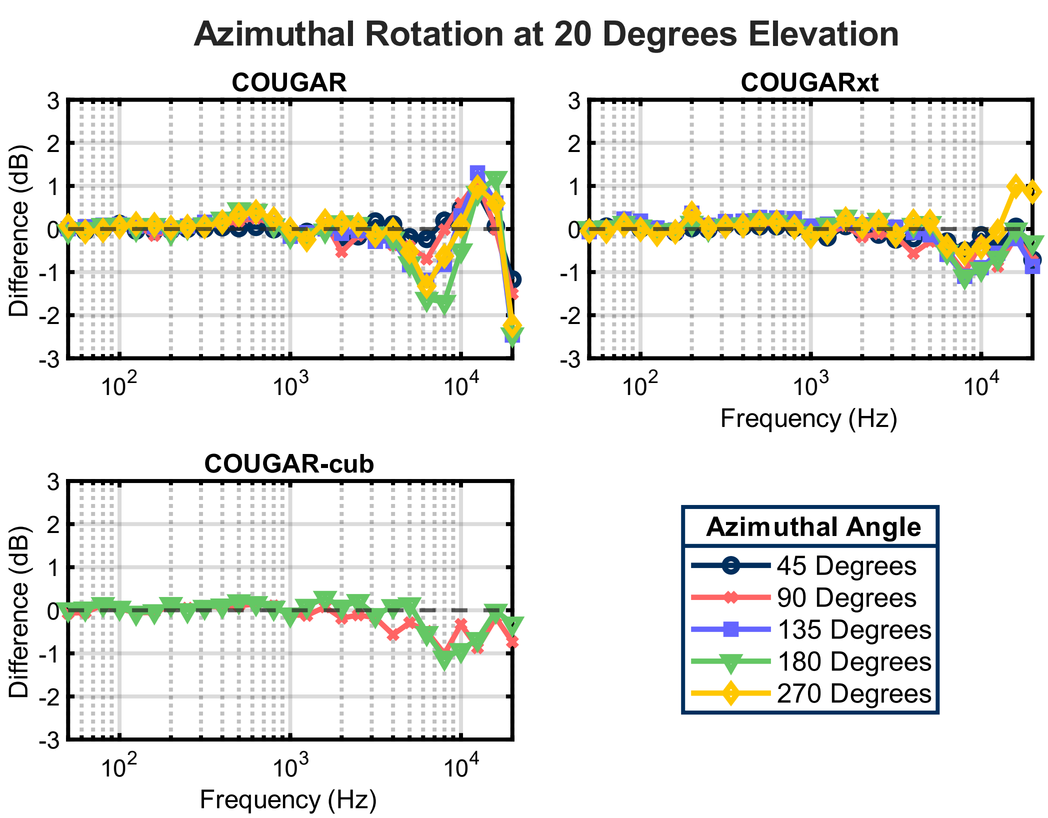

Figure D.13. Same as Figure 5.10, but for 15° elevation.

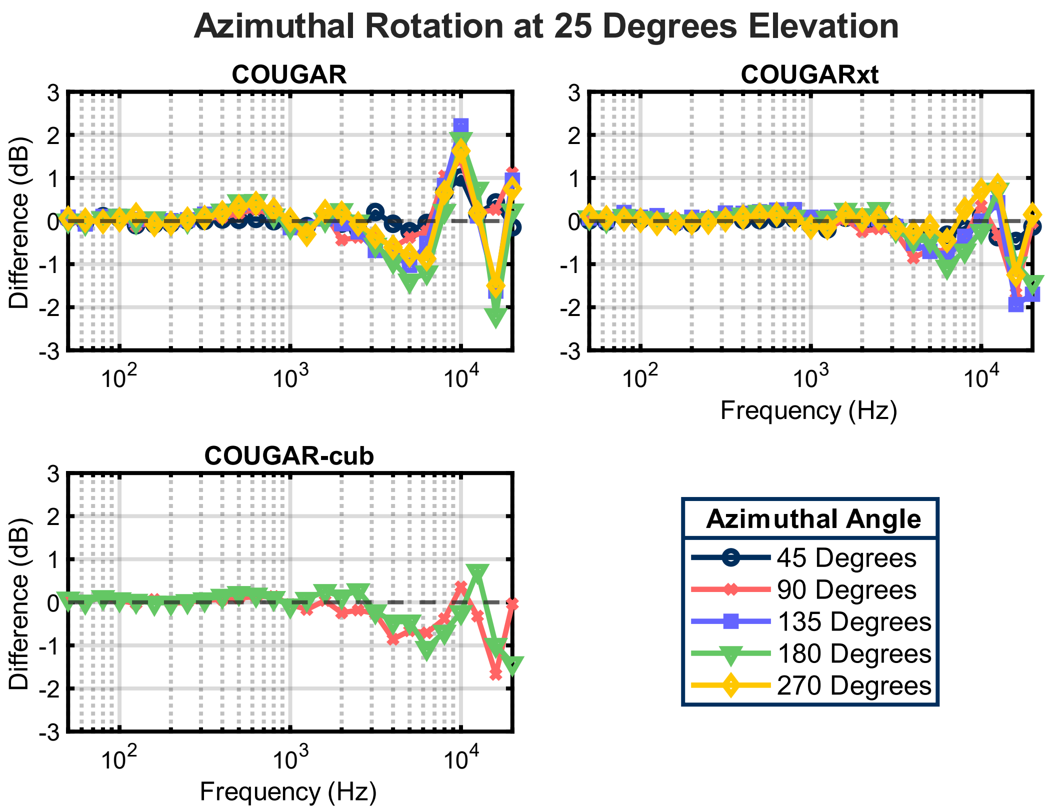

Figure D.14. Same as Figure 5.10, but for 25° elevation.

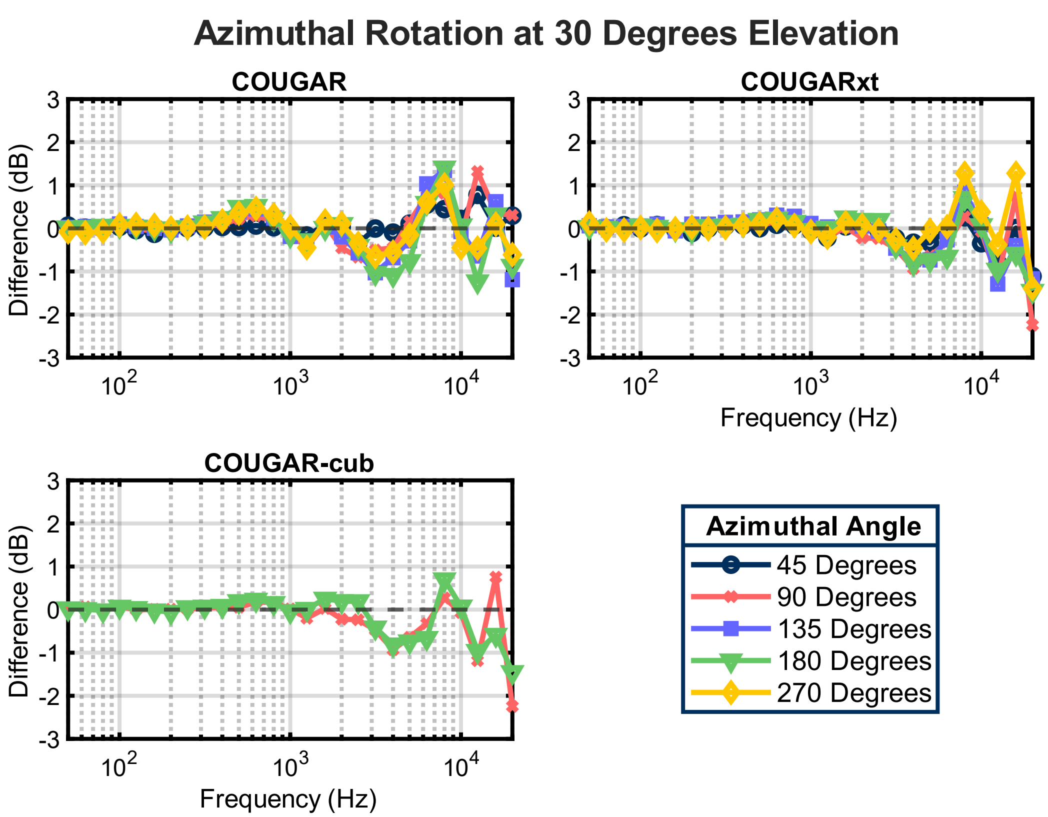

Figure D.15. Same as Figure 5.10, but for 30° elevation.

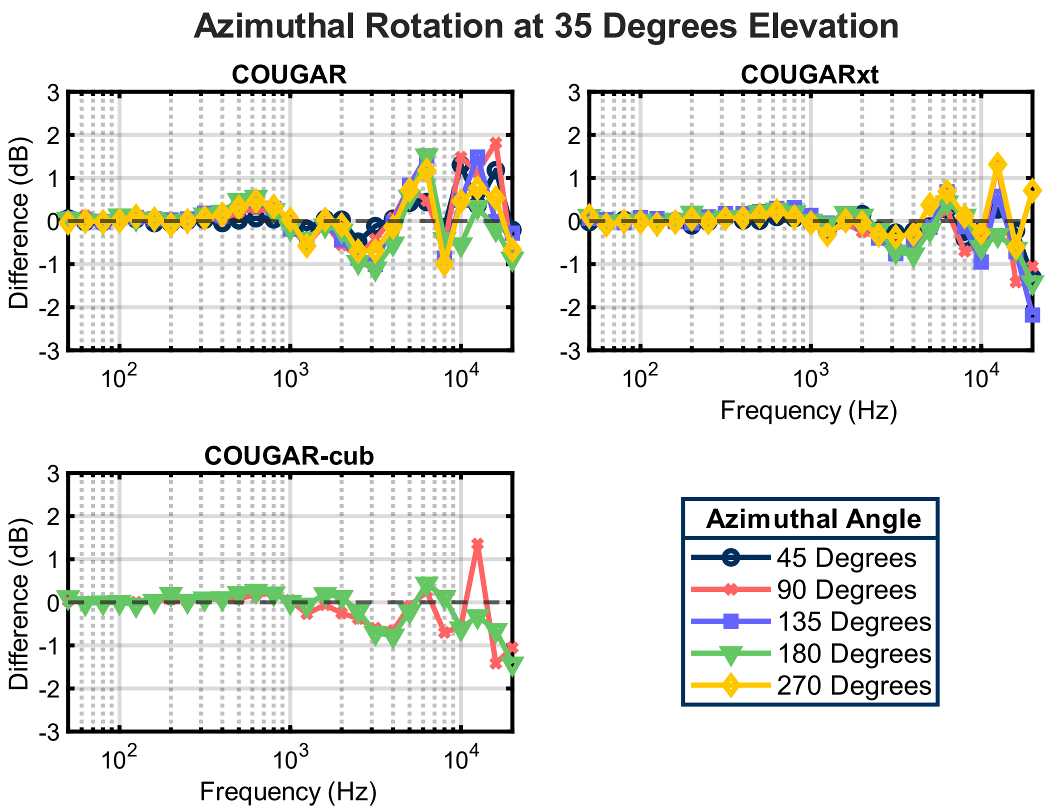

Figure D.16. Same as Figure 5.10, but for 35° elevation.

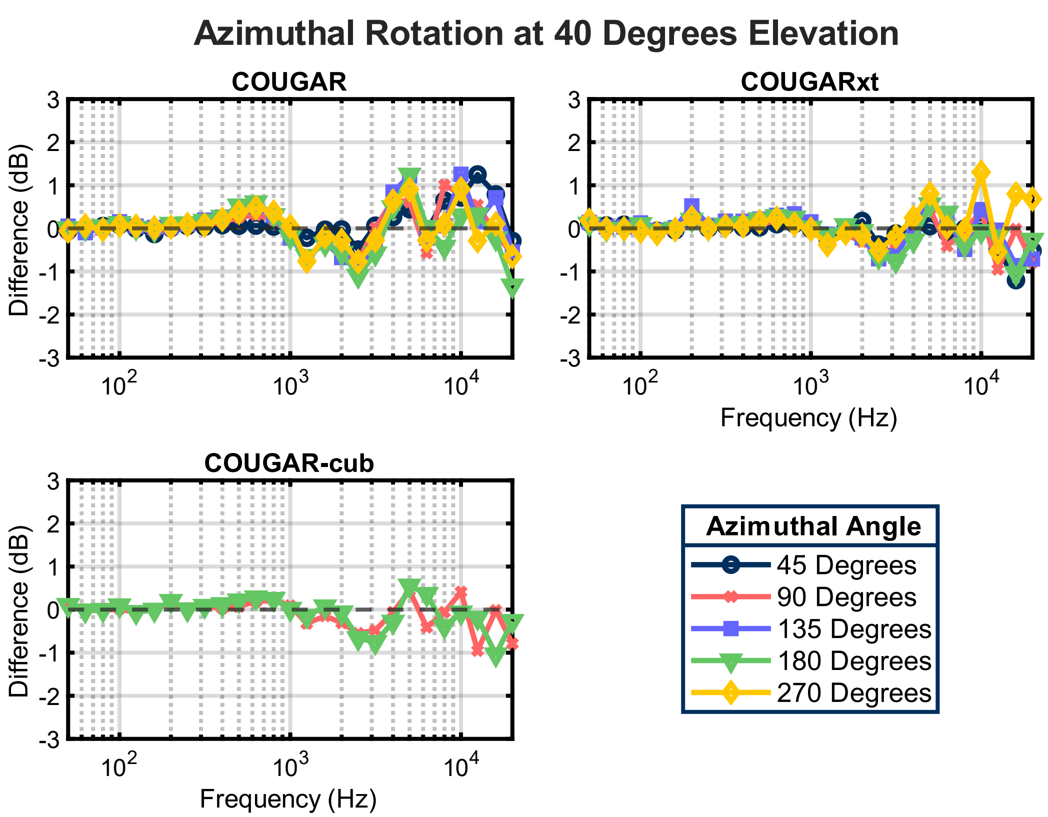

Figure D.17. Same as Figure 5.10, but for 40° elevation.

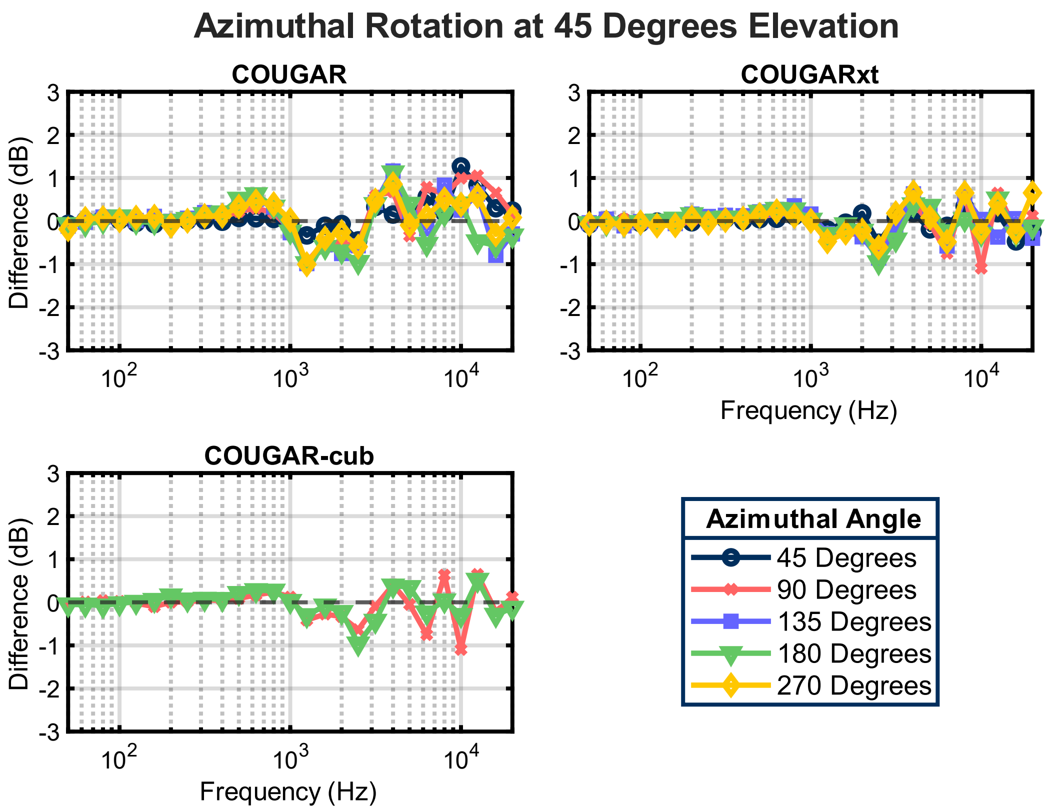

Figure D.18. Same as Figure 5.10, but for 45° elevation.

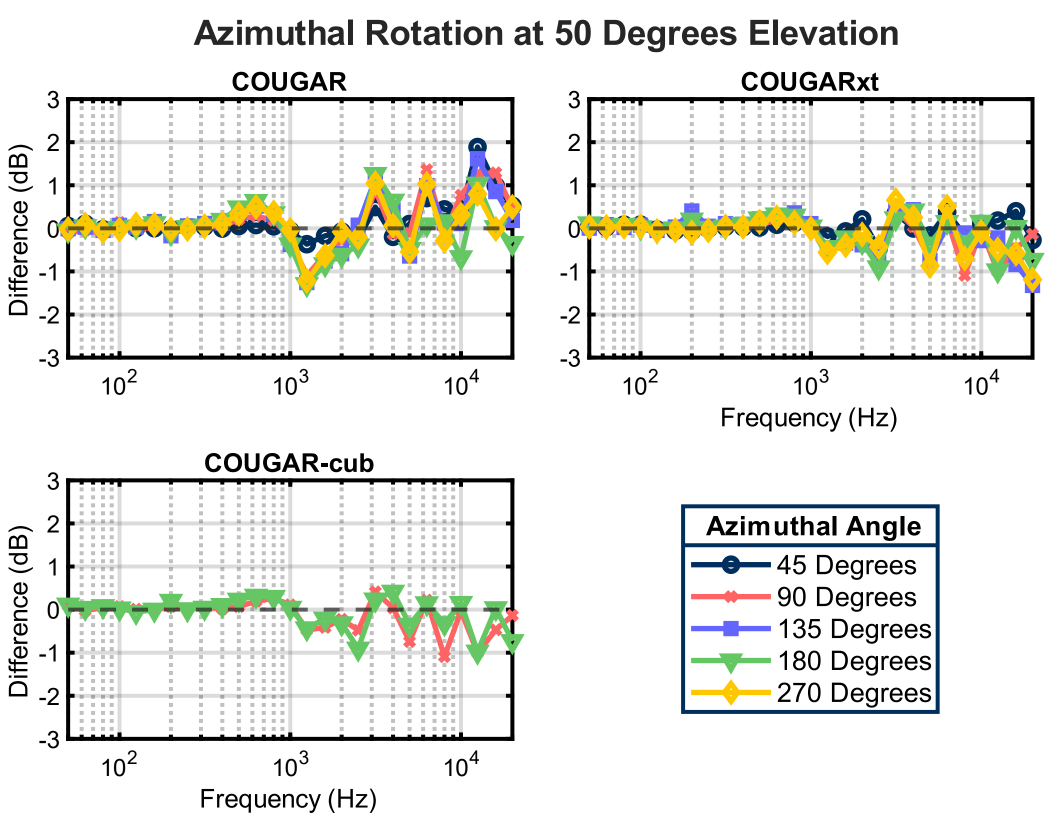

Figure D.19. Same as Figure 5.10, but for 50° elevation.

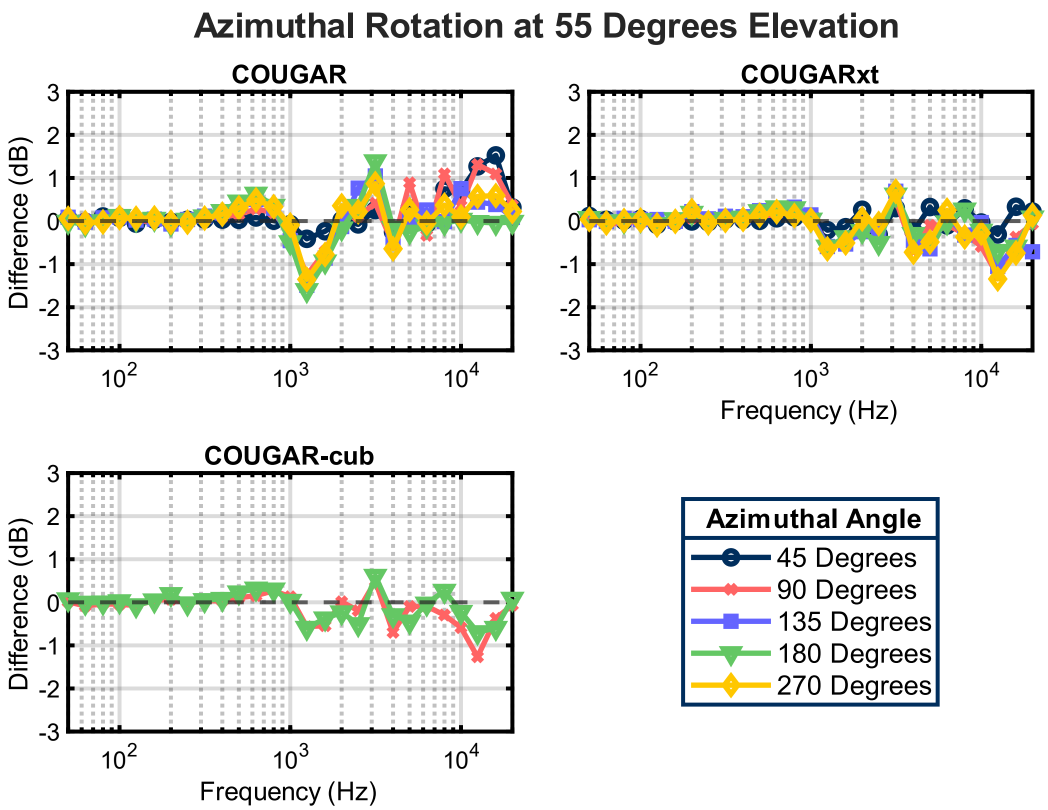

Figure D.20. Same as Figure 5.10, but for 55° elevation.

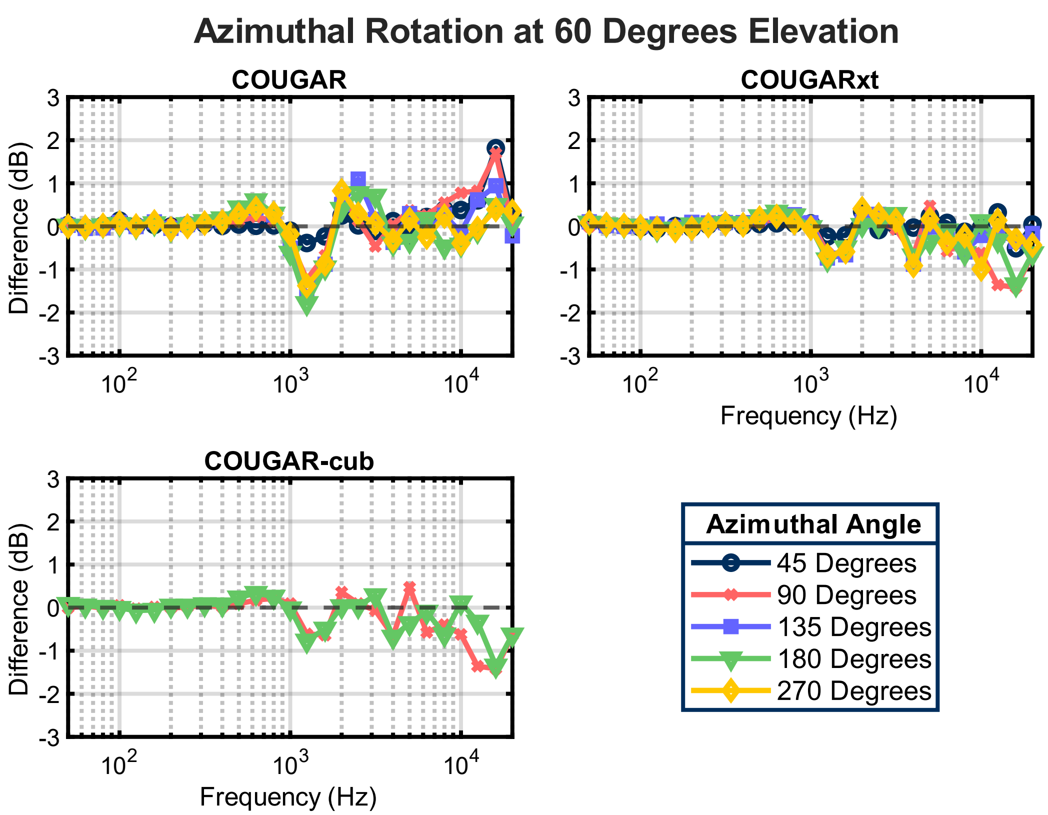

Figure D.21. Same as Figure 5.10, but for 60° elevation.

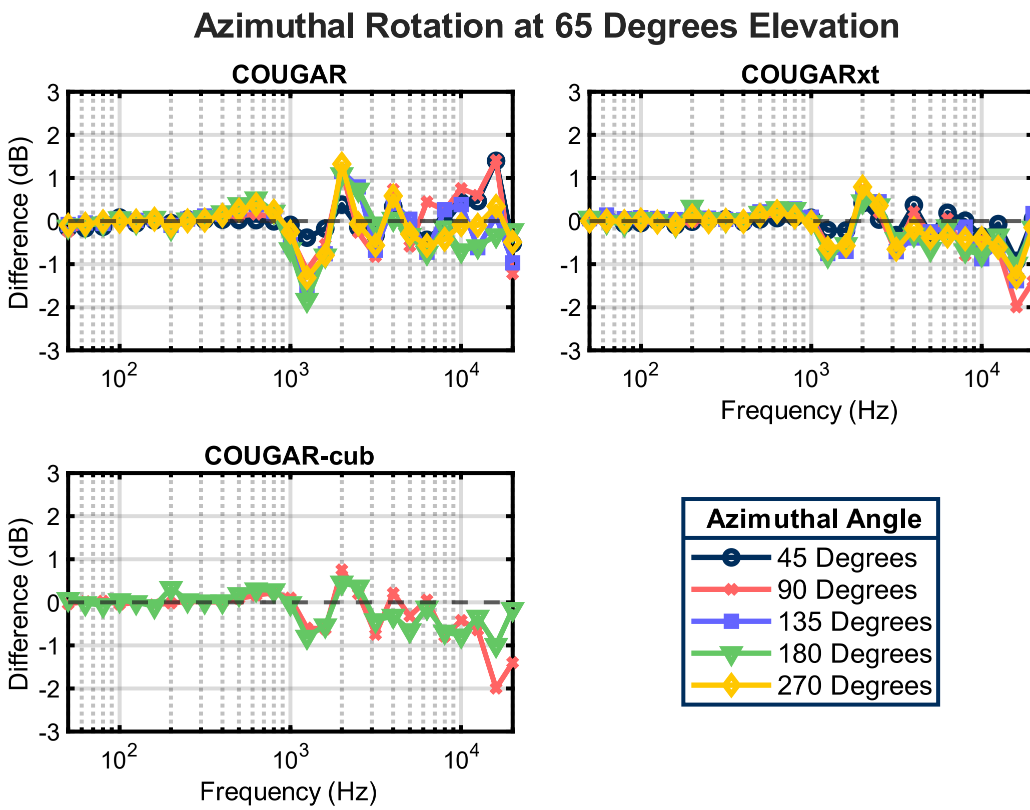

Figure D.22. Same as Figure 5.10, but for 65° elevation.

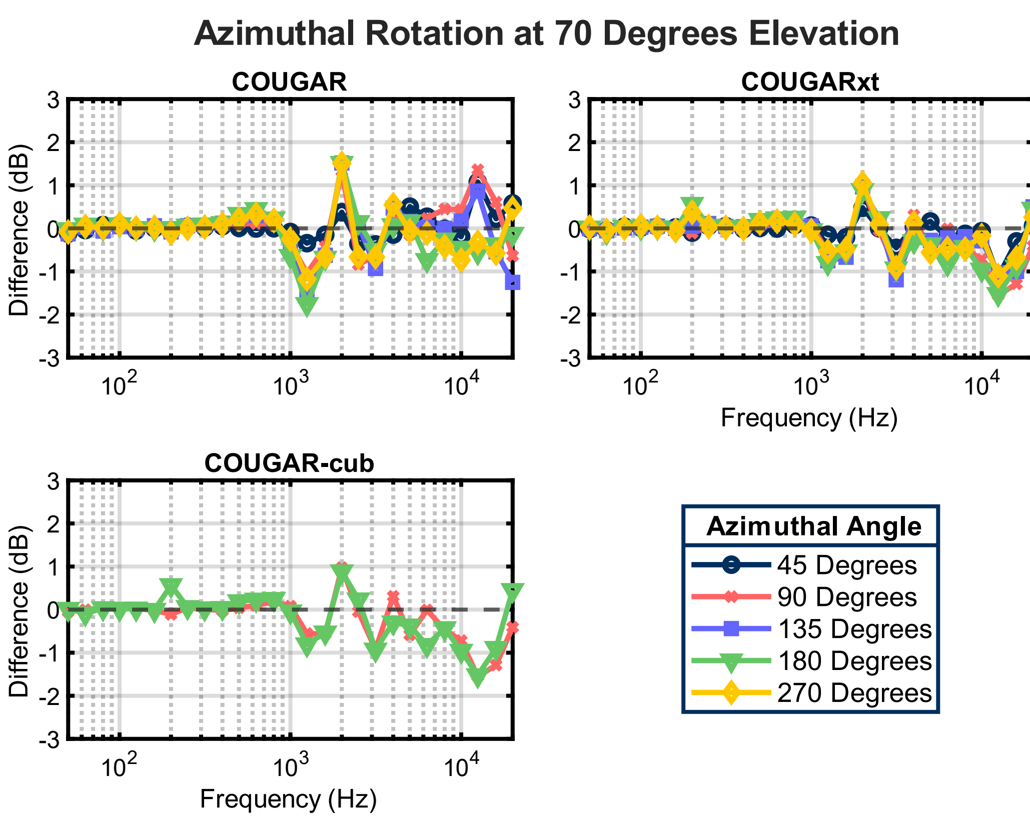

Figure D.23. Same as Figure 5.10, but for 70° elevation.

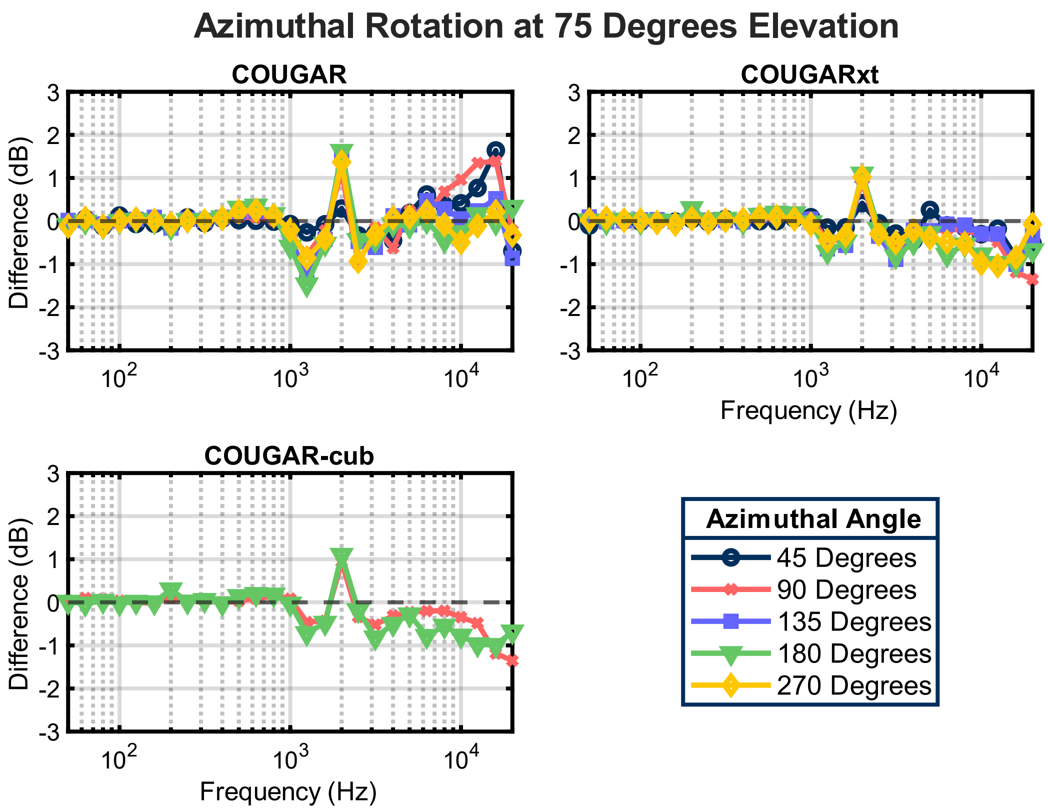

Figure D.24. Same as Figure 5.10, but for 75° elevation.

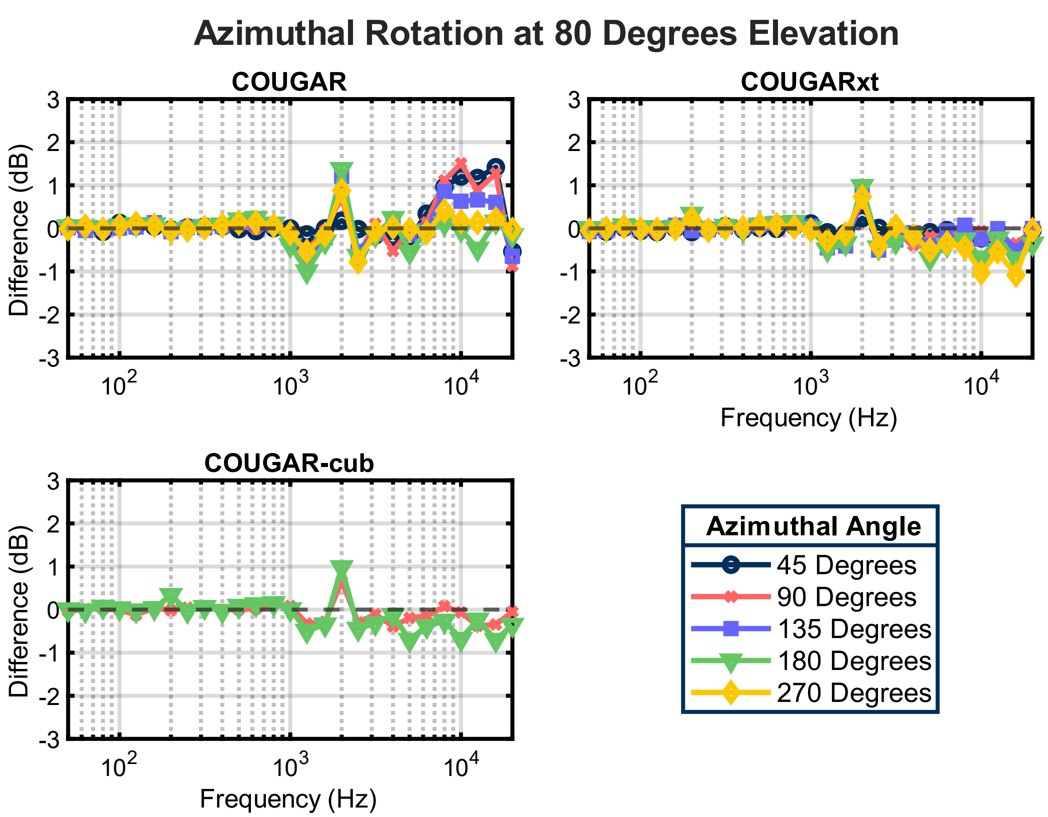

Figure D.25. Same as Figure 5.10, but for 80° elevation.

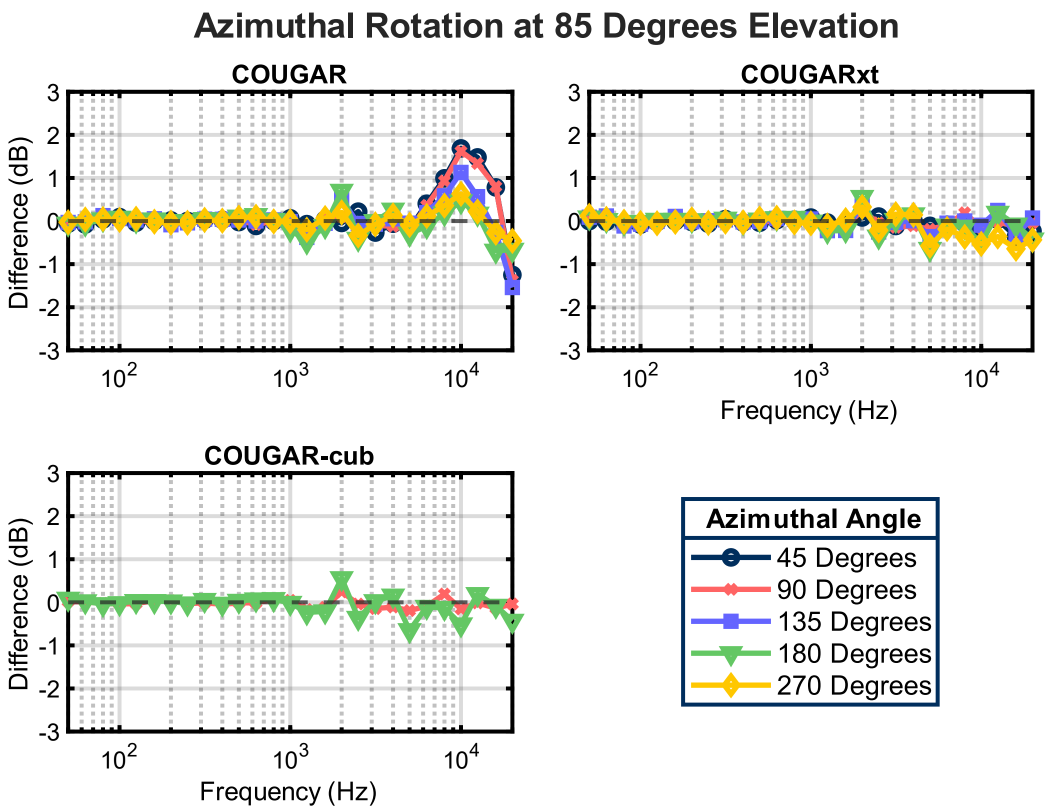

Figure D.26. Same as Figure 5.10, but for 85° elevation.

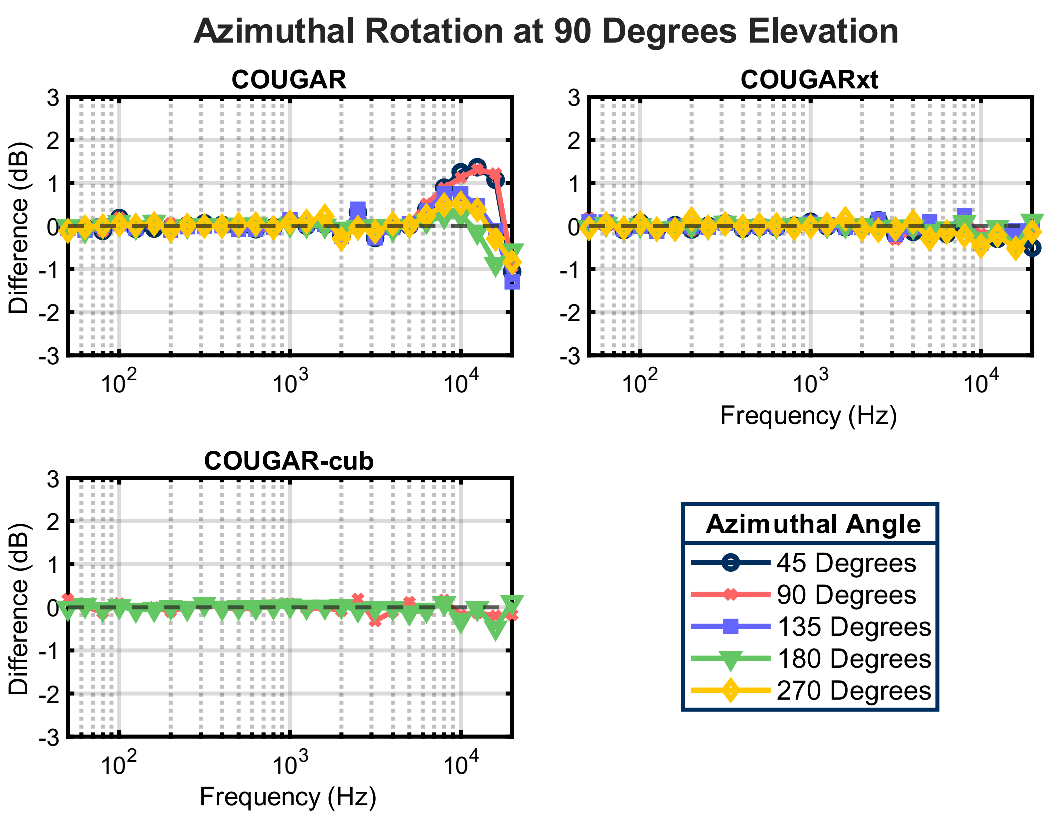

Figure D.27. Same as Figure 5.10, but for 90° elevation.

D.5. Additional Experiments

There were several additional experiments conducted during this measurement campaign. These extra tests explore further design options and validate current measurement and analysis techniques. The first experiment is to test the effects of the bird spikes on a COUGAR configuration. Two back-to-back arc sweeps were performed using the COUGAR both with and without the bird spikes and the difference between the two results are shown in Figure D.28. Evidently, the impact due to the bird spikes is negligible at all investigated frequencies.

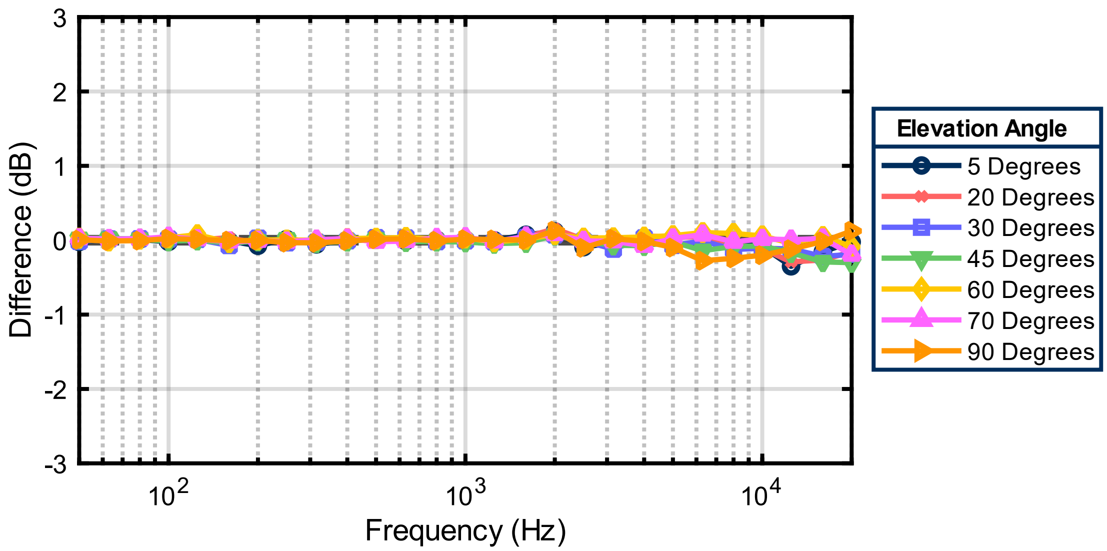

Figure D.28. A COUGAR configuration with bird spikes, shown relative to a COUGAR configuration without bird spikes. Evidently, the acoustic effects of the bird spikes are negligible at all frequencies shown.

The next investigation is to use a shorter version of the COUGAR-cub. All other results in this report use a COUGAR-cub windscreen with a height of eight inches. To investigate the effects of shortening the windscreen height, an arc sweep was made using a COUGAR-cub with a six-inch-tall windscreen and the results are shown below in Figure D.29. This figure is a replica Figure 3.14 with the additional results added to it. The shorter COUGAR-cub windscreen performs nearly identically to the original COUGAR-cub windscreen, except at 90 degrees around 10 kHz. These results indicate that windscreen height is not a primary driver of the acoustic response. Practical considerations such as the ability to fit a microphone into a shorter windscreen must still be considered when designing a final design. Most notably, neither a PCB 378A07 nor a GRAS 47AC could fit inside the shorter COUGAR-cub windscreen.

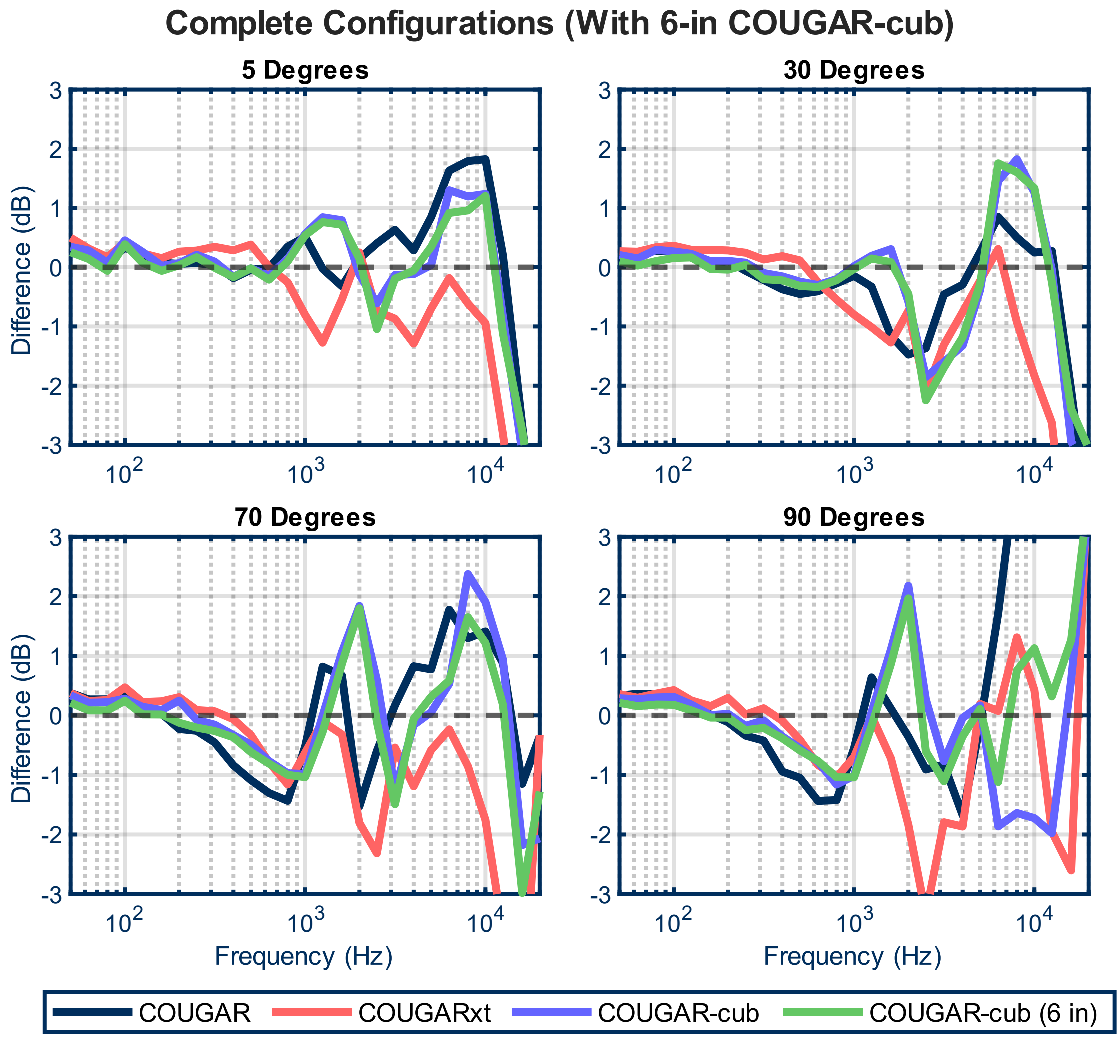

Figure D.29. Comparing all configurations, including the shorter COUGAR-cub, all shown relative to the baseline. This figure is a replica of Figure 3.14 with the addition of the shorter COUGAR-cub curves. The shorter windscreen performs nearly identical to the original COUGAR-cub windscreen.

The next several investigations concern the measurement repeatability. To test the repeatability in a limiting case, the baseline measurement was repeated at the conclusion of the testing campaign, three days after the original baseline measurement. The results are shown in Figure D.30. According to these results, the measurements are almost perfectly repeatable below 1 kHz and are within ±1 dB up to 20 kHz.

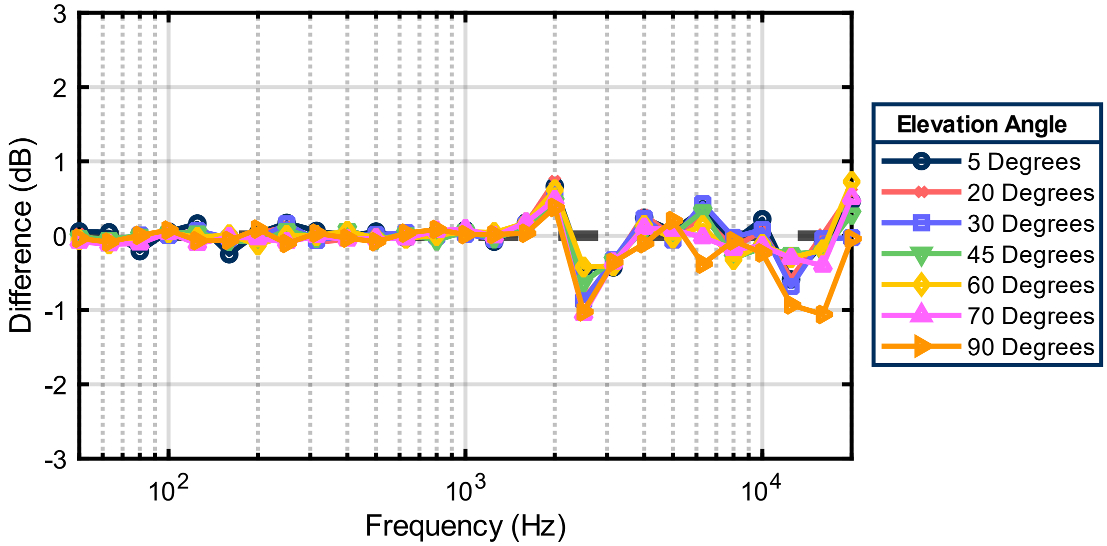

Figure D.30. The verification baseline measurement, shown relative to the original baseline measurement. The two measurements were taken three days apart and demonstrate the overall repeatability of the baseline measurement.

All laboratory results shown in this report used the reference microphone laid to the side of the device under test to correct for inconsistent speaker output. Here, the usefulness of this technique is explored. Figure D.31 shows the identical results to Figure D.30, but this time the reference microphone was ignored in the processing. Notice the inconsistent values below 1 kHz in Figure D.31that did not occur in Figure D.30. This validates the process of using the reference microphone to correct for the inconsistent speaker output, especially at lower frequencies. Some small differences above 1 kHz between the two figures may be investigated in the future.

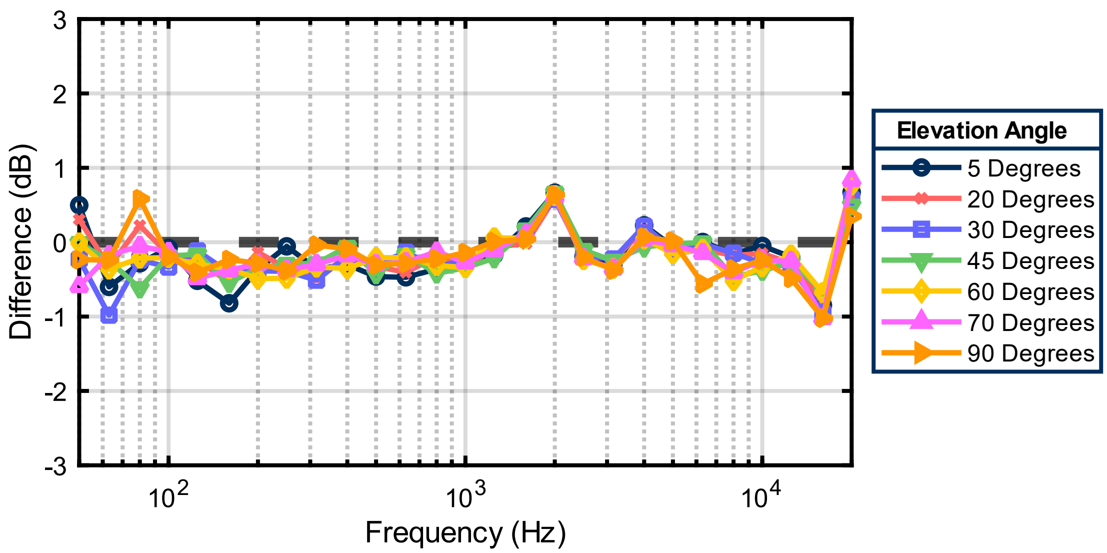

Figure D.31. The verification baseline measurement, shown relative to the original baseline measurement. For these results, the reference microphone was not used to correct for inconsistent speaker output. The effects are primarily noticeable at lower frequencies.

Repeatability tests are important to perform for the final microphone configurations as well. Figure D.32 compares two arc sweeps with COUGAR performed two days apart and after the

COUGAR configuration had been removed and other tests had occurred, required the COUGAR to be set up again for the second measurement. The results are nearly identical below 1 kHz, which is where the dominant loudness contribution occurs for sonic booms. Additionally, Figure D.33 shows a similar experiment using a COUGAR-cub, performed one day apart and after removing and setting up the COUGAR-cub again for the second test. The results are similar, indicating that both measurements were especially repeatable below 1 kHz.

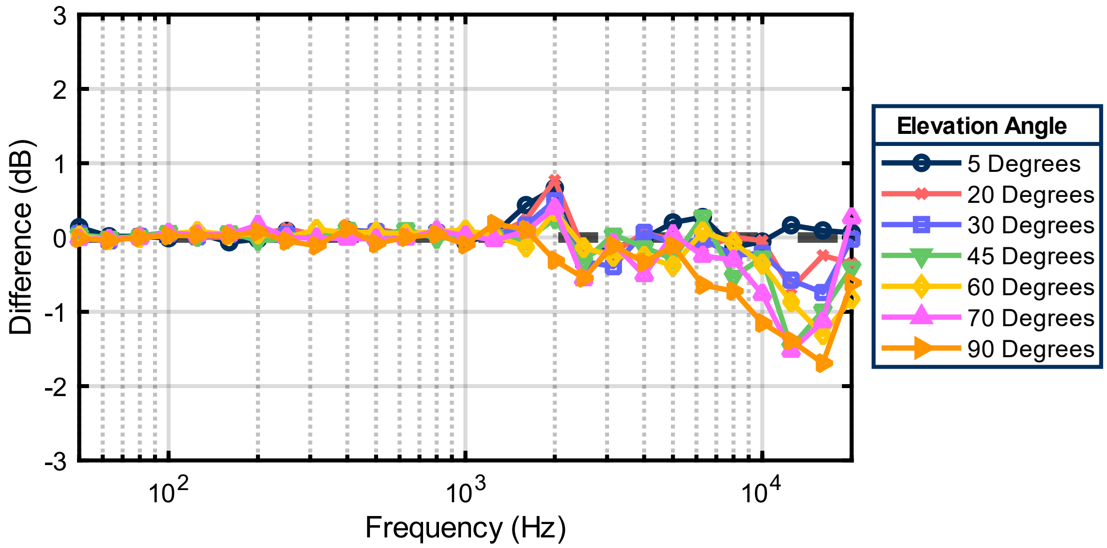

Figure D.32. Validation testing of a COUGAR configuration. The two measurements occurred two days apart. The results indicate a high amount of repeatability below 1 kHz.

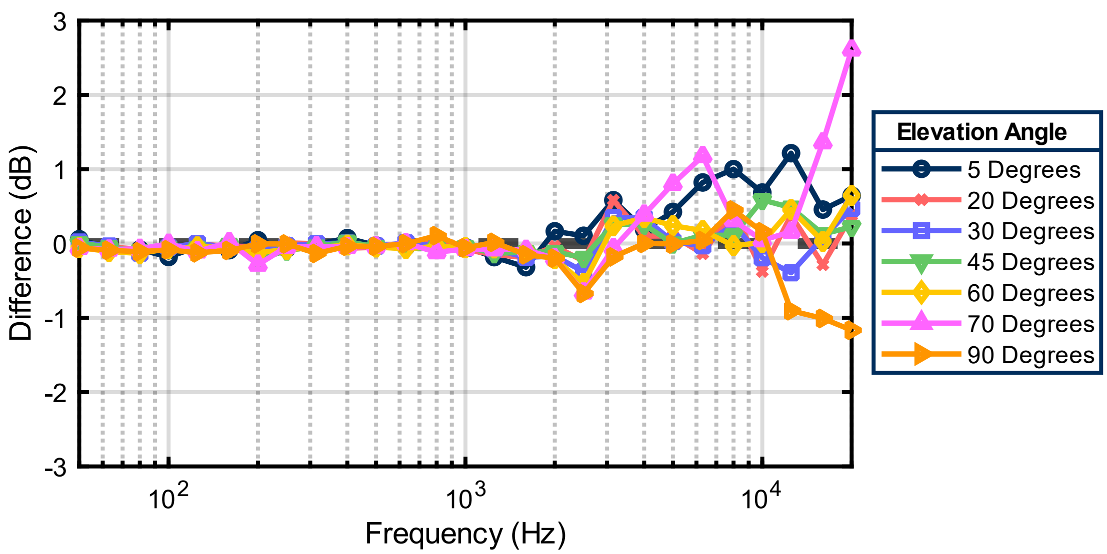

Figure D.33. Validation testing of a COUGAR-cub configuration. The two measurements occurred one day apart. The results indicate a high amount of repeatability below 1 kHz.

References

Anderson, M. C. (2021). “Weather-Robust Systems for Outdoor Acoustical Measurements,” Senior thesis, Department of Physics and Astronomy, Brigham Young University.

Anderson, M. C., Gee, K. L., Durrant, J. T., Loubeau, A., and Doebler, W. J. (2021). “Investigating the impact of contaminating noise on candidate sonic boom metrics,” J. Acoust. Soc. Am. 150, A259-A259. https://doi.org/10.1121/10.0008214

Anderson, M. C., Gee, K. L., Novakovich, D. J., Mathews, L. T., and Jones, Z. T. (2022a). “Comparing two weather-robust microphone configurations for outdoor measurements,” Proc. Mtgs. Acoust. 42, 040005. https://doi.org/10.1121/2.0001561

Anderson, M. C., Gee, K. L., Novakovich, D. J., Rasband, R. D., Mathews, L. T., Durrant, J. T., Leete, K. M., and Loubeau, A. (2022b). “High-fidelity sonic boom measurements using weather-robust measurement equipment,” Proc. Mtgs. Acoust. 39, 040005. https://doi.org/10.1121/2.0001578

Anderson, M. C., Gee. K. L., Durrant, J. T., Loubeau, A., Doebler, W. J., Klos, J., “Recommendations for sonic boom community noise testing measurement and analysis.” Proc. Mtgs. Acoust. 50, 040008 (2024a) https://doi.org/10.1121/2.0001902

Anderson, M. C., Gee. K. L., Durrant, J. T., Loubeau, A., Doebler, W. J., Klos, J., “Reducing contaminating noise effects when calculating low-boom loudness levels.” J. Acoust. Soc. Am. 155, 3889-3899 (2024b) https://doi.org/10.1121/10.0026436

Bradley, K. A., Hobbs, C. M., Wilmer, C. B., Sparrow, V. W., Stout, T. A., Morgenstern, J. M., Underwood, K. H., Maglieri, D. J., Cowart, R. A., Collmar, M. T., Shen, H., and Blanc-Benon, P. (2020). "Sonic Booms in Atmospheric Turbulence (SonicBAT): The Influence of Turbulence on Shaped Sonic Booms," NASA/CR–2020–220509

Chetverikov, D., Liao, Z., Chernozhukov, V. (2020). "On cross-validated Lasso in high dimensions," arXiv:1605.02214 [math.ST]. https://doi.org/10.48550/arXiv.1605.02214

Cook, M. R., Gee, K. L., Transtrum, M. K., Lympany, S. V., and Calton, M. (2021a). “Application of a spectral-based wind noise reduction method to acoustical measurements,” J. Acoust. Soc. Am. 150, A104–A105. https://doi.org/10.1121/10.0007774

Cook, M. R., Gee, K. L., Transtrum, M. K., Lympany, S. V., and Calton, M. (2021b). “Automatic classification and reduction of wind noise in spectral data,” JASA Express Lett. 1, 063602. https://doi.org/10.1121/10.0005308

Cunningham, C., Anderson, M. C., Moats, L. T., Gee, K. L., Hart, G. W., and Hall, L. K. (2023). “Acoustical measurement and analysis of an Atlas V launch,” In Press 2023.

Doebler, W. J. (2017). “The minimum number of ground measurements required for narrow sonic boom metric 90% confidence intervals,” M.S. thesis, Graduate Program in Acoustics, Pennsylvania State University.

Doebler, W. J. and Rathsam, J. (2019). “How loud is X-59’s shaped sonic boom?” Proc. Mtgs. Acoust. 36, 040005. https://doi.org/10.1121/2.0001265

Downs, R., Page, J., Durrant, J. T., Gee, K. L., Novakovich, D. J., Anderson, M. C., and Loubeau, A., (2022). "Sonic boom measurements: Practical implications considering ground effects, microphone installation, and weather hardening," JASA Express Lett. 2, 104001. https://doi.org/10.1121/10.0014414

Durrant, J. T., Anderson, M. C., Bassett, M. S., Batelaan, R., Lawrence, D. C., Hall, L. K., and Gee, K. L. (2023). “Overview of BYU's acoustical measurements of the Falcon-9 SARah-1 launch, reentry sonic boom, and landing,” J. Acoust. Soc. Am. 153, A72. https://doi.org/10.1121/10.0018201

Durrant, J. T., Gee, K. L., Anderson, M. C., Cook, M. R., and Loubeau, A. (2021a) "Preliminary lasso regression analysis of environmental effects on sonic boom metric variability," J. Acoust. Soc. Am. 150, A259. https://doi.org/10.1121/10.0008215

Durrant, J. T., Gee, K. L., Anderson, M. C., Mathews, L. T., Rasband, R. D., Novakovich, D. J., Loubeau, A., and Doebler, W. J. (2021b). “An overview of Brigham Young University’s participation in NASA’s CarpetDIEM campaign,” Proc. Mtgs. Acoust. 43, 045002. https://doi.org/10.1121/2.0001589

Gee, K. L., Hart, G. W., Cunningham, C. F., Anderson, M. C., Bassett, M. S., Mathews, L. T., Durrant, J. T., Moats, L. T., Coyle, W. L., Kellison, M. S., and Kuffskie, M. J. (2023). “Space Launch System acoustics: Far-field noise measurements of the Artemis-I launch,” JASA Express Lett. 3, 023601. https://doi.org/10.1121/10.0016878

Gee, K. L., Neilsen, T. B., and James, M. M. (2013). “On the crest factor of noise in full-scale supersonic jet engine measurements,” Proc. Mtgs. Acoust. 20, 045003. https://doi.org/10.1121/1.4869290

Gee, K. L., Novakovich, D. J., Mathews, L. T., Anderson, M. C., and Rasband, R. D. (2020). “Development of a weather-robust ground-based system for sonic boom measurements,” NASA/CR-2020-5001870

Hart, G. W., Mathews, L. T., Anderson, M. C., Durrant, J. T., Massett, M. S., Olausson, S. A., Houston, G., and Gee, K. L. (2021). “Methods and results of acoustical measurements made of a Delta IV Heavy launch,” Proc. Mtgs. Acoust. 45, 040003. https://doi.org/10.1121/2.0001580

Hubbard, H. H., Maglieri, D. J., Huckel, V., and Hilton, D. A. (1964). “Ground measurements of sonic-boom pressures for the altitude range of 10,000 to 75,000 feet,” NASA-TR-R-198

James, M., Salton, A., Calton, M., Downing, M., Gee, K., and Mclnerny, S. A. (2020). “Commercial Space Operations Noise and Sonic Boom Measurements,” Nat. Acad. Sci. National Academies Press. https://doi.org/10.17226/25834

Jones, Z., Cook, M. R., Gee, K. L., Transtrum, M., K., Lympany, S. V., Calton, M. F., and James, M. M. (2020). “Examining wind noise reduction effects of windscreens and microphone elevation in outdoor acoustical measurements,” Proc. Mtgs. Acoust. 42, 045007. https://doi.org/10.1121/2.0001413

Klos, J. (2020). “Recommendations for Using Noise Monitors to Estimate Noise Exposure During X-59 Community Tests,” NASA/TM–20205007926

Klos, J. (2022). “An Adaptation of ISO 11204 using Customized Correction Grades to Mitigate Contaminating noise Effects when Computing Sonic Boom Loudness Levels,” NASA/TM-20220010779

Lee, J., Rathsam, J., and Wilson, A., (2020). “Bayesian statistical models for community annoyance survey data,” J. Acoust. Soc. Am. 147, 2222. https://doi.org/10.1121/10.0001021

Lonzaga, J. B., Doebler, W., Loubeau, A., Aumann, A., Page, J., and Shumway, M. (2020). "Latest Release of Fast PCBoom Code for Sonic Boom Propagation," https://ntrs.nasa.gov/citations/20205009119

Lonzaga, J. B., Page, J. A., Downs, R. S., Kaye, S. R, Shumway, M. J., Loubeau, A., Doebler, W. J. (2022). “PCBoom Version 7 Technical Reference,” https://ntrs.nasa.gov/citations/20220007177

Loubeau, A. and Page, J. (2018). “Human perception of sonic booms from supersonic aircraft,” Acoust. Today 14(3): 23-30.

Loubeau, A., Naka, Y., Cook, B. G., Sparrow, V. W., and Morgenstern, J. M. (2015). “A new evaluation of noise metrics for sonic booms using existing data,” AIP Conf. Proc. 1685, 090015. https://doi.org/10.1063/1.4934481

Maglieri, D. J., Bobbitt, P. J., Plotkin, K. J., Shepherd, K. P., Coen, P. G, and Richwine, D. M. (2014). “Sonic Boom: Six Decades of Research,” NASA/SP-2014-622

MathWorks® (2023) lasso, https://www.mathworks.com/help/stats/lasso.html, accessed May 31, 2023.

Obuchi, T. and Kabashima, Y. (2016). "Cross validation in LASSO and its acceleration," J. Stat. Mech. 053304. https://doi.org/10.1088/1742-5468/2016/05/053304

Page, J. A., Hodgdon, K. K., Hunte, R. P., Davis, D. E., Gaugler, T. A., Downs, R., Cowart, R. A., Maglieri, D. J., Hobbs, C., Baker, G., Collmar, M., Bradley, K. A., Sonak, B., Crom, D., Cutler, C., (2020). “Quiet Supersonic Flights 2018 (QSF18) Test: Galveston, Texas Risk Reduction for Future Community Testing with a Low Boom Flight Demonstration Vehicle,” NASA/CR–2020-220589

Page, J. A., Hodgdon, K. K., Krecker, P., Cowart, R., Hobbs, C., Wilmer, C., Koening, C., Holmes, T., Gaugler, T., Shumway, D. L., Rosenberger, J. L., Philips, D., (2014). “Waveforms and Sonic Boom Perception and Response (WSPR): Low-Boom Community Response Program Pilot Test Design, Execution, and Analysis,” NASA/CR 2014-218180

Page, J. A., Lonzaga, J. B., Shumway, M. J., Son, S. R., Downs, R. S., Loubeau, A., Doebler, W. J. (2023). “PCBoom Version 7.3 User’s Guide,” https://ntrs.nasa.gov/citations/20220016207

Page, J. A., Plotkin, K., Hobbs, C., Sparrow, V., Salamone, J., Cowart, R., Elmer, K., Welge, H. R., Ladd, J., Maglieri, D., Piacsek, A., (2015). “Superboom Caustic Analysis and Measurement Program (SCAMP) Final Report,” NASA/CR-2015-218871

Rallabhandi, S. K., Loubeau, A., “Summary of Propagation Cases of the Third AIAA Sonic Boom Prediction Workshop.” Journal of aircraft 59(3), 578-694 (2022) https://doi.org/10.2514/1.C036327

Saha, S. Moorthi, S., Wu X., Wang J., Nadiga S., Tripp, P., Behringer D., Hou, Y.-T., Chuang, H., Iredell, M., Ek, M., Meng, J., Yang, R., Mendez, M. P., van den Dool, H., Zhang, Q., Wang, W., Chen, M., and Becker, E. (2014). “The NCEP Climate Forecast System Version 2” J. Clim., 27, 2185–2208. http://dx.doi.org/10.1175/JCLI-D-12-00823.1

Shepherd, K. P. and Sullivan, B. M., (1991). “A Loudness Calculation Procedure Applied to Shaped Sonic Booms,” NASA Technical Paper 3134

Stout, T. A. (2018). “Simulation of N-wave and Shaped Supersonic Signature Turbulent Variations,” PhD thesis, Graduate Program in Acoustics, Pennsylvania State University.

Tibshirani R. (1996). "Regression Shrinkage and Selection via the Lasso," J. R. Statist. Soc. B 58, No. 1, pp. 267-288.

van den Berg, G. P. (2006), “Wind-induced noise in a screened microphone,” J. Acoust. Soc. Am. 119, 824–833. https://doi.org/10.1121/1.2146085